The Dissertation Committee for Erin Wells Bonning
certifies that this is the approved version of the following dissertation:

Computational and Astrophysical Studies of Black Hole Spacetimes

Committee:

Richard Matzner, Supervisor

Cécile Dewitt-Morette

Philip Morrison

Paul Shapiro

Lawrence Shepley

Computational and Astrophysical Studies of Black Hole Spacetimes

by

Erin Wells Bonning, B.A.

DISSERTATION

Presented to the Faculty of the Graduate School of

The University of Texas at Austin

in Partial Fulfillment

of the Requirements

for the Degree of

DOCTOR OF PHILOSOPHY

THE UNIVERSITY OF TEXAS AT AUSTIN

August 2004

In loving memory of my grandmother,

Julie Ann Longhenry

Acknowledgments

I acknowledge first my graduate adviser Richard Matzner for his welcome to the Center for Relativity, for suggestions and guidance in choosing a thesis topic, and for the many helpful conversations and discussions we have had in the course of my graduate studies. I am especially grateful for his unwavering support of my scientific interests beyond the immediate realm of my thesis work. I have from time to time worked on various projects outside the Center for Relativity, during which he has graciously offered support and encouragement, no less than when I have been working directly with him.

I have profited greatly through several collaborations and short working projects with scientists at other institutions. In particular I am grateful for the hospitality of Gerd Bacher at Julius-Maximilians-Universität in Würzburg, Germany, Eric Gourgoulhon at the Observatoire de Paris à Meudon and Maurizio Falanga at the Service d'Astrophysique/CEA in Saclay, France. Special acknowledgment is also due to Greg Shields of the UT Astronomy Department for giving me the opportunity to work with real data during the last year.

While pursuing my undergraduate degree in liberal arts, I benefited immeasurably from the patient tutoring, education, and mentoring in physics by Anne-Marie Novo-Gradac at the U.S. Naval Academy and Jim Beall, my undergraduate adviser at St. John's College. I owe a special debt of gratitude

to these two people who introduced me to their respective fields of study, and who unhesitatingly took the time to answer any physics questions I could think to ask them. Without the opportunity to work so closely with them, I should never have been prepared to enter graduate school.

Of course, I am everlastingly grateful for the unconditional love and support of my father and mother, my immediate and extended family, and my friends, among whom I am particularly thankful to B. Good for moral support and inspiration over many years.

Finally, this work would not have been possible without the financial support of the NASA Graduate Student Researcher's Program fellowship, under which I was funded from 2002-2004.

ERIN WELLS BONNING
University of Texas at Austin
August 2004

Computational and Astrophysical Studies of Black Hole Spacetimes

Publication No. _____

Erin Wells Bonning, Ph.D.
The University of Texas at Austin, 2004

Supervisor: Richard Matzner

This dissertation addresses three problems of interest concerning astrophysical black holes, namely the numerical solution of Einstein's equations for a spacetime containing two orbiting and coalescing black holes, the simulation of a light curve from an accretion disk near the innermost orbit around a spinning black hole, and determining relations between central black hole mass and host galaxy properties in active galactic nuclei.

I first address the problem of setting the initial conditions for the Cauchy formulation of general relativity. I present the solution of the constraint equations via a conformal decomposition and discuss the construction of the background fields as superposed Kerr-Schild black holes. The constraint equations are solved for two black holes with arbitrary linear and angular momenta. The binding energy and spin-spin coupling of the two holes are computed in the initial data slice and analyzed. I discuss the extent to which the

superposed Kerr-Schild initial data limits extraneous radiation and estimate the accuracy of determinations of the innermost stable circular orbit through sequences of initial data.

The second topic concerns the time variability of isotropically radiating material orbiting in an idealized accretion disk around a spinning black hole. I solve the geodesic equations for photon propagation from the surface of the disk to an observer for different orbital parameters. The general relativistic effects upon the signal received are calculated, including the energy shift, relativistic time delay, and gravitational lensing. I produce light curves showing the change in flux over time due to the relativistic effects. Applications of this model to stellar-mass systems as well as super-massive black holes are discussed.

Lastly, I discuss the relationship between a galaxy's central black hole and its evolutionary history. In particular I examine the correlations among host galaxy luminosity, stellar velocity dispersion, and central black hole mass in active galactic nuclei. I derive black hole masses and stellar velocity dispersions from quasar broad and narrow emission lines, respectively. The utility of using the narrow line emitting gas as a surrogate for stellar velocity dispersion is investigated through examining host magnitudes and narrow [O III] line widths for low redshift quasars.

Table of Contents

List of Tables

List of Figures

Chapter 1

Introduction

1.1 General Background and Motivation

The general theory of relativity passed a number of observational tests early in its existence, such as the predictions concerning the precession of Mercury's orbit, the deflection of starlight around the Sun, and the loss of energy through gravitational radiation seen indirectly in the binary pulsar PSR 1913+16. But in large part the theory has remained off-limits to direct experimental or observational confirmation due to the intrinsic weakness of the gravitational field, and the inherent difficulty of measuring small fluctuations in it which is necessary for understanding the dynamics of the geometry of spacetime.

The most interesting astrophysical sources – such as massive compact binaries, supernovae, and the sources of gamma ray bursts – are events that take place in environments in which relativistic effects play important roles. An accurate probing of the gravitational dynamics of these systems would doubtless confirm some aspects of relativity theory while posing yet more interesting questions. In the coming years, we will begin to have observational data of these events from the ground-based gravitational interferometers such

as LIGO, VIRGO, GEO and TAMA. Additionally, next generation detectors are already in the development stage, including the space-based Laser Interferometer Space Antenna (LISA), and LIGO 2 which should far surpass the current interferometers in terms of sensitivity and frequencies covered.

The coalescence of binaries containing black holes is a prime candidate for observation by LISA (the merger of $10^5 M_\odot$ black holes) and the ground based detectors (the merger of $10 M_\odot$ black holes). As two black holes in a binary system orbit each other they emit gravitational radiation, and thereby lose energy and slowly spiral in towards each other. Because of the circularizing effects of gravitational radiation damping, the orbits of the holes are expected to become quasi-circular as they approach each other. The inspiraling orbits will continue until some point where relativistic (and possibly tidal) effects cause the orbits to become unstable, at which time the holes plunge rapidly together and merge. This innermost stable circular orbit (ISCO) produces a distinct feature in the gravitational waveform, namely a high frequency cutoff. The dynamics of the holes during these final orbits, especially the orbital angular velocity and separation determine the dominant characteristics of the detectable waves. Any knowledge of these parameters is advantageous for detecting radiation from these binary systems.

In addition to gravitational radiation, black holes are associated with emission of electromagnetic radiation from orbiting and infalling matter. In particular many X-ray binaries are known to contain black holes accreting material from a companion star. Black holes are also thought to be involved

in the energy production powering gamma-ray bursts and the relativistic jets observed in radio frequencies. I present here a tool to analyze observable and diagnostic features of X-rays from accretion disks around black holes. This method uses ray tracing to directly image the source and to predict the spectrum of radiation observed. Observations of galactic X-ray sources (especially of binaries containing a black hole of ~ 10 solar masses) may permit these methods to probe the structure of the accretion disk. In particular, the angular momentum of the black hole may be inferred from the period of the innermost orbit. This is a key goal of black hole astrophysics; this quantity remains an unknown and un-measured parameter in observed black hole systems.

Among the contexts in which gravitational radiation is a result of black hole dynamics, one of the most promising for the future space-based gravitational interferometer is that resulting from the central supermassive black holes of galaxies merging together. It is known that all bulges of galaxies contain a supermassive black hole. It is further known that all galaxies have likely undergone at least one major merger event in their history. (A major merger is one that is defined by a $1:1$ to $1:4$ mass ratio between galaxies.) Therefore, we expect binary black holes to arise with some frequency in the universe. However, the dynamics in the centers of the merging galaxies are poorly understood. In particular it is unknown on what time scale the black hole mergers occur. It is possible that the black hole orbits 'harden', which is to say that the orbits sink to some radius through dynamical friction

and then remain orbiting each other in an empty environment. These black holes will not have merged through emission of gravitational radiation in the present lifetime of the universe. Alternatively, stellar and gas dynamics in the centers of galaxies may be such that the black holes coalesce very quickly. While the physics of mergers is not well understood, some simple models can constrain the population of binary black holes in galaxies in terms of available observations.

I have carried out a study of host galaxies in active galactic nuclei (AGN) and their associated stellar velocity dispersions as indicated by narrow line emitting gas orbiting in the galactic potential. This study is important in the study of AGN, per se, in terms of evaluating the utility of using gas velocities as a surrogate for stellar velocities, and in terms of quantifying observable differences between radio-loud and radio-quiet objects. The observations may, additionally, illuminate calculations of central black hole mass and stellar velocities in galactic bulges. A more accurate knowledge of these parameters for galaxies and AGN and high redshift enable constraints to be placed on the demographics of supermassive black holes formation and mergers, there therefore on event rate predictions for the LISA (space-based) gravitational wave detector.

1.2 Plan of the Dissertation

This dissertation is divided into three parts. The first, and most substantial, addresses the solution of the initial value problem for binary black

holes. The setting of the background data and numerical solution of the constraint equations is discussed and results from that calculation are presented. Certain physical quantities, such as the binding energy and spin-spin coupling of two Kerr black holes are computed in the initial data slice and analyzed. I additionally discuss the extent to which the superposed Kerr-Schild initial data limits extraneous radiation in the data sets and estimate the accuracy of determinations of the innermost stable circular orbit for two black holes via sequences of initial data. Much of the material in Chapter 2 closely follows work I have previously published with R. Matzner, P. Marronetti, and D. Neilsen (see reference [9]).

Chapter 3 presents a calculation of the time variability of isotropically radiating matter in an idealized accretion disk around a spinning black hole developed in collaboration with M. Falanga. The geodesic equations for a photon propagating from the surface of a disk to an observer are solved. Various general relativistic effects upon the signal received at infinity are calculated including the energy shift, relativistic time delay and phase shift, and gravitational lensing. Light curves and emission profiles are presented from orbits at varying disk inclinations and radii, and for spinning and non-spinning black holes.

Chapter 4 discusses work relating to active galactic nuclei done in collaboration with G. Shields, S. Salviander, and R. McLure. The paper presented there investigates the relationship between host galaxy bulge luminosity, stellar velocity dispersion, and central black hole masses of AGN. We investigate

in detail the utility of using the velocity of narrow line emitting gas as a surrogate for stellar velocity dispersion in objects which are too far away, or contain a nucleus whose luminosity makes measurements of stellar velocities impractical. Additionally, we take note of an unexplained correlation between narrow line width and the radio luminosity of a QSO.

Chapter 2

The Initial Value Problem

2.1 Introduction

The proper way to predict gravitational waveforms for orbiting black holes is to set initial data for two widely separated holes, and then solve the evolution equations to follow the inspiral through merger and beyond. This problem is well beyond the capabilities of current evolution codes. One can, however, turn to the more tractable initial value problem in order to obtain some information about orbiting black holes. Given a collection of initial data for black holes in circular orbits with decreasing radius, one can try to identify a sequence of initial data that corresponds to instantaneous images of a time-dependent evolution. When a suitable sequence of initial data slices has been obtained, they can then be used to determine the various orbital parameters associated with the innermost stable circular orbit (ISCO). For example, the change in binding energy with respect to the orbital radius allows one to identify the separation at the innermost orbit, $\ell_{\rm ISCO}$ and a similar analysis of the angular momentum gives the frequency, $\omega_{\rm ISCO}$. The difficulty in this approach comes in ensuring that the initial data at one radius correspond to the same physical system as the data for another radius, and that the physical system represented is an astrophysically realistic one containing no extraneous

fields which could influence the calculation of the binding energy. Thus, while the initial data approach to studying binary black holes is a computationally feasible way to extract physics from initial data slices, it is not without problems. I discuss here the solution to the initial value problem for spacetimes containing two black holes, and elaborate on the limitations of this approach.

2.2 The 3+1 Formulation

General relativity in the Arnowitt-Deser-Misner (ADM) formalism [2] is formulated as a Cauchy problem where the spatial 3-metric g_{ij} and its conjugate momentum K_{ij} are specified on an initial space-like hypersurface and then propagated forward in time. In this 3+1 formulation, the spacetime $\mathcal{M}$ is foliated into hypersurfaces Σ_t of constant t where t is some scalar function serving as the time coordinate. A normal vector field n^a is defined on the hypersurfaces Σ such that the direction of increasing time is given as

$$t^a \equiv \alpha n^a + \beta^a, \tag{2.1}$$

where α is the lapse function and β^i is the shift 3-vector. The 3-metric g_{ij} induced on each spatial hypersurface Σ_t is the fundamental variable. The extrinsic curvature, K_{ij}, plays the role of momentum conjugate to the metric, and describes the embedding of a t = constant hypersurface into the 4-geometry. The extrinsic curvature K_{ij} is given by the Lie derivative along the normal

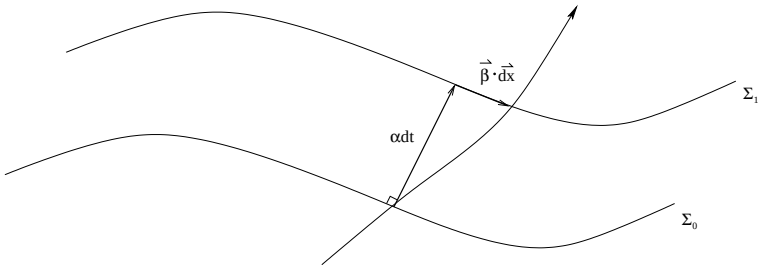

Figure 2.1: A foliation of spacetime in the 3+1 (ADM) formulation. Σ are $t = constant$ space-like hypersurfaces. The coordinates on Σ_t are related to each other by the gauge variables α and β.

vector field:

$$K_{ij} = -\frac{1}{2}\pounds_n g_{ij}. \tag{2.2}$$

The ADM metric is

$$\mathrm{d}s^2 = -(\alpha^2 - \beta_i\beta^i)\,\mathrm{d}t^2 + 2\beta_i\,\mathrm{d}t\,\mathrm{d}x^i + g_{ij}\,\mathrm{d}x^i\,\mathrm{d}x^j. \tag{2.3}$$

Latin indices run $1, 2, 3$ and are lowered and raised by g_{ij} and its 3-dimensional inverse g^{ij}. α and β^i are gauge functions that relate the coordinates on each hypersurface to each other.

The Einstein field equations in this formulation contain both hyperbolic evolution equations, and elliptic constraint equations. The time dependent equations in vacuum are:

$$\begin{aligned} \partial_t g_{ij} &= -2\alpha K_{ij} + \nabla_i\beta_j + \nabla_j\beta_i & (2.4)\\ \partial_t K_{ij} &= \beta^k\partial_k K_{ij} - \partial^k\beta_i K_{kj} - \nabla_i\nabla_j\alpha + \\ &\quad \alpha[R_{ij} + K_{ij}K - 2K_{im}K^m_j] & (2.5) \end{aligned}$$

And the time-independent constraint equations are:

$$R - K_{ij}K^{ij} + K^2 \;=\; 0, \tag{2.6}$$

$$\nabla_j \left(K^{ij} - g^{ij}K \right) \;=\; 0. \tag{2.7}$$

Here R is the 3-dimensional Ricci scalar, K is the trace of the extrinsic curvature tensor, and ∇_j is the 3-dimensional covariant derivative compatible with g_{ij}.

Similarly to the $\nabla \cdot \overrightarrow{E}$ and $\nabla \cdot \overrightarrow{B}$ conditions in electromagnetism, any initial data specified must satisfy these constraint equations; one may not freely specify all components of g_{ij} and K_{ij}. Eq. (2.6) is called the Hamiltonian constraint and Eqs. (2.7) are referred to as the momentum constraints.

2.3 The Conformal Decomposition

The initial value problem in general relativity requires one to consistently identify and separate the constrained and the freely-specifiable parts of the initial data. There are a number of methods for making this separation and solving the constraints as an elliptic system. Among these are the *conformal transverse-traceless decomposition* [83]; the *physical transverse-traceless decomposition* [53, 54, 55]: and the *conformal thin sandwich decomposition* which assumes a helical killing vector [82, 30]. These methods all involve arbitrary choices, all of which have plausible physical motivation, but which do not produce equivalent data.

Until recently, most data have been constructed assuming that the initial 3-space is conformally flat. The method most commonly used is the approach of Bowen and York [12], which chooses maximal spatial hypersurfaces. The chief advantage of this approach is numerical simplicity. The choice $K = 0$ decouples the Hamiltonian constraint from the momentum constraint equations. If, besides $K = 0$, the conformal background is flat Euclidean 3-space, there are known K_{ij} that analytically solve the momentum constraints. The four constraint equations then reduce to one elliptic equation for the conformal factor ϕ. However, it has been pointed out by Garat & Price [26] that there are no conformally flat $K = 0$ slices of the Kerr spacetime. Since astrophysical sources are expected to be rotating, the choice of a conformally flat $K = 0$ background cannot represent a quiescent and rotating black hole. This process will yield data that necessarily contains some quantity of "junk" gravitational radiation. Jansen et al. [34] have shown by comparison with known solutions that conformally flat data do indeed contain a significant amount of unphysical gravitational field. Another conformally flat $K = 0$ method recently used by Gourgoulhon, Grandclement, and Bonazzola [30, 29] is a thin sandwich approximation based on the approach of Wilson and Mathews [82] which assumes the presence of an instantaneous rotation Killing vector to define the initial extrinsic curvature. Gourgoulhon et al. impose a specific gauge defined by demanding that K and the conformal factor remain constant in the rotating frame. This method solves the four initial value equations plus one additional second-order evolution equation. The assumption of a Killing

vector suppresses radiation or, perhaps more accurately, imposes a condition of equal ingoing and outgoing radiation.

The method of setting initial data used in this dissertation is the conformal transverse-traceless decomposition, described below. Rather than choosing a flat conformal background, I use Kerr-Schild data [45] as the background metric. Although this somewhat complicates the numerical solution of the constraints, there is a stronger physical motivation for choosing initial data in a conformal Kerr-Schild form. This choice is motivated by the desire to produce data which accurately represent a likely astrophysical system containing two black holes. Because the equations scale with the mass parameter, it is sufficient to solve them once. To find quantities of physical interest one then has to scale the mass to the scale under consideration. For example, stellar mass black holes and supermassive black holes in galactic centers are described by the same computation. I only consider here cases involving binary black holes. It is likely, especially in the case of merging galaxies, that a three-body interaction will occur. However, such a configuration is unstable and will result in an ejection or a merger on timescales too short to be relevant to the search for gravitational waves from such an occurrence. Therefore, although it would be computationally trivial to add a third (or more) black hole to the computational domain, it would not illuminate any matters of physical interest, so it is discarded here. A black hole may be characterized by charge and magnetic 'monopole' charge in addition to its mass and spin angular momentum. Since black holes that are expected to exist in the universe are not believed to be

charged, we also discard the possibility of charged black holes.

2.3.1 York Conformal Decomposition

This section will outline the method of solving the constraint equations by means of the conformal decomposition presented by York and collaborators [84]. For the full elliptic solution, the physical metric g_{ij} and the trace-free part of the extrinsic curvature A_{ij} are related to some background fields through a conformal factor, ϕ.

$$g_{ij} = \phi^4 \tilde{g}_{ij} \tag{2.8}$$

$$A^{ij} = \phi^{-10} \tilde{A}^{ij} \quad . \tag{2.9}$$

Here, ϕ is a scalar function to be solved for, and K and A_{ij} are respectively the trace and trace-free parts of K_{ij}:

$$K_{ij} = A_{ij} + \frac{1}{3} g_{ij} K. \tag{2.10}$$

A tilde ($\tilde{}$) indicates a background field tensor.

Since the trial extrinsic curvature does not exactly solve the momentum constraint (it has a erroneous longitudinal part), a correction to the longitudinal part, constructed from a vector w^i, to the extrinsic curvature A_{ij} is added:

$$A^{ij} \equiv \phi^{-10} (\tilde{A}^{ij} + (\tilde{lw})^{ij}) \quad , \tag{2.11}$$

where w^i is a vector potential to be solved for and

$$(\tilde{lw})^{ij} \equiv \tilde{\nabla}^i w^j + \tilde{\nabla}^j w^i - \frac{2}{3} \tilde{g}^{ij} \tilde{\nabla}_k w^k \quad . \tag{2.12}$$

Plugging Eqs. (2.8 - 2.12), into the Hamiltonian and momentum constraints (2.6 - 2.7), four coupled elliptic equations for the fields ϕ and w^i are obtained:

$$\begin{aligned} \tilde{\nabla}^2\phi &= (1/8)\big(\tilde{R}\phi + \frac{2}{3}\tilde{K}^2\phi^5 - \\ &\quad \phi^{-7}(\tilde{A}^{ij} + (\tilde{lw})^{ij})(\tilde{A}_{ij} + (\tilde{lw})_{ij})\big) \qquad (2.13) \\ \tilde{\nabla}_j(\tilde{lw})^{ij} &= \frac{2}{3}\tilde{g}^{ij}\phi^6\tilde{\nabla}_j K - \tilde{\nabla}_j\tilde{A}^{ij} \qquad (2.14) \end{aligned}$$

These elliptic equations were first solved by Marronetti and Matzner [42] with a conformal Kerr-Schild background for equal mass black holes under highly specific symmetry conditions. I have since then expanded their result to accommodate a broad generality in initial configurations – arbitrary spin, mass ratios and linear and angular momenta. Results from this code are presented in Sec. 2.7.

2.4 Setting the Superposed Background Data

This section will discuss the superposed Kerr-Schild data, how it is constructed, its utility as initial data *as is*, and motivations for choosing this particular conformal background.

2.4.1 Kerr-Schild Data for Isolated Black Holes

The Kerr-Schild [36, 35] form of a black hole solution describes the spacetime of a single black hole with mass, m, and specific angular momentum, $a = j/m$, in a coordinate system that is well behaved at the horizon. (I use

here uppercase M for calculated masses, e.g., the ADM mass, and lowercase m for mass parameters, or when the distinction is not important.) The Kerr-Schild metric is

$$\mathrm{d}s^2 = \eta_{\mu\nu}\,\mathrm{d}x^\mu\,\mathrm{d}x^\nu + 2H(x^\alpha)l_\mu l_\nu\,\mathrm{d}x^\mu\,\mathrm{d}x^\nu, \tag{2.15}$$

where $\eta_{\mu\nu}$ is the metric of flat space, H is a scalar function of x^μ, and l_μ is an (ingoing) null vector, null with respect to both the background and the full metric,

$$\eta^{\mu\nu}l_\mu l_\nu = g^{\mu\nu}l_\mu l_\nu = 0. \tag{2.16}$$

This last condition gives $l^0 l_0 = -l^i l_i$.

l^μ in Kerr and Schwarzschild spacetimes is tangent to geodesics of ingoing photons. Thus, Eq. (2.15) leads to slicing of spacetimes which penetrate the horizon. This is a desirable property for numerical work in which the singularity is excised, and fields calculated within the horizon do not propagate information outside the horizon.

The general non-moving black hole metric in Kerr-Schild form (written in Kerr's original rectangular coordinates) has

$$H = \frac{mr}{r^2 + a^2\cos^2\theta}, \tag{2.17}$$

and

$$l_\mu = \left(1, \frac{rx + ay}{r^2 + a^2}, \frac{ry - ax}{r^2 + a^2}, \frac{z}{r}\right), \tag{2.18}$$

where r, θ (and ϕ) are auxiliary spheroidal coordinates, $z = r(x, y, z)\cos\theta$, and ϕ is the axial angle. $r(x, y, z)$ is obtained from the relation,

$$\frac{x^2 + y^2}{r^2 + a^2} + \frac{z^2}{r^2} = 1, \tag{2.19}$$

giving

$$r^2 = \frac{1}{2}(\rho^2 - a^2) + \sqrt{\frac{1}{4}(\rho^2 - a^2)^2 + a^2 z^2}, \tag{2.20}$$

with

$$\rho = \sqrt{x^2 + y^2 + z^2}. \tag{2.21}$$

The non-spinning (Schwarzschild) black hole is obtained by setting $a = 0$, yielding

$$H = m/r \tag{2.22}$$

and

$$l_\mu = (r, x_i) \tag{2.23}$$

with $x_i = (x, y, z)$. Comparing the Kerr-Schild metric with the ADM decomposition (Eq. 2.3), the $t =$ constant 3-space metric is:

$$g_{ij} = \delta_{ij} + 2Hl_i l_j, \tag{2.24}$$

Further, the ADM gauge variables are

$$\beta_i = 2Hl_0 l_i, \tag{2.25}$$

and

$$\alpha = \frac{1}{\sqrt{1 + 2Hl_0^2}}. \tag{2.26}$$

The extrinsic curvature can be computed from the metric using the ADM evolution equation (Eq. 2.4).

$$K_{ij} = \frac{1}{2\alpha}[\nabla_j \beta_i + \nabla_i \beta_j - \partial_t g_{ij}], \tag{2.27}$$

Each term on the right hand side of this equation is known analytically from the four-metric.

2.4.2 Boosted Kerr-Schild Black Holes

The Kerr-Schild metric is form-invariant under a boost, making it an ideal metric to describe moving black holes. A constant Lorentz transformation (the boost velocity, $\mathbf{v}$, is specified with respect to the background Minkowski spacetime) $\Lambda^{\alpha}{}_{\beta}$ leaves the 4-metric in Kerr-Schild form, with H and l_{μ} transformed in the usual manner:

$$\begin{aligned} x'^{\beta} &= \Lambda^{\beta}{}_{\alpha} x^{\alpha}, & (2.28)\\ H'(x'^{\alpha}) &= H\left((\Lambda^{-1})^{\alpha}{}_{\beta}\ x'^{\beta}\right), & (2.29)\\ l'_{\delta}(x'^{\alpha}) &= \Lambda^{\gamma}{}_{\delta}\ l_{\gamma}\left((\Lambda^{-1})^{\alpha}{}_{\beta}\ x'^{\beta}\right). & (2.30) \end{aligned}$$

Note that l'_0 is no longer unity. As the solution before boosting is stationary, the only time dependence comes in the motion of the center. The full metric is stationary with a Killing vector reflecting the boost velocity. The solution, therefore, contains no junk radiation, as no radiation escapes to infinity during a subsequent evolution. Thus, Kerr-Schild data exactly represent a single spin-

ning and/or moving single black hole. This is not possible in other approaches, viz. the conformally flat approach as discussed in Section 2.3.

2.4.3 Background Data for Multiple Black Holes

The structure of the Kerr-Schild metric suggests a natural extension for multiple black hole spacetimes using the straightforward superposition of flat space and black hole functions

$$g_{ij} \approx \eta_{ij} + 2\ {}_1H\ {}_1l_i\ {}_1l_j + 2\ {}_2H\ {}_2l_i\ {}_2l_j + \cdots\ , \tag{2.31}$$

where the preceding subscript numbers the black holes. A simple superposition is typically not a genuine solution of the Einstein equations, because it does not satisfy the constraints. However, it should be "close" to the real solution when the holes are widely separated. On the low resolution numerical grids (grid spacing $h \sim M/4, M/6$) first used to solve the time-dependent Einstein equations for binary black holes, the magnitude of the constraint violation of superposed Kerr-Schild initial data was less than the errors associated with the second–order finite difference stencils used [41].

To generate the background data, I first choose mass and angular momentum parameters for each hole, and compute the respective H and l^α in the appropriate rest frame. These quantities are then boosted in the desired direction and offset to the chosen position in the computational frame. The computational grid is the center of momentum frame for the two holes, making the velocity of the second hole a function of the two masses and the velocity

of the first hole. Finally, the individual metrics and extrinsic curvatures in the coordinate system of the computational domain are computed:

$$
\begin{aligned}
{}_A g_{ij} &= \eta_{ij} + 2\ {}_A H\ {}_A l_i\ {}_A l_j, && (2.32)\\
{}_A K_i{}^m &= \frac{1}{2\alpha}\ {}_A g^{mj}\left(\nabla_j\ {}_A \beta_i + \nabla_i\ {}_A \beta_j - \ {}_A \partial_t g_{ij}\right). && (2.33)
\end{aligned}
$$

Again, the index A labels the black holes. Data for N holes are then constructed in superposition

$$
\begin{aligned}
\tilde{g}_{ij} &= \eta_{ij} + \sum_A^N 2\ {}_A B\ {}_A H {}_A l_i\ {}_A l_j, && (2.34)\\
\tilde{K} &= \sum_A^N {}_A B\ {}_A K_i{}^i, && (2.35)\\
\tilde{A}_{ij} &= \tilde{g}_{n(i}\ \sum_A^N {}_A B\ \left({}_A K_{j)}{}^n - \frac{1}{3}\delta_{j)}{}^n\ {}_A K_i{}^i\right). && (2.36)
\end{aligned}
$$

The extrinsic curvature is separated into its trace, K, and trace-free parts, A_{ij}, and the indices of $\tilde{A}_{ij}$ are explicitly symmetrized. The simple superposition of the metric from Eq. (2.31) (part of the original specification of Matzner, Huq, & Shoemaker [45]) has been modified here with the introduction of *attenuation functions*, ${}_A B$ [42, 41].

The attenuation functions represent the physical idea that in the immediate vicinity of one hole, the effect of a second hole becomes negligible. Near a black hole the conformal background superposition ($\tilde{}$) metrics approach the analytic values for the single black hole. The attenuation function ${}_2 B$ (${}_1 B$) eliminates the influence of the second (first) black hole in the vicinity of the

first (second). ${}_1B$ equals unity everywhere except in the vicinity of the second black hole, and its first and second derivatives are zero at the singularity of the second hole.

The attenuation function used is

$$ {}_1B = 1 - \exp(-\ell_1^4/2\sigma^2), \tag{2.37} $$

where ℓ_1 is the coordinate distance from the center of hole 2,

$$ \ell_1^2 = \frac{1}{2}(\rho^2 - a^2) + \sqrt{\frac{1}{4}(\rho^2 - a^2)^2 + a^2 z^2} \ , \tag{2.38} $$

$$ \rho = \sqrt{{}_2\gamma^2(x - {}_2x)^2 + (y - {}_2y)^2 + (z - {}_2z)^2} \ . \tag{2.39} $$

and σ is a freely-chosen parameter. In all examples given in this dissertation, the masses are equal and $\sigma = m^2$. Fig. 2.2 shows a typical attenuation function used in calculating the initial data sets.

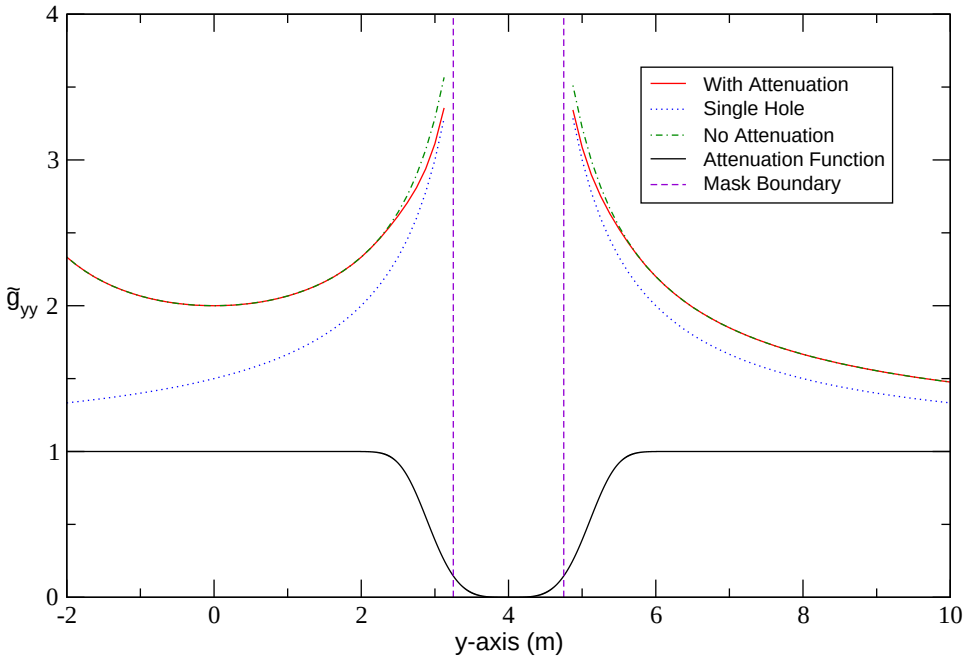

Figure 2.2: The attenuation function, ${}_1B = 1-\exp(-\ell_1^4/2\sigma^2)$, used to calculate the initial data solutions. To indicate the effect of the attenuation function in a binary black hole system, I have plotted the background metric function $\tilde{g}_{yy}$ in the vicinity of one hole with and without attenuation. The Schwarzschild black holes are placed along the y-axis at $\pm 4m$. Here ℓ_1 is the coordinate distance from the center of the second black hole, and the attenuation function width is $\sigma = m^2$.

A small volume containing the singularity is masked from the computational domain. This volume is specified by choosing a threshold value for the Ricci scalar, typically for $|R| \geq 2/m^2$. For a single Schwarzschild black hole, this gives a spherical mask with a radius $r \simeq 0.73\ m$. In all cases the masked region lies well within apparent horizons in the solved data. In practice I find that a small attenuation region (also inside the apparent horizon) is necessary to achieve a smooth solution of the elliptic initial data equations near the mask. Figures 2.3 and 2.4 show the Hamiltonian and momentum constraints for the background space with and without attenuation.

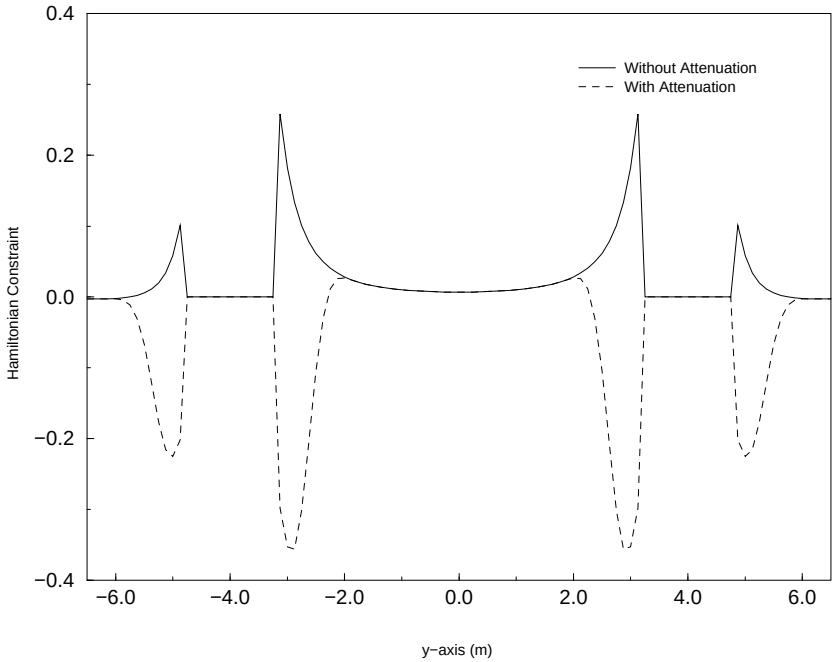

Figure 2.3: The Hamiltonian constraint (units m^{-2}) calculated for the background space for two identical Schwarzschild black holes. The black holes are located on the y-axis at $y = \pm 4$ m, and have zero initial velocity. The solid curve is the background behavior of the constraint without using attenuation functions, and the dashed curve is the constraint with attenuation and $\sigma = m^2$. The masked region is within the radius $r \lesssim 0.73m$. It can be seen that attenuation does not necessarily reduce the constraint, but does smooth it.

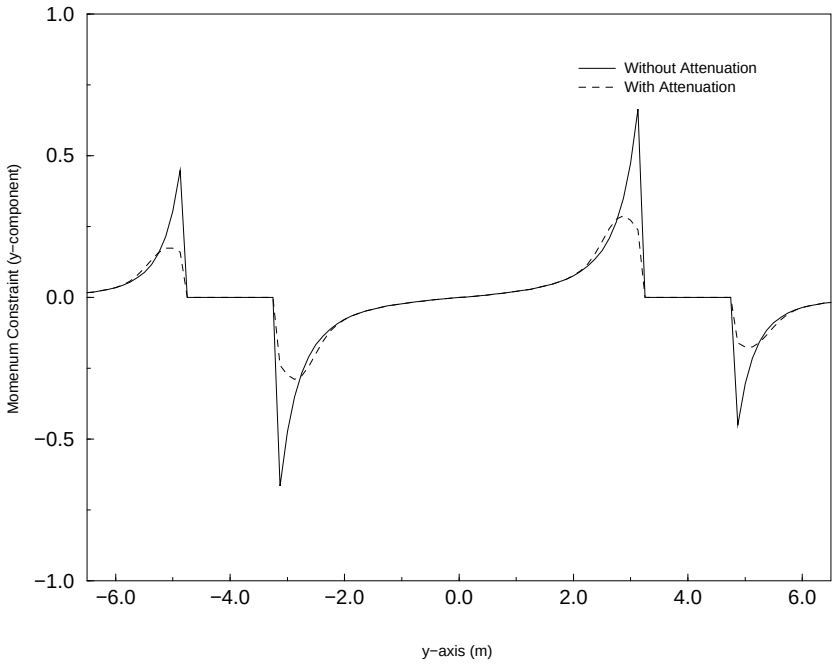

Figure 2.4: The y-component of the momentum constraint (units m^{-2}) calculated for the background space of two identical Schwarzschild black holes. The black holes are located on the y-axis at $y = \pm 4\ m$, and have zero initial velocity. The solid curve is the background behavior of the constraint without using attenuation functions, and the dashed curve is the constraint with attenuation and $\sigma = m^2$.

2.5 Solving the Constraints

2.5.1 Generating the Physical Spacetime

The superposition of Kerr-Schild data described in the previous section do not exactly satisfy the constraints, and are therefore not representative of a physical system. The physical spacetime can be constructed by modifying the background fields with new functions such that the constraints are satisfied.

The background metric, $\tilde{g}_{ij}$, the trace and trace-free part of the extrinsic curvature ($\tilde{K}$ and $\tilde{A}_{ij}$ respectively), are set according to the prescription given in Equations (2.34) - (2.36). The trace K is taken to be a given function

$$K = \tilde{K}. \tag{2.40}$$

The Hamiltonian and momentum constraint equations, expressed in terms of the background quantities $\tilde{g}_{ij}$, K, $\tilde{A}_{ij}$, the conformal factor ϕ, and the vector potential w^i Equations (2.13) - (2.14) can now be solved numerically.

I solve the constraint equations with a Chebyshev accelerated Simultaneous Over-Relaxation (SOR) elliptic solver. Pure relaxation methods converge too slowly to be of practical use. However, the solution can be anticipated, and one can over-relax the solution to converge more quickly. The parameter which governs the over-relaxation must be precisely chosen in order to obtain optimal convergence. Chebyshev acceleration is an algorithm to so choose the acceleration parameter. One begins with an acceleration parameter of 1 and gradually increases it to its optimal value as the solution progresses.

SOR methods in this way converge to a solution in a number of iterations proportional to the number of grid points [65]. While SOR methods are not the quickest and most efficient way of solving elliptic equations, they are stable, reliable, and fairly easy to code. (Work is currently in progress to adapt the initial data solver to multi-grid methods in which coarse grids are used to accelerate the convergence on fine grids.) Discrete derivatives are approximated with second order, centered derivatives. The solution is iterated until the L_2 norms of the residuals of the fields are less than some chosen value, in this case, 10^{-10} which is far below the truncation error associated with the discrete derivatives used here.

The code was parallelized using the Cactus Computational Toolkit [77], which provides a transparent means of performing parallelization, parallel I/O, and data checkpointing. Fig. 2.5 shows timing data for a sample run on a domain of 193^3 grid points. Fig. 2.6 shows the speedup for the same runs. The speedup is defined as the ratio of the time required to run the program on one processor to that required to run on N processors. A completely parallelizable code would have linear speedup with slope of unity. Linear speedup is seen for the initial data code up to about $15 - 20$ processors, although the slope is short of ideal. Calculations presented in this dissertation were typically done on eight or sixteen processors.

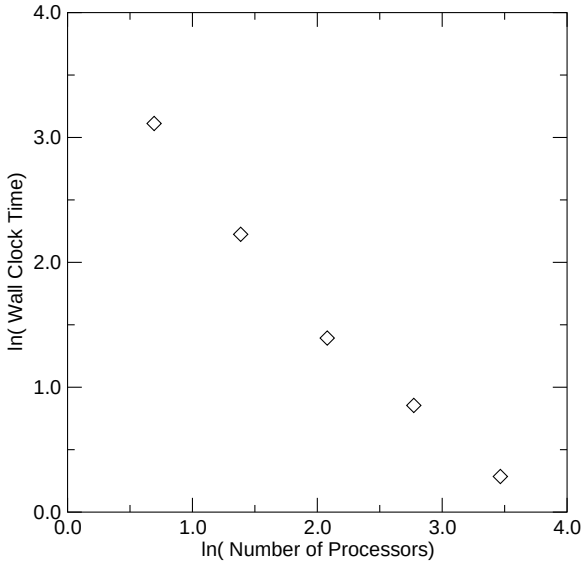

Figure 2.5: Timing data for an initial data calculation on a domain of 193^3 grid points.

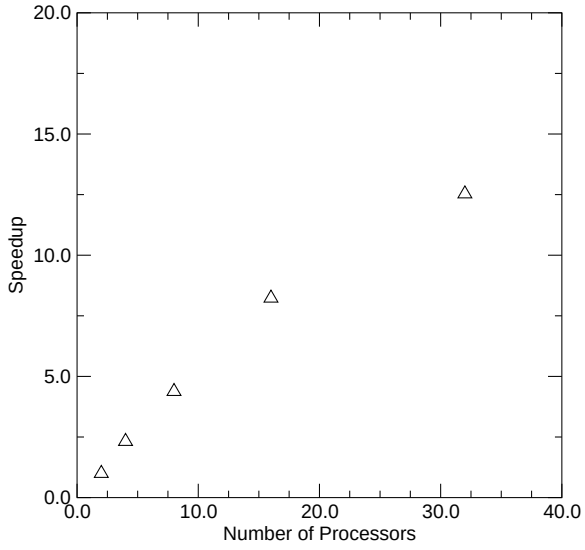

Figure 2.6: Speedup for the same initial data calculation shown in Fig. 2.5

2.5.2 Boundary Conditions

A solution of the elliptic constraint equations requires that boundary data be specified on both the outer boundary and on the surfaces of the masked regions. This contrasts with the hyperbolic evolution equations for which excision can in principle be carried out without setting inner boundary data since no information can propagate out of the holes. Boundaries in an elliptic system, on the other hand, have an immediate influence on the entire solution domain. The use of the attenuation functions allows the use of the simple conditions $\phi = 1$ and $w^i = 0$ on the masked regions surrounding the singularities. In practice this inner boundary condition is not completely satisfactory because it generates small discontinuities in the solution at this boundary. These discontinuities are small relative to the scales in the problem, and are contained within the horizon.

The outer boundary conditions are more difficult. Several physical quantities of interest, e.g., the ADM mass and momenta, are global properties of the spacetime, and are calculated on surfaces near the outer boundary of the computational grid. Therefore the outer boundary conditions must be chosen carefully to obtain the proper physics. The outer boundary conditions are based on an asymptotic expansion of the Kerr-Schild metric, which relies on the ADM mass and momentum formulæ to identify the physically relevant terms at the boundaries. These expansions and formulæ are reviewed here.

An asymptotic expansion of the Kerr-Schild metric ($\rho \gg m$) gives

$$r = \rho\left(1 + \mathrm{O}(\rho^{-2})\right), \tag{2.41}$$

$$H = m/\rho\left(1 + \mathrm{O}(\rho^{-2})\right), \tag{2.42}$$

$$l_i = n_i + \frac{a^c \epsilon_{ijc} n^j}{\rho} + \mathrm{O}(\rho^{-2}), \tag{2.43}$$

where $n_i = n^i = x^i/\rho$ and $n_i n^i = 1$. (This is the only place where the 3-metric is *not* used to raise and lower indices) a^c is the Kerr spin parameter with a general direction: $a^c = a\hat{a}^c$. The shift (Eq. 2.25) is asymptotically

$$\beta_i = \frac{2m}{\rho}\left(n_i + a^c \frac{\epsilon_{ijc} n^j}{\rho}\right) + \mathrm{O}(\rho^{-3}). \tag{2.44}$$

The asymptotic expansion of the extrinsic curvature in the stationary Kerr-Schild form (cf. Eq. (2.27)) is

$$\begin{aligned} \alpha K_{ab} = & \frac{2m}{\rho^2}\left(-2n_a n_b + \delta_{ab}\right) \\ & -\frac{3m}{\rho^3} a^c \left(\epsilon_{ajc} n_b + \epsilon_{bjc} n_a\right) n_j \\ & +\frac{6m^2}{\rho^3}\left(n_a n_b - \frac{2}{3}\delta_{ab}\right) + \mathrm{O}(\rho^{-4}). \end{aligned} \tag{2.45}$$

The terms proportional to a^c/ρ^3 in this expression arise from the transverse components of β^a ($\beta_a n^a = 0$); the terms of $\mathrm{O}(\rho^{-3})$ independent of a^c arise from the affine connection. Note that $\alpha = 1 + \mathrm{O}(\rho^{-1})$, and will not affect the ADM estimates below.

The ADM formulæ are evaluated in an asymptotically flat region sur-

rounding the system of interest; in Cartesian coordinates they are

$$M_{\rm ADM} = \frac{1}{16\pi}\oint\left(\frac{\partial g_{ji}}{\partial x^j}-\frac{\partial g_{jj}}{\partial x^i}\right)\mathrm{d}S^i, \tag{2.46}$$

$$P_k^{\rm ADM} = \frac{1}{8\pi}\oint\left(K_{ki}-K^b{}_b\delta_{ki}\right)\mathrm{d}S^i, \tag{2.47}$$

$$J_{ab}^{\rm ADM} = \frac{1}{8\pi}\oint\left(x_aK_{bi}-x_bK_{ai}\right)\mathrm{d}S^i, \tag{2.48}$$

for the mass, linear momentum, and angular momentum of the system respectively [80] (All repeated indices are summed.) The mass and linear momentum together constitute a 4-vector under Lorentz transformations in the asymptotic Minkowski space, and the angular momentum depends only on the trace-free components of the extrinsic curvature.

To compute the ADM mass and momenta for a single, stationary Kerr-Schild black hole, the integrals are evaluated on the surface of a distant sphere. The surface element then becomes $dS^i = n^i\rho^2\mathrm{d}\Omega$, where n^i is the outward normal and $\mathrm{d}\Omega$ is the differential solid angle. The metric needs to be evaluated only to order $\mathrm{O}(\rho^{-1})$; the differentiation in Eq. (2.46) guarantees that terms falling off faster than ρ^{-1} do not contribute to the integration. The integrand is then $\frac{4m}{\rho^2}n_i\rho^2n^i\,\mathrm{d}\Omega$ and the integration yields the expected ADM mass $M_{ADM} = m$. The ADM linear momentum requires only the leading order of of K_{ab}, $\mathrm{O}(\rho^{-2})$; terms falling off faster than this do not contribute. The integrand of Eq. (2.47) then becomes $-\frac{4m}{\rho^2}n_an_bn^b\rho^2\,\mathrm{d}\Omega$, yielding zero for the 3-momentum, as expected for a non-moving black hole.

The integral for the ADM angular momentum Eq. (2.48) contains K_{ab}, which to leading order is $\mathrm{O}(\rho^{-2})$. The explicit appearance of x_a in the inte-

grand suggests that it grows at infinity as $\mathrm{O}(\rho)$, leading to a divergent result. However, inserting the leading order term of K_{ab} for a single, stationary Kerr-Schild black hole into the integrand of Eq. (2.48), the integrand is found to be identically zero. The $\mathrm{O}(\rho^{-2})$ terms of K_{ab} contain the quantities $n_a n_b$ and δ_{ab}, which separately cancel because of the antisymmetric form of Eq. (2.48), and a divergent angular momentum is avoided. Including the $\mathrm{O}(\rho^{-3})$ terms of K_{ab}, I find that $J^{\mathrm{ADM}}_{ab} = \epsilon_{abc} a^c m$; the symmetry of the other $\mathrm{O}(m^2\rho^{-3})$ terms again means they do not contribute. This result for J^{ADM}_{ab} thus depends on terms in the integrand proportional to a that arise from corresponding terms in β^i proportional to q^i where q^a is a unit vector transverse to the radial direction, $q^a n_a = 0$. Only these terms contribute to the angular momentum integral; in particular those terms in β^i proportional to n^i/ρ do not contribute.

The ADM mass and momenta are Lorentz invariant. For a single, boosted black hole, one naturally obtains $M_{\mathrm{ADM}} = \gamma m$ and $P_{\mathrm{ADM}} = \gamma m v$. The background spacetime for multiple black holes is constructed with a superposition principle, and the ADM quantities are linear in deviations about flat space at infinity. Thus the ADM formulæevaluated at infinity for the superposed data do yield the expected superposition of ADM quantities. For example, given two widely separated black holes boosted in the x-y plane with spins aligned along the z-axis, one has

$$\tilde{M}_{\mathrm{ADM}} = {}_1\gamma_1 m + {}_2\gamma_2 m, \tag{2.49}$$

$$\tilde{P}^{\mathrm{ADM}}_i = 0, \tag{2.50}$$

$$\tilde{J}^{\mathrm{ADM}}_{12} = {}_1\gamma\left({}_1m_1 v_1 b + {}_1m_1 a\right) + {}_2\gamma\left({}_2m_2 v_2 b + {}_2m_2 a\right), \tag{2.51}$$

where ${}_1b$ and ${}_2b$ are impact parameters and the tilde ($\tilde{}$) superscript indicates that these quantities are calculated with the background tensors $\tilde{g}_{ab}$ and $\tilde{K}_{ab}$. This superposition principle for the ADM quantities in the background data is one advantage of conformal Kerr-Schild initial data. (Note, in choosing the center of momentum frame for the computation, $P_i^{\rm ADM} = 0$ is a condition for setting the background data.)

Consider now the ADM integrals for the solved data. The Hamiltonian constraint becomes an equation for the conformal factor, ϕ. As this equation is a nonlinear generalization of Poisson's equation, asymptotic flatness in the full, solved metric requires that

$$\phi \longrightarrow 1 + \frac{C}{2\rho} + \mathrm{O}(\rho^{-2}), \tag{2.52}$$

where C is a (finite) constant. This leads to our outer boundary condition for ϕ, namely

$$\partial_\rho \left(\rho(\phi - 1)\right) |_{\rho\to\infty} = 0. \tag{2.53}$$

Furthermore, the linearity of the ADM mass integral gives

$$M_{\rm ADM}(\text{solved}) = {}_1\gamma_1 m + {}_2\gamma_2 m + C. \tag{2.54}$$

(Here the absence of a tilde ($\tilde{}$) indicates that this mass is calculated using the solved g_{ab}.) At this point one cannot predict even the sign of C, though $|C|$ is expected to be small for widely separated holes. The results below indicate that $|C|$ is much less than the Newtonian binding energy in such cases. If $|C| \to \infty$, then the boundary condition Eq. (2.53) would fail. The existence of

solutions using this condition, however, provides evidence that this possibility does not occur.

The boundary condition for w^i is discussed below. One expects $w^i \to 0$ at infinity, but a physically correct solution on a finite domain requires an understanding of how w^i approaches this limit at infinity. The boundary conditions on w^i are constructed by demanding that the ADM angular momentum of the full (solved) system be only finitely different from that of the background (superposed) data. That is, given that $\{\tilde{g}_{ab}, \tilde{K}_{ab}\}$ and $\{g_{ab}, K_{ab}\}$ have finite differences at infinity, $J_{ab} - \tilde{J}_{ab}$ must also be finite. Using Eq. (2.9) and Eq. (2.48), the difference in angular momentum becomes

$$J_{ab} - \tilde{J}_{ab} = \frac{1}{8\pi} \oint \left(x_a \nabla_{(b} w_{i)} - x_b \nabla_{(a} w_{i)} \right) \mathrm{d}S^i \,. \tag{2.55}$$

($\phi \to 1$ at infinity, and there is no difference at this order between conformal and physical versions of w^i and g_{ab} at infinity.)

In the discussion of the Kerr angular momentum (see Eq. (2.48) and Eq. (2.45)) an integral of this form was evaluated where K_{ab} was expressed in terms of the Kerr-Schild shift vector. In that analysis, it was noted that falloff of the form

$$w_i \longrightarrow \frac{C_1}{\rho} n_i + \frac{C_2}{\rho^2} q_i + \mathrm{O}(\rho^{-3}), \tag{2.56}$$

with C_1 and C_2 constant, and $q_i n^i = 0$, will give a finite contribution to the angular momentum. The boundary conditions are therefore taken to be:

$$\partial_\rho (\rho w^i n_i) = 0 \tag{2.57}$$

$$\partial_\rho \left(\rho^2 w^i (\delta_{ij} - n_i n_j) \right) = 0 \,. \tag{2.58}$$

Figures (2.7)–(2.9) display ϕ and w^i for a simple configuration. In this case the elliptic equations were solved on a domain of $\pm 10\ m$ along each axis with resolution $\Delta x = m/8$. As can be seen in these figures, the functions ϕ and w^i actually result in little adjustment to the background configurations. The radial component of w^i, $w^i n_i$, is the dominant function. The graphs plotted here, which give the functions along the y-axis, show $||w^y||_\infty \approx 0.03$, while $||w^x||_\infty \approx 3 \times 10^{-3}$, and $||\phi - 1||_\infty \approx 0.013$. Because of the symmetry of the configuration, $||w^z||_\infty$ is much smaller. Analytically, $w^z = 0$ on the y-axis; computationally we find $||w^z||_\infty \approx 5 \times 10^{-7}$. In fact we find in general that the radial component of w^i is the dominant function in all directions, consistent with the boundary conditions, and consistent with the finding that solution of the constraints has small effect on the computed angular momentum.

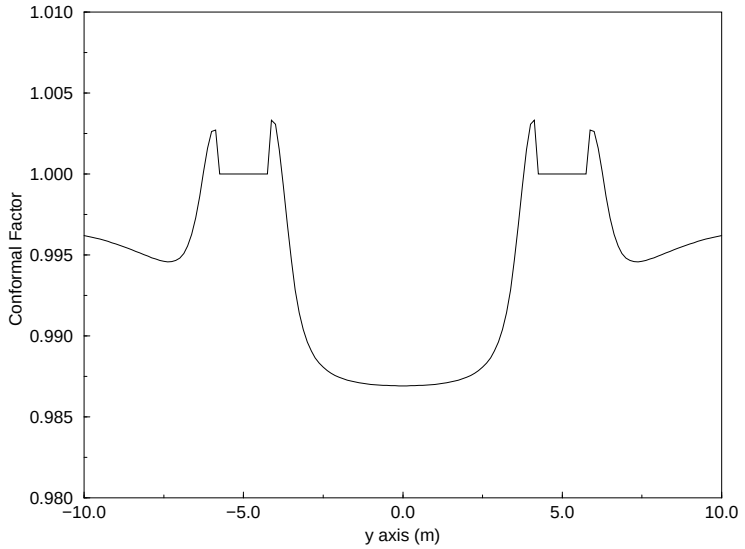

Figure 2.7: ϕ along the y-axis connecting two non-spinning holes with orbital angular momentum. The holes are boosted in the $\pm$ x direction with $v = 0.196$ and are separated by 10 M. Note that ϕ is very close to unity everywhere.

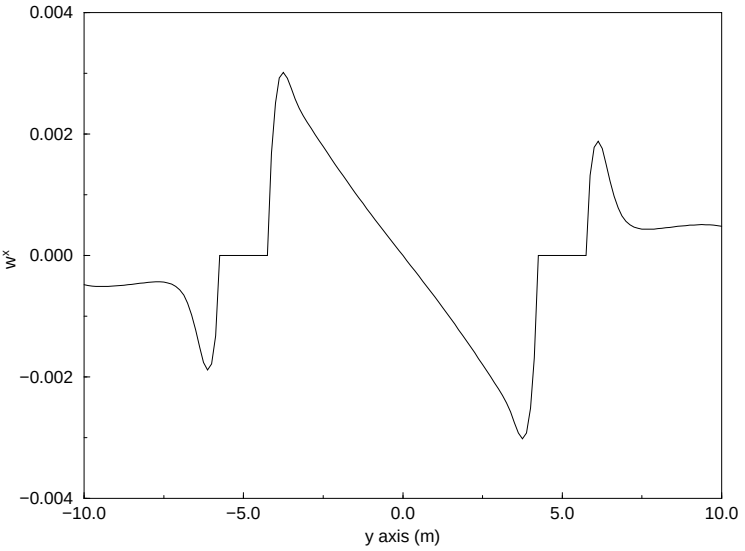

Figure 2.8: w^x for the same configuration as in Figure 2.7.

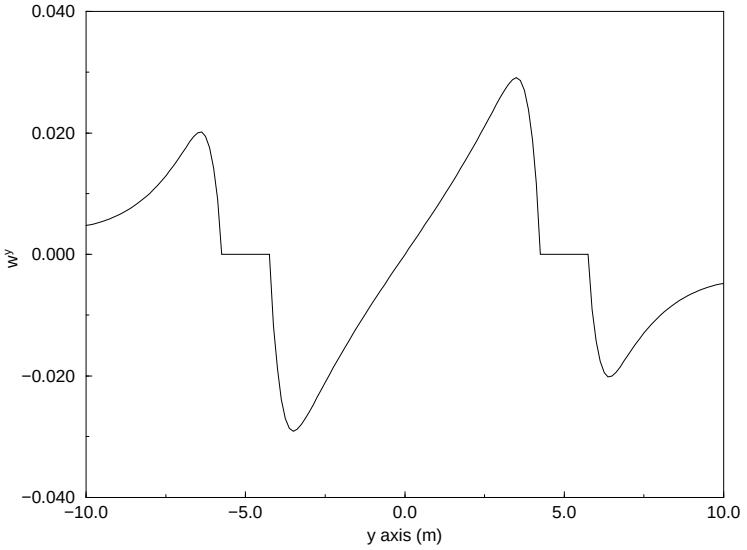

Figure 2.9: w^y for the same configuration as in Figure 2.7. w^z is numerically zero as expected by symmetry.

2.6 Analysis

This section discusses the binding energy calculations in perturbed background data. As a first step towards understanding the physical content of initial data sets, I examine in this section a perturbative calculation of the effect of the presence of a second hole on the horizon areas of a first hole and on global features such as the ADM integrals and the binding energy of the pair. This analysis is carried out for non-spinning holes to first order in the binding energy. A comparison to the Newtonian result indicates that the Kerr-Schild *background* superposition data contain the appropriate physical information at this level. I then consider at a more qualitative level possible spin-related phenomena, estimate their magnitudes, and discuss their possible effects near the ISCO.

2.6.1 Binding Energy in Brill-Lindquist Data

Before discussing the conformal Kerr-Schild data, I first consider Brill-Lindquist data for two non-moving Schwarzschild black holes [13]. These data are conformally flat, and $K_{ab} = 0$. The momentum constraints are trivially satisfied, and the Hamiltonian constraint is solved for a conformal factor: $\phi = 1 + m/(2r) + m'/(2r')$. Here the two mass parameters are m, and m', and r and r' are the distances in the flat background from the holes m and m'.

The apparent horizon areas in the solved data correspond to

$$M_{\rm AH} + M'_{\rm AH} = m + m' + \frac{mm'}{\ell} + \mathrm{O}(\ell^{-2}). \tag{2.59}$$

The subscript "AH" indicates masses computed from apparent horizon areas, and the separation in the flat background space is ℓ [15]. Assume that this mass (computed from *apparent* horizons) is close to the total intrinsic mass of the black holes (which is given by a knowledge of the spin—here zero—and the area of the *event* horizon). The binding energy, E_b, can be computed as the difference of the ADM mass observed at infinity and the sum of the horizon masses:

$$E_b = M_{\rm ADM} - M_{\rm AH} - M'_{\rm AH}. \tag{2.60}$$

For Brill-Lindquist data $M_{\rm ADM} = m + m'$, so that

$$E_b = -\frac{Gmm'}{\ell} + \mathrm{O}(\ell^{-2})\,, \tag{2.61}$$

which is the Newtonian result.

2.6.2 Binding Energy in Superposed Kerr-Schild Data

I now calculate the binding energy in superposed Kerr-Schild data (set according to the conformal transverse-traceless approach described in Sec. 2.3) for a non-moving Schwarzschild black hole at the origin, and a second such hole at coordinate distance ℓ away. (ℓ is measured in the flat space associated with the data construction.) The area of the hole at the origin is computed to first order. It is found that the Newtonian binding energy already appears in the the background data prior to solving the constraints. This is an argument justifying the result noted at the end of Sec. 2.5.2: solving the elliptic constraint equations leads to small corrections to the Kerr-Schild background data.

Let both holes be placed on the z-axis; the first hole with mass parameter m at the origin, and a second hole with mass parameter m' at $z = \ell$. The holes are well separated, and all quantities are expanded about the origin in powers of $\epsilon \equiv m'/\ell$ with $\epsilon \ll 1$. Using Schwarzschild coordinates labeled (r, θ, ϕ) (cf. Eq. (2.15)–Eq. (2.20) for $a = 0$), the background metric tensor is

$$\tilde{g}_{rr} = 1 + \frac{2m}{r} + 2\epsilon \cos^2\theta, \tag{2.62}$$

$$\tilde{g}_{r\theta} = -2\epsilon r \sin\theta \cos\theta, \tag{2.63}$$

$$\tilde{g}_{\theta\theta} = r^2 + 2\epsilon r^2 \sin^2\theta, \tag{2.64}$$

$$\tilde{g}_{\phi\phi} = r^2 \sin^2\theta, \tag{2.65}$$

with all other components zero. The extrinsic curvature of the second hole, ${}_2K_{ab}$, is of $\mathrm{O}(\epsilon^2)$ at the origin, so $\tilde{K}_{ab} = {}_1K_{ab}$. Finally, the non-zero components of $\tilde{A}_{ab}$ are

$$\tilde{A}_{rr} = -\frac{2c_2}{r^2}\left(1 + 2\frac{m}{r} + 2\epsilon\cos^2\theta\right), \tag{2.66}$$

$$\tilde{A}_{r\theta} = \epsilon\frac{c_2}{r}\sin\theta\cos\theta, \tag{2.67}$$

$$\tilde{A}_{\theta\theta} = c_2\left(1 + 2\epsilon\sin^2\theta\right), \tag{2.68}$$

$$\tilde{A}_{\phi\phi} = c_2 \sin^2\theta. \tag{2.69}$$

where

$$c_2 \equiv \frac{2M}{3}\sqrt{\frac{\rho}{\rho + 2M}}\frac{(2r + 3m)}{(r + 2m)}. \tag{2.70}$$

While $\tilde{K}_{ab}$ is not a function of ϵ, and therefore contains no information about the second hole, perturbed quantities do appear in $\tilde{A}_{ab}$. This perturbation in $\tilde{A}_{ab}$ arises because the mixed-index components of ${}_AA^c_b$ are summed, and

because the full background metric, involving terms from each hole, is involved in the symmetrization in Eq. (2.36).

To calculate the binding energy one must first find the apparent horizon area of the local hole. For a single Schwarzschild hole, the horizon is spherical and located at $\rho_{\rm H} = 2m$; the area of the horizon is $16\pi m^2$. The effect of the second hole is to distort the horizon along the z-axis connecting them. Define a trial apparent horizon surface as $f = 0$, where

$$f = \rho - 2m - \sum_l a_l P_l(\cos\theta)\,. \tag{2.71}$$

The expansion of f in Legendre polynomials, P_l, expresses the distortion of the local horizon away from the zero-order spherical result. This expansion includes a term describing a constant "radial" offset in the position of the apparent horizon, $a_0 P_0$. This and the other terms defining the surface have the expected magnitude, $a_l = {\rm O}(m\epsilon)$. The horizon is solved for by placing this expression for the surface into the apparent horizon equation

$$\nabla_i s^i + A_{ab} s^a s^b - \frac{2}{3} K = 0, \tag{2.72}$$

where s^i is the unit normal to the trial surface

$$s_i = \frac{f_{,i}}{\sqrt{g^{ab} f_{,a} f_{,b}}}. \tag{2.73}$$

The apparent horizon equation is solved to first order, ${\rm O}(\epsilon)$. One must evaluate the equation at the new (perturbed) horizon location. Let F represent the left-hand side of the apparent horizon equation (Eq. (2.72)). $\rho_0 = 2m$ is the

horizon surface of the single, unperturbed hole, and $\rho_{\rm H}(\theta)$ is the new perturbed horizon. F is expanded to first order as

$$F(\rho_{\rm H}(\theta)) = F_0(\rho_0) + \left.\frac{\partial F}{\partial \rho}\right|_{\rho_0} \sum a_l P_l \; = 0. \tag{2.74}$$

Solving (Eq. (2.72)), the only nonzero coefficients in Eq.(2.71) are $a_0 = mm'/(3\ell)$, $a_2 = -mm'/(2\ell)$. Integrating the determinant of the perturbed metric over the horizon surface, $\rho = 2m + \sum_l a_l P_l(\cos\theta)$, the area of the apparent horizon is found to be

$$A_{\rm H} = 16\pi \left(m + \frac{mm'}{2\ell}\right)^2 + {\rm O}\left(m^2(m'/\ell)^2\right), \tag{2.75}$$

corresponding to a horizon mass of $M_{\rm H} = m + mm'/(2\ell)$ to Newtonian order, i.e. to order ${\rm O}(\epsilon) = {\rm O}(\ell^{-1})$.

In this non-moving case the total ADM mass is just $M_{\rm ADM} = m + m'$. This leads to the Newtonian binding energy at this order

$$E_b = -\frac{mm'}{\ell}. \tag{2.76}$$

Because this was carried out only to lowest order in ϵ, Eq. (2.76) had to result in an expression of ${\rm O}(m\epsilon)$, but it did not have to have a coefficient of unity.

Thus, I have demonstrated that both the conformally flat and conformally Kerr-Schild data contain the Newtonian binding energy. However, this result is obtained in the superposed *background* Kerr-Schild metric, while the

Brill-Lindquist data give the correct binding energy only after solving the elliptic constraints. This is also consistent with the small corrections introduced by ϕ and w^i ($\phi \sim 1$, $|w^i| \ll 1$) in the solved Kerr-Schild data (see Sec. 2.5.2).

Furthermore, the Newtonian form of the binding energy ($\epsilon \ll 1$) means that the correct classical total energy is found for orbiting situations. If the holes have non-relativistic motion, their individual masses are changed by order $\gamma \approx 1 + \mathrm{O}(v^2) = 1 + \mathrm{O}(\epsilon)$. The binding energy, which is already $\mathrm{O}(\epsilon)$ and is proportional to the product of the masses, is changed only at order $\mathrm{O}(\epsilon^2)$. The ADM mass, on the other hand, measures γm, and M_{ADM} will be increased by $mv^2/2$ (an $\mathrm{O}(\epsilon)$ increase) for each hole, leading to the correct Newtonian energetics for the orbit.

The apparent horizon is the only structure available to measure the intrinsic mass of a black hole. For a spinning hole, the intrinsic spin of the black hole is a complication; the relation is between horizon area and *irreducible* mass:

$$A_{\mathrm{H}} = 16\pi m_{irr}^2 = 8\pi m \left(m + \sqrt{(m^2 - a^2)} \right) \tag{2.77}$$

As Eq. (2.77) shows, the irreducible mass is a function of both the mass and the spin, and in a general superposition it is not possible to specify the spin of the black holes.

2.6.3 Spin effects in Approximating Inspiral with Initial Data Sequences

The initial data contain the binding energy in a multiple black hole spacetime. This information can be used to deduce some characteristics of the orbital dynamics, particularly the radius of the circular orbit, ℓ, and the orbital frequency, ω. Given a sequence of initial data slices with decreasing separations, one can determine E_b for each slice. The circular orbit is found where

$$\left.\frac{\partial E_b}{\partial \ell}\right|_J = 0. \tag{2.78}$$

The separation at the ISCO orbit, $\ell_{\rm ISCO}$, lies at the boundary between binding energy curves which have a minimum, and those that do not. The curve for the ISCO has an inflection point:

$$\left.\frac{\partial^2 E_b}{\partial \ell^2}\right|_J = 0. \tag{2.79}$$

The angular frequency is given by

$$\omega_{\rm ISCO} = \frac{\partial E_b}{\partial J}. \tag{2.80}$$

The attempt to model dynamical inspiral seems secure for large separation ($\ell > 15m$), though surprises appear even when the holes are very well separated. For instance, Eq. (2.75) above shows that compared to the bare parameter values, the mass increase is equal for the two holes in a data set. Thus the smaller hole is proportionately more strongly affected than the larger one is.

The physically measurable quantity in question is the frequency (at infinity) Eq. (2.80) associated with the last orbit prior to the plunge, the ISCO. This may be impossible to determine from the initial data alone.

To begin with, isolated black holes form a 2-parameter set (depending on the mass parameter m, and the angular momentum parameter, $j = ma$). For isolated black holes without charge the parameters $\{m, j\}$ uniquely specify the hole. They are equal, respectively, to the physical mass and physical angular momentum. Every method of constructing multiple black hole data assigns parameter values ${}_Bm$ and ${}_Bj$ to each constituent ${}_B(hole)$ in the data set.

There is substantial ambiguity involving spin and mass in setting the black hole data. One must consider the evolutionary development of the black hole area and spin. A related concern arises because it is only the total ADM angular momentum that is accessible in the data, whereas one connects to particle motion via the orbital angular momentum.

For example, one can consider the behavior of the individual black hole spin and mass in an inspiral. For widely separated holes, because the spin effects fall off faster with distance than the dominant mass effects do, the spin ought to be approximately conserved in an inspiral. Therefore it should also be constant across the initial data sets representing a given sequence of orbits. But when the holes approach closely, the correct choice of spin parameter becomes problematic also.

Newtonian arguments demonstrate some of the possible spin effects. In every case they are *a priori* small until the orbits approach very closely. However, at estimates for the ISCO, the effects begin to be large, and result in ambiguities in setting the data [66]. I consider these effects in decreasing order of their magnitude.

For two holes, each of mass m in Newtonian orbit with a total separation of ℓ, the orbital frequency is

$$m\omega = \sqrt{2}(m/\ell)^{(3/2)}. \tag{2.81}$$

From recent work by Pfeiffer et al. [64], the estimated ISCO frequency is of order $m\Omega = 0.085$, corresponding to $\ell \approx 6.5\, m$ in this Newtonian approach. To compare this frequency, Eq. (2.81), to an intrinsic frequency in the problem, take the lowest (quadrupole) quasi-normal mode of the final merged black hole (of mass $2m$) which has frequency $2m\omega_0 \approx 0.37$; the quadrupole distortion is excited at twice the orbital frequency. The driving frequency equals the quasi-normal mode frequency when $\ell \approx 4\, m$, as might be expected.

To consider effects linked to the orbital motion on the initial configurations, one first treats the effect of imposing co-rotation. While co-rotation is not physically enforced except for very close orbits, as shown below, certain formulations, for instance versions of the "thin sandwich" with a helical Killing vector, require co-rotation in their treatment. Nevertheless, for any particular initial orbit, co-rotation is a possible situation.

In co-rotation, then, with Eq. (2.81), for each hole:

$$J = ma = I\omega = 4m^2(m\omega). \tag{2.82}$$

The result for the moment of inertia $I = 4m^3$ is the Schwarzschild value [51, 76]. Thus

$$a = 4m\sqrt{2}(m/\ell)^{(3/2)}. \tag{2.83}$$

Assume $a/m \ll 1$, and compute the area of this black hole [51]:

$$A = 8\pi m(m + \sqrt{m^2 - a^2}) \approx 16\pi m^2(1 - (a/m)^2/4). \tag{2.84}$$

The horizon mass computed from this area is

$$\sqrt{A/(16\pi)} \approx m(1 - 4(m/\ell)^3). \tag{2.85}$$

At the estimated the ISCO orbit, $\ell_{\rm ISCO} \approx 6\,m$, this effect is of order of 10% of the Newtonian binding energy, distinctly enough to affect the location of the ISCO.(At $\ell_{\rm ISCO} \approx 6\,m$, $a/m \approx 0.3$ for co-rotation).

Two more physical effects are not typically considered in setting data. They are *frame dragging*, and *tidal torquing*. Within the Newtonian approximations, these effects are small, but not zero as the orbits approach the ISCO. In full nonlinear gravity these effects could be substantial precisely at the estimated ISCO.

The frame dragging is the largest dynamical effect. The orbiting binary possesses a net angular momentum. For a rotating mass (here the complete

binary system) the frame dragging angular rate is estimated as the rotation rate times the gravitational potential at the measurement point [51]. Hence

$$m\Omega_{\rm drag} = m\omega\left(\frac{2m}{\ell}\right) \approx \left(\frac{m}{\ell}\right)^{\frac{5}{2}} \approx \frac{a}{4m}. \tag{2.86}$$

This is a/m of order 1% at $\ell = 10m$; of order 4% at $\ell = 6m$.

The tidal torquing and dissipative heating of the black holes can be similarly estimated. As the two holes spiral together, the tidal distortion from each hole on the other will have a frequency which is below, but approaching the quasi-normal frequency. Just as for tidal effects in the solar system, there will be lag in the phase angle of the distortion, which can be determined because the lowest quasi-normal mode is a dissipative oscillator, driven through the tidal effects at twice the orbital frequency:

$$\ddot{q} + 2\gamma\dot{q} + \omega_0^2 q = F(\omega). \tag{2.87}$$

Here $m^2 q$ is the quadrupole moment of the distorted black hole. The parameter γ is (for a Schwarzschild hole of mass $2m$)) about $2m\gamma = 0.089$. In Eq. (2.87) the driving acceleration $F(\omega)$ is identified with the tidal distortion acceleration. Evaluated at zero frequency:

$$q = F(\omega = 0)/\omega_0^2 \tag{2.88}$$

$$\approx \frac{m}{\ell^3}. \tag{2.89}$$

The lagging phase, for driving frequency $2\omega \ll \omega_0$, is easily computed to be

$$\phi \approx 4\gamma\frac{\omega}{\omega_0^2} \tag{2.90}$$

$$= 4\left(\frac{\gamma}{\omega_0}\right)\left(\frac{\omega}{\omega_0}\right) \tag{2.91}$$

This lagging tidal distortion will produce a tidal torque on the black hole, which can be approximated using a combination of Newtonian and black hole ideas. The most substantial approximation is that the torque arises from a redistribution of the mass in the "target" black hole, of amount $\Delta m = mm^2q = m(m/\ell)^3$. This mass has separation $\approx 4m$. Thus the torque on the hole is

$$\begin{aligned}
\tau &= \sin\phi \times (\text{lever arm}) \times \Delta F \qquad (2.92)\\
&= \sin\phi \times (4m) \times (\Delta m 2m^2/\ell^3)\\
&= 8\sin\phi m(m/\ell)^6\\
&\approx 32(\gamma/\omega_0)(\omega/\omega_0)m(m/\ell)^6\\
&\approx 60m(m/\ell)^{15/2}.
\end{aligned}$$

Most important is the effect of this torque on the angular momentum of the hole over the period of time it takes the orbit to shrink from a very large radius. To evaluate this, the inspiral rate is calculated under the assumption of weak gravitational radiation from the orbit (following [51]):

$$\frac{d\ell}{dt} = -\frac{128}{5}\left(\frac{m}{\ell}\right)^3 \qquad (2.93)$$

Thus

$$\begin{aligned}
\frac{dJ}{d\ell} &= \tau\frac{dt}{d\ell} \qquad (2.94)\\
&= -\frac{5\tau}{128}\left(\frac{m}{\ell}\right)^{-3} \qquad (2.95)\\
&\approx -2m\left(\frac{m}{\ell}\right)^{9/2}, \qquad (2.96)
\end{aligned}$$

and

$$J(\ell) \approx m^2 \left(\frac{m}{\ell}\right)^{7/2}; \tag{2.97}$$

assuming that there is minimal mass increase from the associated heating, this identifies the induced spin parameter $a = m(m/\ell)^{7/2}$ for an inspiral from infinity.

The estimate $a = m(m/\ell)^{7/2}$ for an inspiral from infinity assumes the mass of the hole has not changed significantly in the inspiral. By considering the detailed behavior of the shear induced in the horizon by the tidal perturbation, the growth in the black hole mass can be estimated [76] as

$$\frac{dm}{dt} = \omega \frac{dJ}{dt}, \tag{2.98}$$

leading to a behavior

$$\Delta m(\ell) \approx 5m \left(\frac{m}{\ell}\right)^5; \tag{2.99}$$

Consequently, the change in mass can be ignored until the holes are quite close. However, the Newtonian estimates lead to possible strong effects just where they become unreliable, and just where they would affect the ISCO.

These results are consistent with similar ones of Price and Whelan [66], who estimated tidal torquing using a derivation due to Teukolsky [75]. That derivation assumes the quadrupole moment in the holes arises from their Kerr character, which predicts specific values for the quadrupole moment, as a function of angular momentum parameter a.

Finally, I consider an effect on binding energy shown by Wald and also by Dain [79, 21]. Wald directly computes the force for stationary sources with

arbitrarily oriented spins. He considered a small black hole as a perturbation in the field of a large hole. The result found was

$$E_b = -\frac{mm'}{\ell} - \left(\frac{\vec{S} \cdot \vec{S}' - 3(\vec{S} \cdot \hat{n})(\vec{S}' \cdot \hat{n})}{\ell^3} \right). \tag{2.100}$$

Here, $\vec{S}$, $\vec{S}'$ are the spin vectors of the sources and $\hat{n}$ is the unit vector connecting the two sources. Dain [21], using a definition of intrinsic mass that differs from the one used here, finds binding energy which agrees with Wald's Eq. (2.100) at $O(\ell^{-3})$. This is discussed further in Section 2.7.

2.7 Results

To verify the solution of the discrete equations one must examine the code's convergence in some detail. The constraints have known analytical solutions—they should be zero—which allows a determination of the code's convergence using a solution calculated at two different resolutions. Let S_1 be a solution calculated with resolution h_1, and S_2 be a solution calculated with h_2, then the convergence factor c_{12} is

$$c_{12} = \frac{\log\left(\frac{||\mathrm{S_1}||}{||\mathrm{S_2}||}\right)}{\log\left(\frac{\mathrm{h_1}}{\mathrm{h_2}}\right)} \tag{2.101}$$

A conformal background spacetime with two $m = 1$ non-spinning black holes separated by $6m$ on the y-axis was constructed. The elliptic equations were then solved on grids with resolutions of $m/6$, $m/8$, $m/10$ and $m/12$, which is a sufficient spread of resolution to determine the order of convergence. Tables 2.7–2.7 show the convergence factors as a function of resolution for the Hamiltonian constraint and the x-component of the momentum constraint, $\mathcal{C}^x$. The convergence for $\mathcal{C}^y$ is nearly identical to $\mathcal{C}^x$, and as the y-axis is an axis of symmetry, $\mathcal{C}^z$ is identical to $\mathcal{C}^x$. Figures 2.10–2.12 show the convergence behavior of the constraints along coordinate lines. The constraints calculated at lower resolutions are rescaled to the highest resolution by the ratio of resolutions squared. The code shows second order convergence for all components with the exception of those points nearest to the inner boundary.

Convergence (c_{ab})			
	$a = m/6$	$a = m/8$	$a = m/10$
$b = m/8$	1.70		
$b = m/10$	1.77	1.86	
$b = m/12$	1.79	1.86	1.85

Table 2.1: Convergence data for the Hamiltonian constraint, $\mathcal{C}^0$, for a solution with two $m = 1$, non-spinning holes at $x^i = (0, \pm 3m, 0)$ in the conformal background, and outer boundaries at $x^i = \pm 6m$. The solution was calculated at resolutions $m/6$, $m/8$, $m/10$, and $m/12$. The L_2 norms of $\mathcal{C}^0$ were calculated over the entire volume of the domain using a mask of radius $1m$ around each hole, while the computational mask has a radius of approximately 0.75 m. This larger mask was used to compensate for the slight difference of physical location of the mask at different resolutions. The norms are as follows: $||\mathcal{C}^0(m/6)||_2 = 0.00389054$, $||\mathcal{C}^0(m/8)||_2 = 0.00238321$, $||\mathcal{C}^0(m/10)||_2 = 0.00157387$ and $||\mathcal{C}^0(m/12)||_2 = 0.00112328$.

Convergence (c_{ab})			
	$a = m/6$	$a = m/8$	$a = m/10$
$b = m/8$	1.93		
$b = m/10$	1.99	2.06	
$b = m/12$	1.99	2.03	1.99

Table 2.2: Convergence data for the x-component of the momentum constraint, for the same configuration as Table 2.7. The norms of $\mathcal{C}^x$ are as follows: $||\mathcal{C}^x(m/6)||_2 = 0.00541231$, $||\mathcal{C}^x(m/8)||_2 = 0.00310937$, $||\mathcal{C}^x(m/10)||_2 = 0.00196156$ and $||\mathcal{C}^x(m/12)||_2 = 0.00136514$. Convergence factors were also calculated for $\mathcal{C}^y$ and $\mathcal{C}^z$, and found to be essentially identical to the data shown here, and thus are not given separately.

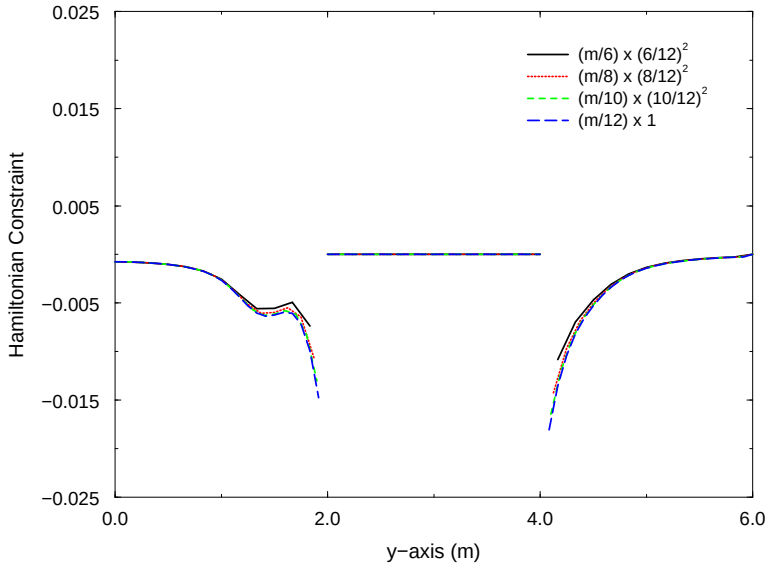

Figure 2.10: The Hamiltonian constraint (units m^{-2}) along y-axis after solving the elliptic equations for 4 different levels of resolution. The constraints are rescaled by the ratio of the resolutions squared, showing second order convergence. The two non-spinning, instantaneously stationary holes of $m = 1$ are positioned at ± 3 on the y-axis.

Domain	M_{ADM}
$\pm$ 8 m	1.942 m
$\pm$ 10 m	1.964 m
$\pm$ 11 m	1.974 m
$\pm$ 12 m	1.980 m

Table 2.3: Total ADM Mass for two instantaneously stationary, non-spinning holes separated by $6m$ on a grid of discretization $\Delta x = m/8$ for four different domain sizes.

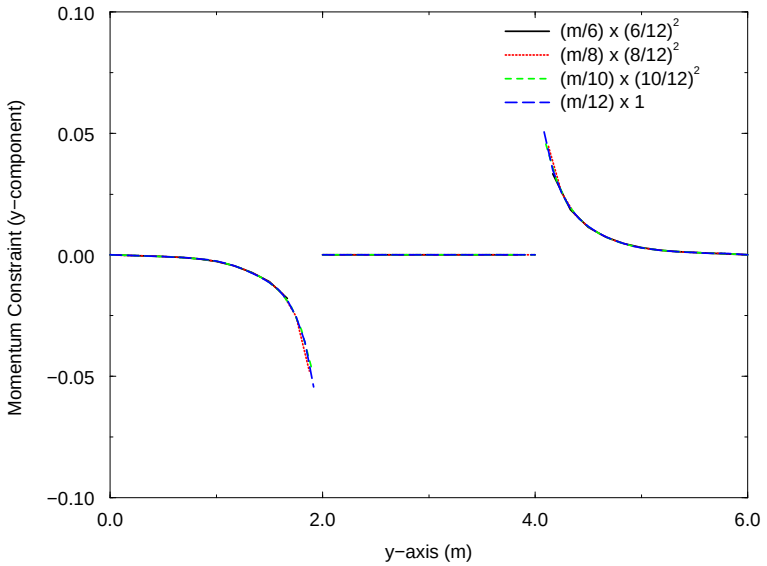

Figure 2.11: y-component of momentum constraint (units m^{-2}) along the y-axis after solving the elliptic equations for 4 different levels of resolution, showing second order convergence. The background physical situation is the same as in Figure (2.10). The other momentum constraint components evaluated on this axis are zero by symmetry, both analytically, and computationally ($O(10^{-12})$).

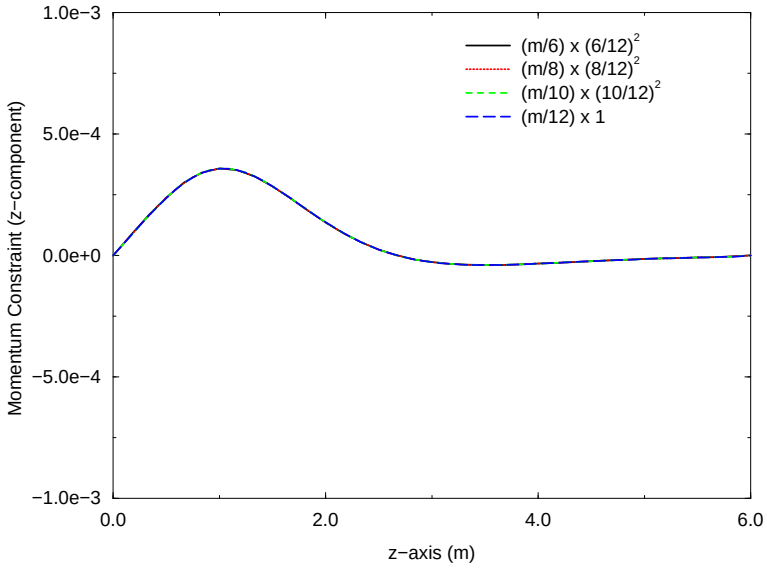

Figure 2.12: z-component of momentum constraint (units m^{-2}) along the z-axis after solving the elliptic equations for 4 different levels of resolution, showing second order convergence. Other components of the momentum constraint evaluated along this line are zero by symmetry, both analytically and computationally ($O(10^{-12})$). The background physical situation is the same as in Figure (2.10). The behavior of the x-momentum constraint along the x-axis is identical to this figure, as required by the symmetry of the problem.

Solutions of elliptic equations are well-known to be dependent on all boundary data. The outer boundary is an artificial boundary, since the physical spacetime is unbounded. Boundary data for this outer boundary are derived from the asymptotic behavior of a single Kerr black hole. On very large domains these conditions should closely approximate the expected field behavior, but on small domains these boundary data only nearly approximate the real solution. This error in the boundary data then contaminates the entire solution, as expected for elliptic solutions. Additional error arises in the calculation of the ADM quantities which are surface integrals to be evaluated at infinity but are instead evaluated near the outer boundary which does not approach asymptotic flatness. As an indication of the error associated with the artificial outer boundaries, I calculated solutions with the same physical parameters on grids of differing sizes. The boundary effects in the $M_{\rm ADM}$ are given in Table 2.3, and Fig. 2.13 shows a contour plot of ϕ for equal mass, non-spinning, instantaneously stationary black holes with the outer boundaries at $x^i = \pm 12m$. As a further demonstration of boundary effects in the solutions, Fig. 2.14 shows ϕ for a configuration examined by Pfeiffer *et al.* [62]. Their solution, shown in Fig. 8 of [62], was computed on a much larger domain via a spectral method [63]. Thus, while I have achieved reasonable results, it is important to remember that the boundary effects may be significant. Moreover, I have only considered the effect of outer boundaries, while errors arising from the approximate inner boundary condition have not been examined.

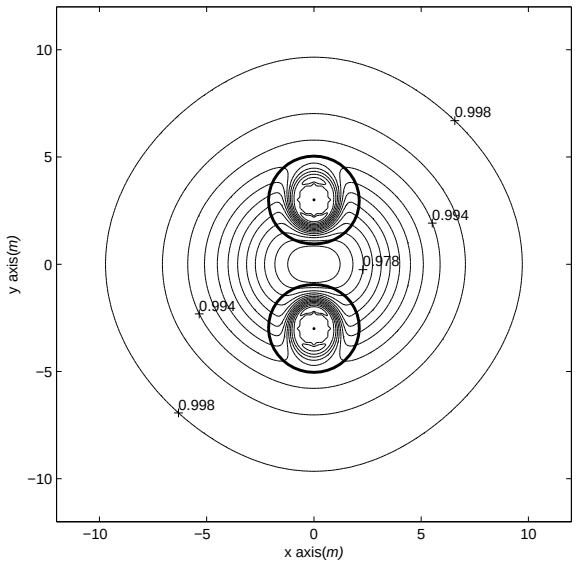

Figure 2.13: Contour plot of ϕ for two instantaneously stationary, non-spinning holes of mass parameter $m = 1$. The holes are separated by 6 m along the y-axis. The bold circles indicate the apparent horizons.

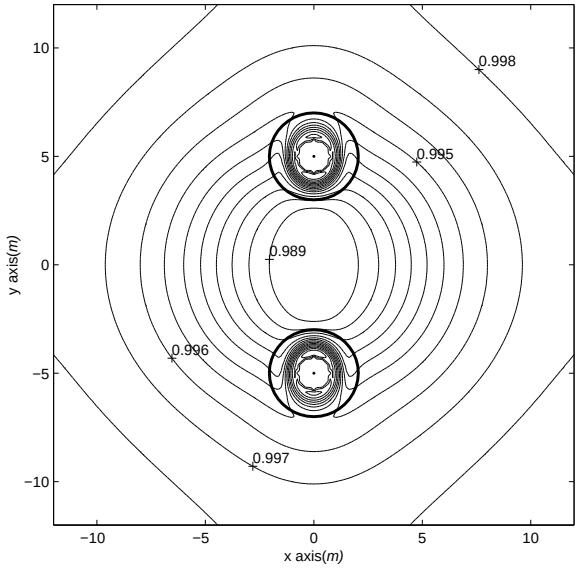

Figure 2.14: Contour plot representing the same configuration as Fig. 2.13 but with the holes separated by 10 m along the y-axis. The outermost contour here shows some effect from the boundaries. Compare to Figure 8 in ref. [62] .

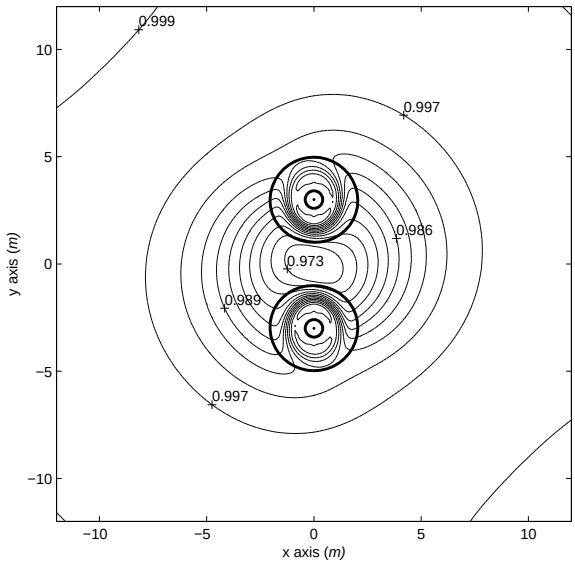

Figure 2.15: Conformal factor ϕ for two instantaneously stationary holes separated by $6m$ with spin parameter $a = 0.5$. The spins are parallel and pointed out of the page. Compare to Fig. 2.13. Also notice the boundary effect on the outermost contour, labeled 0.999.

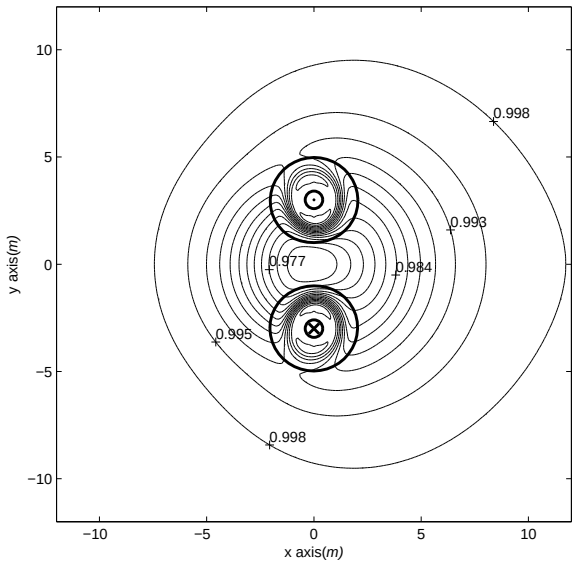

Figure 2.16: Conformal factor ϕ for the same configuration as Fig. 2.15 except the spins are anti-parallel: the spin of the hole at $(0, -3, 0)$ points into the page.

Other derived quantities also show convergence. $M_{\rm ADM}$ is computed from Eq. 2.54, using the known background quantity and computing the correction C due to the $1/r$ contribution from the conformal factor to the integral. The actual integral numerically computed on the surface of the domain is

$$C = \frac{1}{16\pi} \oint 4\phi^3 \left((\partial_j \phi) \tilde{g}_{ji} - (\partial_i \phi) \tilde{g}_{jj} \right) dS^i \tag{2.102}$$

Fig. 2.17 shows the ADM mass $M_{\rm ADM}$ for two non-spinning black holes at $6m$ separation, and different resolutions. The fit is

$$M_{ADM} = \left(1.941 + 0.067 \left(\frac{\Delta x}{m} \right) - 0.422 \left(\frac{\Delta x}{m} \right)^2 \right) m. \tag{2.103}$$

showing good second order convergence. The angular momentum calculation is less robust, but exhibits approximately first order convergence. The fit to Figure 2.18, which shows J^{ADM} for two non-spinning holes with orbital angular momentum, gives:

$$J_{12}^{ADM} = \left(1.837 - 0.121 \left(\frac{\Delta x}{m} \right) + 0.237 \left(\frac{\Delta x}{m} \right)^2 \right) \epsilon_{12} m^2. \tag{2.104}$$

Compare this to the angular momentum computed for the background: $\tilde{J}_{12}^{ADM} = 2.0m^2$.

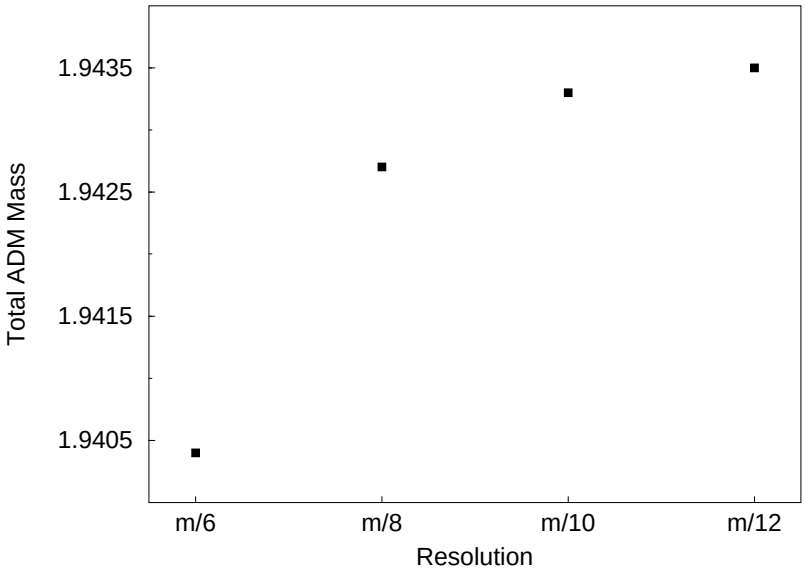

Figure 2.17: The total ADM energy for two momentarily stationary non-spinning black holes separated by $6m$ at various resolutions. The results exhibit second order convergence.

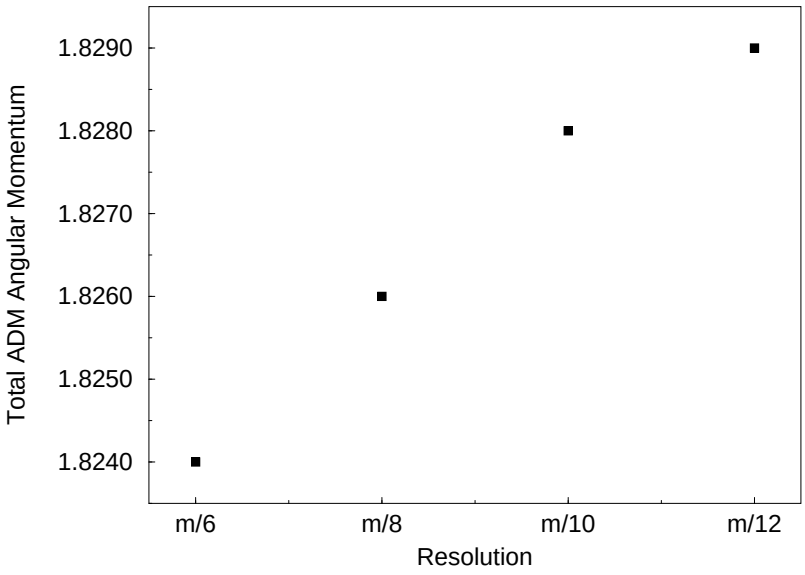

Figure 2.18: The total ADM angular momentum for two non-spinning holes boosted in the $\pm$ x direction with $v = 0.3162$ and separated by $6m$ at various resolutions (background angular momentum $\tilde{J}_{12}^{ADM} = 2.0m^2$).

The small computational domain does not negate the utility of these solutions as initial data for the time-dependent Einstein equations. For instance, Figures 2.19 and 2.20 show data for grazing and elliptical orbits. They have been incorporated into earlier versions of a binary black hole evolution code. While the small domains do mean that that the data do not represent the best asymptotically flat results available from this method, some of the qualitative analytical predictions of the previous section can still be verified. In particular, Figures 2.13, 2.15, and 2.16 show the conformal factor ϕ for holes instantaneously at rest at a separation of $6m$. In Figure 2.13 they are non-spinning; in Figures 2.15 and 2.16, each has Kerr parameter $a = 0.5m$. In one case (Fig. 2.15) the spins are aligned; in the other (Fig. 2.16) they are anti-aligned. Table 2.4 gives the values of the apparent horizon area of each hole, the ADM mass, and the binding energy fraction for these configurations. The binding energy is consistent with the analytic estimates of Wald [79] in Section 2.6.3.

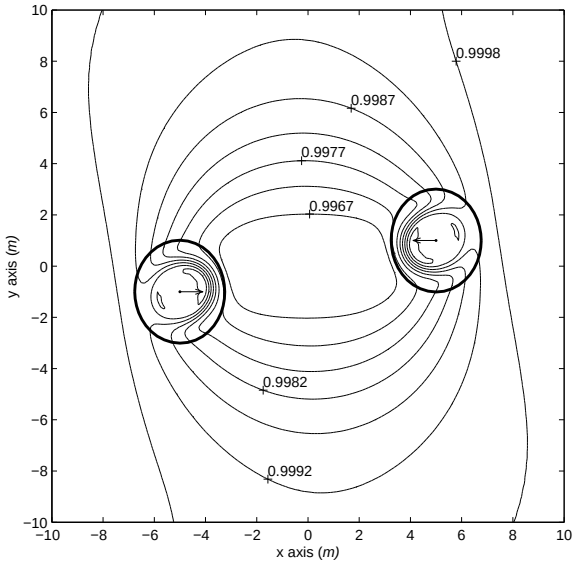

Figure 2.19: ϕ for a grazing collision between two equal mass, non-spinning holes. The holes are centered at $y = \pm 1m$ and boosted toward each other with $v_x = \mp 0.5c$, respectively.

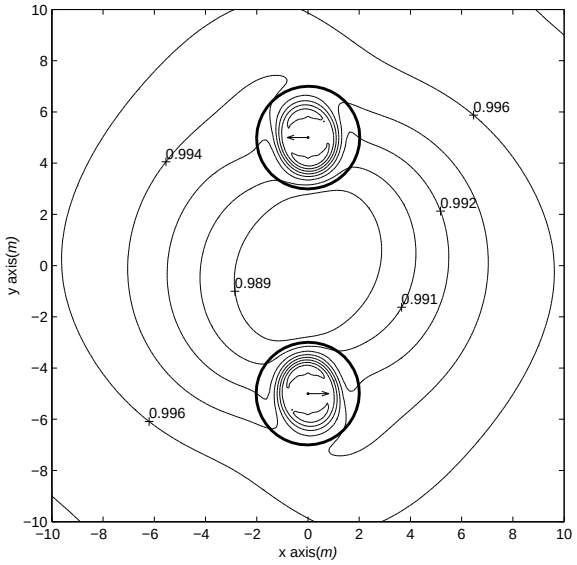

Figure 2.20: ϕ for two non-spinning holes boosted perpendicularly to their separation. The holes are separated by $10m$ and boosted with $v_x = \pm 0.196$, giving the system a background angular momentum of $\tilde{J}_{12}^{ADM} = 2.0m^2$. The calculated $J_{12}^{ADM} = 1.91m^2$ and $M_{ADM} = 1.970m^2$. The Newtonian data correspond to an elliptic orbit at apastron.

Wald's computation of the binding energy for spinning holes, Eq. (2.100), gives for parallel or anti-parallel spins orthogonal to the separation (as in my computational models):

$$E_b = -\left(\frac{mm'}{\ell} + \frac{\vec{S}\cdot\vec{S'}}{\ell^3}\right) \tag{2.105}$$

with oppositely directed spins showing *less* binding energy. For the $S = 0.5\,m^2$, $\ell = 6\,m$ configuration, this is a change of order $\mathrm{O}(2\times10^{-3})$ between the parallel and the anti-parallel cases. Evaluating the computational results, as in Table 2.4, for the spinning cases there is a change in binding energy between parallel and anti-parallel spins of approximately half that, with the correct sign. This rough correspondence to the analytic result is promising; however, the non-spinning case deviates from the expectation that its binding energy should be between that of the spinning cases. Within the accuracy of the solution, given the limited domain size available, a clearer dependence of binding energy on spin cannot be shown.

	$A^{\dagger}_{AH}$	M_{ADM}	$M^{\dagger}_{AH}$	Binding Energy
Parallel Spin	53.20	1.973	1.065	-0.157 = -0.147 $\times M_{AH}$
Anti-parallel Spin	53.17	1.974	1.065	-0.156 = -0.146 $\times M_{AH}$
Zero Spin	57.10	1.980	1.066	-0.151 = -0.142 $\times M_{AH}$

Table 2.4: M_{ADM}, A_{AH} and associated quantities calculated for two holes with $m = 1.0$ on a grid $(24\ m)^3$ with resolution $\Delta x = m/8$. †: Quantity for a single hole.

2.8 Conclusions

Initial data based on background superposition of Kerr-Schild black holes has been constructed, and I have analyzed the physical content of initial data so constructed. Having examined binding energy to leading order, I have found that in the method of setting initial data via straightforward superposition of Kerr-Schild data, the background fields contain the Newtonian binding energy: the subsequent solution of the elliptic equations yields a only small correction. Using numerical solutions I have presented orbital configurations with solved initial data. I have presented a qualitative discussion of physical effects that may confound any attempt to study inspiral via a sequence of initial data, and which may affect the determination of the location of the ISCO.

However, the initial data approach to studying binary black holes is not without problems. First, there is no unambiguous way to set initial data in general relativity. Current algorithms all require some arbitrary mathematical choices to find a solution. For instance, the approach taken in this dissertation requires the definition of a background space and of its metric and the momentum of its metric, followed by solution of four coupled elliptic differential equations for variables that adjust the background fields. But the choice of the background quantities is arbitrary to a large extent. The physical meaning of these mathematical choices is not completely clear, but the physical effect is significant.

Data constructed with various algorithms can differ substantially, even

when attempting to describe the same physical system [62]. The data sets can be demonstrated in many circumstances to contain the expected Newtonian binding energy, as I have shown (i.e., the binding energy of order $O(m^2/\ell)$ agrees with the Newtonian result at this order). However, the data can differ significantly at $O(m(m/\ell)^2)$. These differences may be attributed to differences in wave content of the data reflecting possible prior motion, or the wave content may simply be a spurious addition. At present it is neither possible to build prior motion into the initial data, nor to specify how radiation is added to the the solution, nor to know how much there is. Therefore, it can be shown that the circular orbits and the ISCO so determined are in fact method-dependent. Furthermore, the methods need not even agree that a specific dataset represents a circular orbit; their subsequent evolutions may not agree [52].

Secondly, a chief physical difficulty with the initial data method for studying black hole binaries is the lack of unambiguous conserved quantities. For example, in the case of neutron stars, constant baryon number is an unambiguous indicator of the sameness of the stars. However, in black hole physics it is not available; it is unclear how to determine that two black hole initial data sets do, in fact, represent the same physical system. The best candidate for an invariant quantity is the event horizon area, $A_{\rm H}$. This area does not change for isentropic processes on account of the proportionality of $A_{\rm H}$ with the black hole entropy. One could argue that since the quasi-circular orbit is quasi-adiabatic, $A_{\rm H}$ is nearly invariant over some phase of the inspiral. But

the inspiral cannot be completely adiabatic because it cannot be made arbitrarily slow; the black holes will absorb an unknown amount of gravitational radiation while in orbit and will thereby increase in size.

Moreover, the event horizon is a global construct of the spacetime, and cannot be determined from a single slice of initial data. Therefore, one must use the apparent horizon area, $A_{\rm AH}$ as an ersatz invariant for initial data studies. When the hole is approximately stationary, these horizon areas may be nearly equal. In dynamic configurations—as should be appropriate for orbiting holes—these horizon areas may differ substantially [17].

One test of whether a sequence of initial value calculations can be used to mimic evolution calculations would be to compare evolution calculations with a sequence of initial value calculations directly. Unfortunately, the best extent evolution codes are incapable of evolving even a significant fraction of an entire Newtonian orbit. Therefore, even such matters as whether the irreducible mass is a useful invariant quantity between initial data sets, or whether the quasi-circular orbit is found by minimizing the effective potential (Eq. 2.60), cannot be computationally verified.

To an extent, the difficulty in setting data will become less relevant as good evolutions are eventually achieved. Data can be set for initial configurations with very large separation and then followed through until their merger. Matters of extraneous gravitational radiation built into the solution will become moot, since, in an evolution stable over many orbital periods, one merely has to wait for it to propagate off the computational grid, or fall into

the black hole before looking for gravitational wave signatures. Lacking any existing long-term stable evolution codes, the analysis presented here is a useful first step in understanding the physical content of initial data. However, it is only the beginning: a more full understanding of the physics of two interacting black holes is unlikely to come from the initial data alone, but from a full, time-dependent solution to the Einstein field equations.

Chapter 3

Imaging Radiating Matter Orbiting a Kerr Black Hole

3.1 Introduction

Gravitational wave signals are expected to be detected in second-generation detectors from a number of strongly gravitating systems of astrophysical interest which are currently being observed in other wavelengths. As a matter of forming a more complete understanding of those systems, it is of interest to investigate the signals of matter radiating in the conventional (and presently observable) electromagnetic spectrum from regions of highly curved spacetime. The most universal and widely studied astrophysical system from which we may one day detect gravitational radiation, and which is presently the subject of countless traditional observations, is that consisting of a disk of material orbiting and accreting onto a compact object, either a neutron star or a black hole. This type of system is ubiquitous in astronomical objects of stellar size, such as companion stars accreting onto neutron stars or stellar-mass black holes and in galactic-scale systems such as active galactic nuclei which are thought to contain an central accreting supermassive ($10^8 - 10^{10} M_\odot$) black hole.

To take one example, X-ray bursts are observed from matter falling onto pulsars. X-ray bursts can produce large scale asymmetries in the crusts of rotating neutron stars, causing them to deform. The resulting time-dependent mass quadrupole moments will generate gravitational radiation detectable by an instrument such as the Advanced LIGO detector. Observations of the X-ray emission from such a system in conjunction with gravitational wave observations could constrain models for the processes by which neutron stars are spun up to millisecond periods, and could give insight into the gravitational physics or equation of state of rapidly-spinning neutron stars.

As a matter of broad scientific interest in such systems, it is useful to be able to calculate the characteristics of radiation arriving from matter orbiting close to its last circular orbit of a black hole. I investigate here the general relativistic effects on radiation emitted from small clumps or particles of matter co-moving with the accretion disk around a compact object, in this case, specifically a black hole. The Kerr metric is assumed as being appropriate for the description of rotating astrophysical objects. In particular, I consider the photon propagation from circular orbits of matter in an idealized accretion disk to an observer at infinity. I follow here the assumptions of Page & Thorne [60] regarding the disk:

1. The disk is axially symmetric and lies in the equatorial plane of the black hole.

2. The disk is thin, and disk self-gravity can be neglected.

3. The matter in the disk moves nearly along circular geodesic orbits about the black hole, slowly losing energy and angular momentum, until it crosses the innermost marginally stable orbit and plunges into the hole.

4. Heat flow within the disk is negligible, and the only energy that is carried out of the surfaces of the disk is carried by photons. The gravitational radiation from the disk is neglected as well as extended magnetic fields.

5. Heating of the disk by photons emitted by other portions of the disk is neglected. This is assumption is not entirely physically realistic, and should be relaxed in more detailed models, but will be used for this discussion.

I consider the changes in observed flux including the increase when the emitting matter is behind the black hole on account of gravitational lensing (via an increase in the observed solid angle) and the Doppler effect at different portions of the orbit. This chapter details the calculations necessary for constructing the images of such orbiting material and producing the light curves showing the change in flux over an orbital period.

3.2 Particle Motion and Photon Propagation in the Kerr Metric

3.2.1 Equations of Motion

I first must consider the geodesic equations for both matter orbiting around a compact object and for photons propagating from the orbiting matter

to an observer located an infinite distance from the accreting object. The fundamental equations governing orbital dynamics in the Kerr metric were first derived by Carter [16] and later elaborated by Cunningham & Bardeen [19, 5] for the case of stable, bounded, circular particle orbits in the equatorial plane of a black hole. The Kerr metric in Boyer-Lindquist coordinates is given by:

$$ds^2 = -e^{2\nu}dt^2 + d^{2\psi}(d\phi - \omega dt)^2 + d^{2\lambda}dr^2 + e^{2\mu}d\theta^2 \tag{3.1}$$

where

$$\begin{aligned} e^{2\psi} &= sin^2\theta A\Sigma^{-1} && (3.2)\\ e^{2\nu} &= A^{-1}\Delta\Sigma && (3.3)\\ e^{2\lambda} &= \Delta^{-1}\Sigma && (3.4)\\ e^{2\mu} &= \Sigma && (3.5) \end{aligned}$$

and the auxiliary Kerr variables are given as

$$\begin{aligned} \Delta &= r^2 + a^2 - 2Mr && (3.6)\\ \Sigma &= r^2 + a^2\cos^2\theta && (3.7)\\ A &= (r^2 + a^2)^2 - a^2\sin^2\theta\Delta && (3.8)\\ \omega &= 2Mar/A && (3.9)\\ & && (3.10) \end{aligned}$$

The equations of motion for an electrically neutral test particle with mass μ are given by $\mathcal{D}^2x^i/\mathcal{D}\tau^2 = 0$ where $\mathcal{D}$ is the covariant derivative. In

the Hamiltonian formulation, momenta $p_\mu = g_{\mu\nu}\dot{x^\nu}$ are introduced from the Lagrangian

$$\mathcal{L} = \frac{1}{2} g_{\mu\nu} \dot{x^\mu} \dot{x^\nu} \tag{3.11}$$

to obtain the Hamiltonian

$$H = \frac{1}{2} g^{\mu\nu} p_\mu p_\nu \tag{3.12}$$

In Eq. (3.11) the dot denotes ordinary differentiation with respect to an affine parameter λ. Since the Hamiltonian does not depend explicitly on λ, it is automatically a constant of the motion, determined by the normalization $g_{\mu\nu}\dot{x^\mu}\dot{x^\nu} = -\mu_0^2$, as

$$H = -\frac{1}{2}\mu_0^2. \tag{3.13}$$

For a photon, μ_0 is set equal to 0; for time-like geodesics, μ_0 is set equal to 1.

The general orbits of particles may be characterized by four constants of the motion. Two of them arise from symmetries in p_t and p_ϕ and correspond to conservation of energy and angular momentum about the symmetry axis, namely $p_t = -E$ and $p_\phi = \Phi$, respectively. In addition, the constant of motion μ_0 which corresponds to conservation of mass is taken from Eq. (3.13). The fourth constant of the motion is not given by obvious symmetries of the metric. It can be found from the fact that the Hamilton-Jacobi equation,

$$\frac{\partial S}{\partial \lambda} = \frac{1}{2} g^{\mu\nu} \left[\left(\frac{\partial S}{\partial x^\mu} \right) \left(\frac{\partial S}{\partial x^\nu} \right) \right] \tag{3.14}$$

can be solved with a Jacobi action S given in terms of known constants of the motion:

$$S = -\frac{1}{2}\mu_0^2 \lambda - Et + \Phi\phi + S_\theta + S_r \tag{3.15}$$

and where S_θ and S_r are functions of θ and r only. Inserting this into Eq. (3.14) yields the separated form:

$$\left(\frac{dS_\theta}{d\theta}\right)^2 + a^2\mu_0^2 cos^2\theta + (aE\sin\theta - \Phi\sin^{-1}\theta)^2 = \tag{3.16}$$
$$-\Delta\left(\frac{dS_r}{dr}\right)^2 + 2\left[(r^2+a^2)E - a\Phi\right]\frac{dS_r}{dr} - \mu_0^2 r^2$$

which in turn gives two ordinary differential equations:

$$dS_\theta/d\theta = \sqrt{\Theta(\theta)} \tag{3.17}$$

$$dS_r/dr = \Delta^{-1}(P + \sqrt{R(r)}) \tag{3.18}$$

Where

$$\Theta(\theta) = \mathcal{Q} - \cos^2\theta\left[a^2(\mu^2 - E^2) + \Phi^2\sin^{-2}\theta\right], \tag{3.19}$$

$$P(r) = E(r^2+a^2) - \Phi a \tag{3.20}$$

$$R(r) = P^2 - \Delta(\mu^2 r^2 + \mathfrak{K}) \tag{3.21}$$

and $\mathfrak{K}$ is set equal to the left hand side of Eq. (3.16). The constant $\mathcal{Q}$ is related to the others by $\mathcal{Q} = \mathfrak{K} - (\Phi - aE)^2$, and will be relevant in the subsequent calculation.

From the full expression for the Jacobi action, the integrated forms of the geodesic and orbit equations are obtained:

$$\int^{\theta} \frac{d\theta}{\sqrt{\Theta}} = \int^{r} \frac{dr}{\sqrt{R}} \tag{3.22}$$

$$t = \int^{\theta} \frac{-a(aE\sin^2\theta - \Phi)d\theta}{\sqrt{\Theta}} + \int^{r} \frac{(r^2+a^2)}{\Delta}\left(1 - \frac{P}{\sqrt{R}}\right)dr \tag{3.23}$$

$$\phi = \int^{\theta} \frac{-a(aE - \Phi\sin^{-2}\theta)d\theta}{\sqrt{\Theta}} + \int^{r} \frac{a}{\Delta}\left(1 - \frac{P}{\sqrt{R}}\right)dr \tag{3.24}$$

3.2.2 Time-like Geodesics for Circular Orbits

In this model I will be considering matter orbiting in circular orbits in the equatorial plane of a spinning black hole. The parameters of such an orbit were first found by Cunningham & Bardeen [19], through the construction of an orthonormal tetrad in the local rest frame of a star, or in this case, any object small compared to the size of the disk, in a circular orbit around the central object.

The components of the tetrad representing the four-velocity of the star are:

$$\Lambda^{t}_{(t)} = e^{-\nu}(1 - V_*^2)^{-1/2} \tag{3.25}$$

$$\Lambda^{\phi}_{(t)} = \Omega_* \Lambda^{t}_{(t)} \tag{3.26}$$

and in the space-like direction:

$$\Lambda_{(\phi)\phi} = e^{\psi}(1 - V_*^2)^{-1/2} \tag{3.27}$$

$$\Lambda_{(\phi)t} = -\Omega_* \Lambda_{(\phi)\phi} \tag{3.28}$$

Here

$$\frac{d\phi}{dt} = \Omega_* = \pm\frac{1}{(a \pm \sqrt{\frac{r^3}{M}})} \tag{3.29}$$

is the angular velocity of the particle's orbit.The positive signs refer to a prograde orbit, which is the only kind I consider here. Retrograde orbits are unstable for $r < 9M$ and do not exist at all for $r < 4M$.

The velocity of the star in the locally non-rotating frame of reference is

$$V_* = (\Omega_* - \omega)e^{\psi-\nu} \tag{3.30}$$

The function $\omega = 2Mar/A$ represents the "frame dragging"; it is the velocity of a particle (or photon) with zero orbital angular momentum.

3.2.3 Photon Propagation

As mentioned earlier, there are four constants of the motion associated with a particle with four-momentum $(p_r, p_\theta, p_\phi, p_t)$: the energy of the particle $E = -p_t$, the angular momentum about the symmetry axis $\Phi = p_\phi$, Carter's constant $\mathcal{Q}$, related to the polar angular momentum by $p_\theta = [\mathcal{Q} + E^2 cos^2\theta - \Phi^2 cot^2\theta]^{1/2}$, and μ_0, associated with the rest mass and set equal to zero for null geodesics.

The trajectory of a photon is independent of its energy, and is described by the dimensionless parameters λ and q:

$$\lambda = \Phi/E \tag{3.31}$$

$$q = \mathcal{Q}^{1/2}/E \tag{3.32}$$

It should be noted that these parameters are related to the direction cosines of a beam of radiation with respect to the local rest frame of the emitting material. Letting φ and ϑ represent the angles of the beam with respect to the direction of the emitter's motion (φ) and with the direction perpendicular to the equatorial plane (- θ direction) (ϑ), then λ and q are given by:

$$\lambda = \frac{e^{\psi-\nu}(\cos\varphi + V_*)}{1 + e^{\psi-\nu}(\Omega_* \cos\varphi + \omega V_*)}, \tag{3.33}$$

$$q = r_* e^{-\nu}(1 - V_*)^{-1/2}(1 - \Omega_*\lambda) cos\vartheta \tag{3.34}$$

While this work does not deal directly with the angle of emitted radiation, this is a very useful quantity to know when dealing with the polarization of emitted radiation. Since the physical object under discussion is a disk of plasma accreting onto a black hole, a significant portion of the emitted radiation will have been Compton up-scattered before emission from the surface of the disk. Any model of polarization of the disk emission given as a function of emission angle may easily be incorporated here to calculate the total polarized flux from the disk, since the angle of emission of radiation is known automatically from (λ, q).

Substituting the parameters λ and q into Equations (3.22)-(3.24), the following equations for photon propagation are obtained:

$$\int_{\theta_*}^{\theta_0} \frac{d\theta}{\sqrt{\Theta(\theta)}} = \int_{r_*}^{r_0} \frac{dr}{\sqrt{R(r)}} \tag{3.35}$$

$$\Delta\phi = \int_{r_*}^{r_0} dr \frac{r[a + \lambda(r-1)}{\Delta\sqrt{R(r)}} + \lambda \int_{\theta_*}^{\theta_0} d\theta \frac{\cot^2\theta}{\sqrt{\Theta(\theta)}} \tag{3.36}$$

$$\Delta t = \int_{r_*}^{r_0} dr \frac{(r^2+a^2)^2 - a^2\Delta - a\lambda r}{\Delta\sqrt{R(r)}} + a^2 \int_{\theta_*}^{\theta_0} d\theta \frac{\cos^2\theta}{\sqrt{\Theta(\theta)}} \tag{3.37}$$

The functions $\Theta(\theta)$ and $R(r)$ for photons are:

$$\Theta(\theta) = q^2 + a^2\cos^2\theta - \lambda^2\cot^2\theta \tag{3.38}$$

$$R(r) = r^4 + (a^2 - q^2 - \lambda^2)r^2 + \left[(a-\lambda)^2 + q^2\right] r - a^2q^2 \tag{3.39}$$

These two quantities can also be related to the time derivatives:

$$\sqrt{\Theta} = \rho^2\dot{\theta} \tag{3.40}$$

$$\sqrt{R} = \rho^2\dot{r}, \text{ where} \tag{3.41}$$

$$\rho^2 = r^2 + a^2\cos^2\theta$$

Photon trajectories are evaluated directly from r_* to r_0 and from θ_* to θ_0. Some paths that reach the observer may have turning points (r_t, θ_t) in r, θ, or both. These turning points are found where the functions $\Theta(\theta)$ or $R(r)$ are equal to zero. These photon trajectories are then evaluated from $r_* \rightarrow r_t \rightarrow r_0$, and likewise in the θ direction.

3.3 Solving the Equations

I consider a small clump of matter or radiating particle orbiting a black hole (or neutron star) in a geometrically thin but optically thick disk. The clump will be assumed to be radiating isotropically, which is a reasonable assumption for the thermal line-emission characteristics of accretion disks. Effects of inclination on the observed light curve are significant. Disks at very low inclination (or nearly face-on orientation) will show both very little amplification from gravitational lensing, and light primarily red-shifted from the gravitational potential of the central object. Disks at high inclination (nearly edge-on) will have their light curves affected by two things: gravitational lensing as the emitting material passes behind the central object, and Doppler shifting of the emitted frequency as the material orbits away from and toward the observer. I investigate here the characteristic light curves from an emitting clump orbiting a spinning compact object.

The calculation assumes a geometrically thin Keplerian disk with inner radius r_*, and a clump rotating around a black hole of mass M. The usual spherical polar coordinate system (r, θ, ϕ) is used with the observer on the positive z-axis at $z = \infty$. The rotation axis z_* of the disk is inclined by an angle i to the $x - z$ plane. Azimuthal angles ϕ and ϕ_* are measured with respect to the x and x_* axes, respectively. The disk rotates in the direction of increasing ϕ_*, in the same sense as the spinning hole. Taking $\theta_* = \pi/2$, the relations between the star and observer coordinates are:

$$\sin\phi_* = \sin\theta\ \sin\phi \tag{3.42}$$

$$\cos\theta = \sin i\ \cos\phi_*. \tag{3.43}$$

The apparent position of the image seen by the observer is represented by two impact parameters α and β. They are measured relative to the direction to the center of the black hole: α in the direction perpendicular to the symmetry axis, and β parallel to it (see Fig. 3.1). Taking advantage of the azimuthal symmetry, I set the observer at $\phi = 0$.

The parameters α and β are related to the parameters λ and q by:

$$\alpha = -r_0\frac{p^{(\phi)}}{p^{(t)}} = -\frac{\lambda}{sin\theta_0} \tag{3.44}$$

$$\beta = \pm\frac{r_0 p^{(\theta)}}{p^{(t)}} = \pm\left[\Theta(\theta_0)\right]^{1/2} = \pm(q^2 + cos^2\theta_0 - \lambda^2 cot^2\theta_0)^{1/2} \tag{3.45}$$

Where the sign of β is positive if $(\partial\theta/\partial r)_0 > 0$, and negative if less than zero.

To obtain the image of a disk, equation Eq. (3.35) is integrated from r_* to ∞, and from $\theta_* = \pi/2$ to θ_0 as given by the inclination of the observer. There is an infinite number of pairs (λ, q) which satisfy Eq. (3.35). From the requirement that $\sqrt{\Theta}$ and $\sqrt{R}$ must be real, limits can be found for the numerical values of (λ, q). These can then be searched fairly efficiently to find those sets for which Eq. (3.35) is satisfied. Typically, around 200 - 400 sets of (λ, q) are found. They are then interpolated along the azimuthal angle to obtain smooth curves. There will also exist so-called *second-order* images -

images from photon trajectories that have circled the disk one or more times before reaching the observer. While easy to calculate, they are ignored here due to the fact that they contribute very little intensity to the total flux [4, 39].

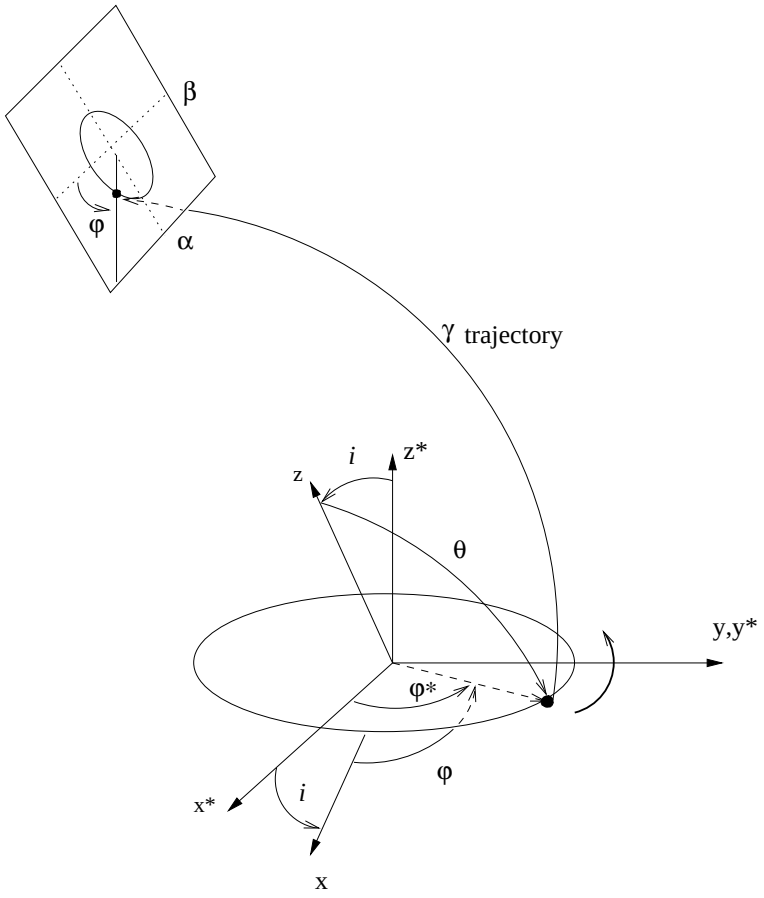

Figure 3.1: The geometry of the problem. Starred quantities represent the emitter's coordinates and un-starred quantities represent observer coordinates. A photon leaves the disk and reaches the observer at $z = \infty$. The photon is observed against the celestial sphere at a position given by impact parameters α and β as shown below.

3.4 Results

3.4.1 Disk Images

Figures 3.2 - 3.4 show images of disks of varying radii around an extreme Kerr hole and a Schwarzschild hole at varying inclinations.

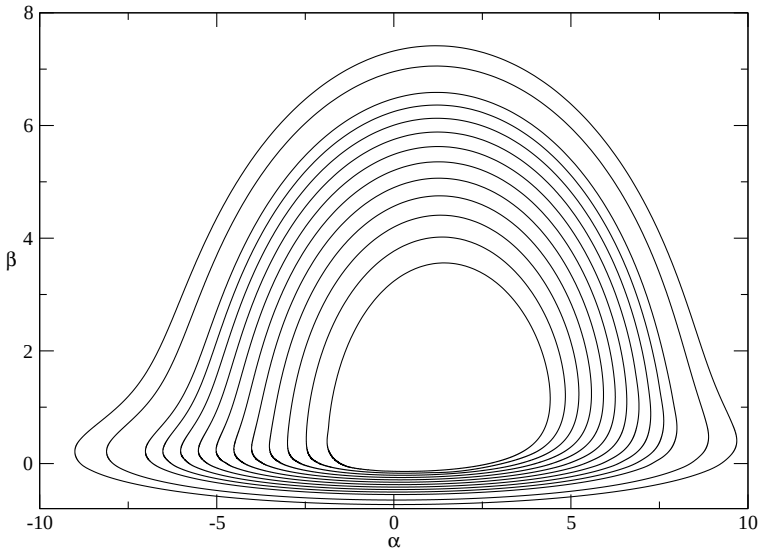

Figure 3.2: Ring images around an extreme ($a/M = 1$) Kerr hole. The innermost ring is at $1.02M$, the outermost is at $8M$. The disk is inclined to the observer at $i = 85°$

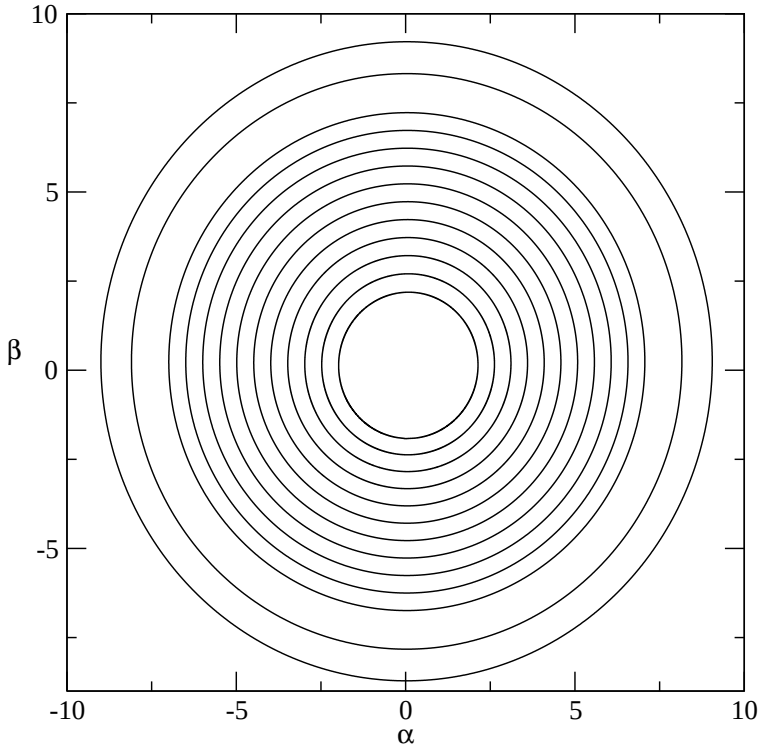

Figure 3.3: Ring images around an extreme ($a/M = 1$) Kerr hole. The innermost ring is at $1.02M$, the outermost is at $8M$. The disk is inclined to the observer at $i = 8°$

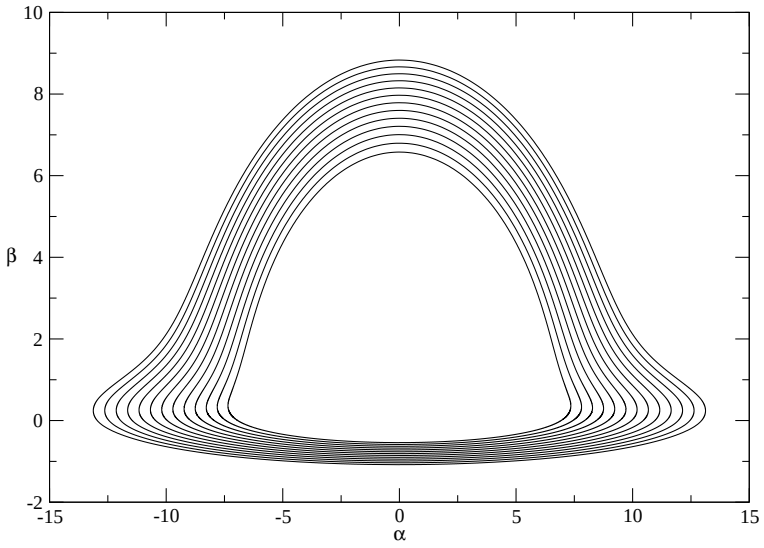

Figure 3.4: Ring images around a Schwarzschild hole. The innermost ring is at the innermost stable particle orbit at $6M$, the outermost is at $12M$. The disk is inclined to the observer at $i = 85°$

3.4.2 Energy shift

Following Cunningham & Bardeen [5], a photon with momentum four-vector p_μ has energy in the local rest frame of the star:

$$p^{(t)} = -\Lambda^{\mu}_{(t)} p_\mu \tag{3.46}$$

The ratio of the energy observed at infinity, E, and the energy in the emitting frame $p^{(t)}$ is given by:

$$E/p^{(t)} = e^{-\nu} \left[1 - \lambda\Omega_*\right] \left(1 - V_*^2\right)^{-1/2} \tag{3.47}$$

The first term in Eq. (3.47) corresponds to the energy shift due to gravitational redshift, the second to the classical Doppler shift, and the third to the special relativistic (transverse) Doppler shift.

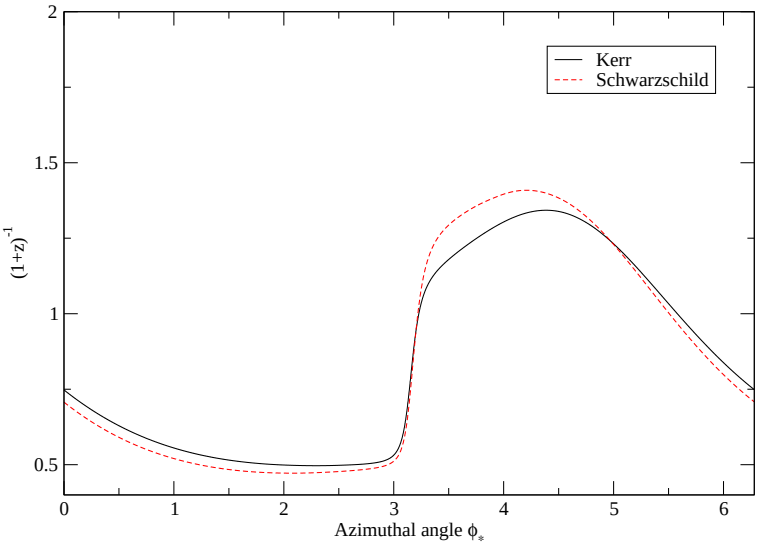

Figure 3.5: Example of redshift factors $(1+z)^{-1}$ calculated for an orbit at $r_* = 6M$ for Schwarzschild and extreme Kerr holes seen by an observer inclined to the plane of the orbit at $i = 85°$

3.4.3 Time Delay

I calculate the relative time delay for photons emitted from different locations in the orbit.. From equation Eq. (3.37) one can calculate the total time of photon propagation from a given point on an orbit. Since the observer here is considered to be an infinite distance from the emitting material, I calculate Δt relative to a reference photon emitted radially ($\lambda = q = 0$). The photon arrival time, which is a function of the (r_*, ϕ_*) position of the emitter, is given from the orbital time $t_{orb} = \phi_*/\Omega_*$ plus the relative time delay $\Delta t = t(\lambda, q) - t(0)$.

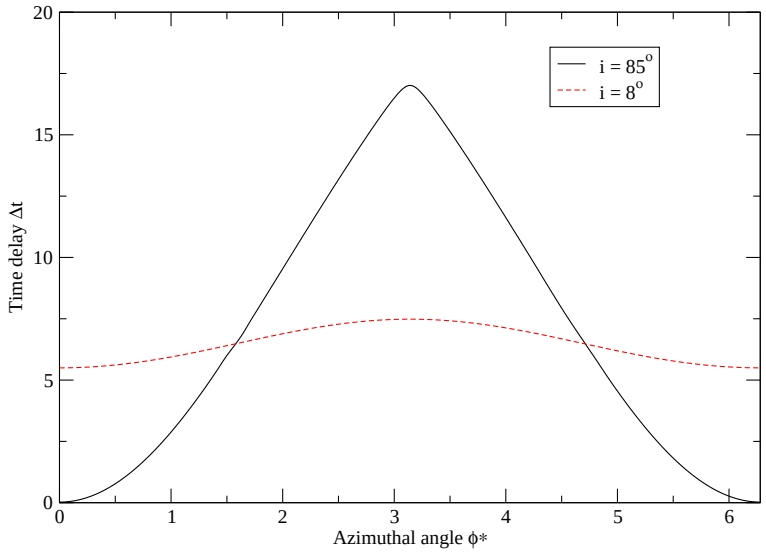

Figure 3.6: The time delay Δt for an orbit at $r_* = 6M$ around an extreme Kerr hole at two inclination angles,$i = 85°$ and $i = 8°$. Time delay is given in units of GM/c^3.

The time delay at each point along the orbit corresponds to a phase delay $\Delta\phi = \Omega_* \Delta t$. This has the effect of shifting the observed phase of a signal, as seen in Figure Fig. 3.7.

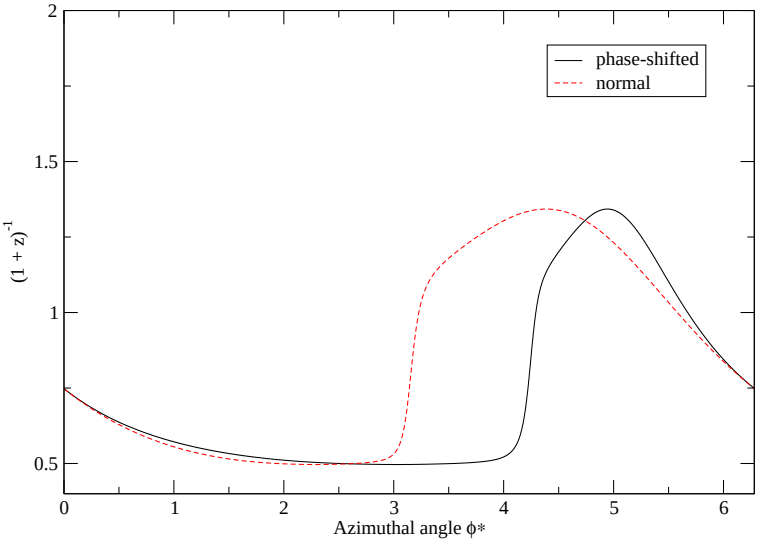

Figure 3.7: The energy shift $(1 + z)$ shown as a function of azimuthal angle, and with phase shift attributable to the relative time delay due to the lensed path behind the hole. Orbital parameters are the same as Fig. 3.6

The time delay for a disk around a stellar size compact object can reach nearly 10^{-1} milliseconds. For rapidly rotating objects, such as millisecond pulsars, Δt can be approximately 5 % of a typical 2.5 ms pulse rate, which can become significant in calculating the shape of an observed pulse. Fig. 3.8 shows the time delay in seconds around a stellar mass Kerr hole, for which the relative delay reaches fractions of a millisecond.

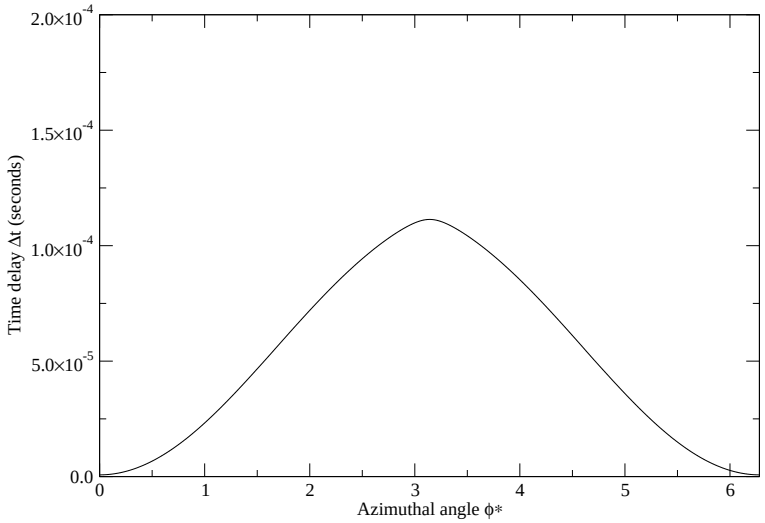

Figure 3.8: Time delay in seconds from a disk at $r_* = 20M$ around a stellar mass Kerr hole from an inclination $i = 80°$

3.4.4 Solid Angle

The observed solid angle $d\Omega$ must be calculated at each point in the disk in order to compute its contribution to the observed flux. For high inclinations, gravitational lensing will greatly increase the solid angle for the portions of the orbit going behind the black hole, causing a greater contribution to the observed flux from these regions than for the orbit in front of the hole, or from a nearly face-on orientation.

The solid angle as seen by the observer is given by the parameters α and β. In order to produce time-dependent flux profiles, the solid angle is expressed in terms of the coordinates of the emitting material ϕ_* and r_*, or

$$d\Omega = d\alpha \; d\beta = \left| \frac{\partial(\alpha, \beta)}{\partial(\phi_*, r_*)} \right| d\phi_* dr_* \tag{3.48}$$

The Jacobian is evaluated by finite differencing.

3.4.5 Light Curves

The specific intensity, I_ν, measured by a local inertial observer is obtained via the photon number density f which is a Lorentz invariant quantity and is constant along null geodesics in vacuum:

$$\frac{df}{d\tau} + f(x^\mu, p^\mu(\tau)) = 0 \qquad f = I_\nu/\nu^3. \tag{3.49}$$

The total observed line flux F is the integral of the specific intensity $I_{\nu_{obs}}$ over frequency and over the solid angle $d\Omega$ subtended in the observer's

sky by the luminous disk,

$$F = \int\int\int I_{\nu_{obs}} d_{\nu_{obs}} d\Omega. \tag{3.50}$$

The specific intensity of a line in the emitting frame is expressed by a δ-function at the rest frequency ν_0 of emission:

$$I_{\nu_{em}} = \varepsilon(\xi)\delta(\nu_{em} - \nu_0) \tag{3.51}$$

For convenience, here $\xi = r/M$ is the dimensionless radius, and $\varepsilon(\xi)$ is the surface emissivity which is assumed to vary with radius as a power law with index q,

$$\varepsilon(\xi) = \frac{\varepsilon_0}{4\pi}\xi^{-q} \tag{3.52}$$

The spectral index q can be used as a fitting parameter for fitting line profiles to disk emission, which can in turn constrain disk heating models [18]. Combining equations (5.17), (5.18), and remembering that $I_{\nu_{obs}}/\nu_{obs}^3 = I_{\nu_{em}}/\nu_{em}^3$ is a Lorentz invariant, the total observed flux in the line is

$$F = \int\int \varepsilon(\xi)(1+z)^{-4} d\Omega, \tag{3.53}$$

where $(1+z) = \nu_{em}/\nu_{obs}$ is the redshift factor.

In explicit form one can write the flux from line emission as:

$$F = \frac{\varepsilon_0}{4\pi} r_0^2 \int\int \xi^{-q}(1+z)^{-4} \left|\frac{\partial(\alpha,\beta)}{\partial(\phi_*, r_*)}\right| d\phi_* dr_* \tag{3.54}$$

Figures 3.9 - 3.11 show a set of the simulated light curves, solid angle and redshift factor $(1+z)^{-4}$ for different positions from the last stable orbit

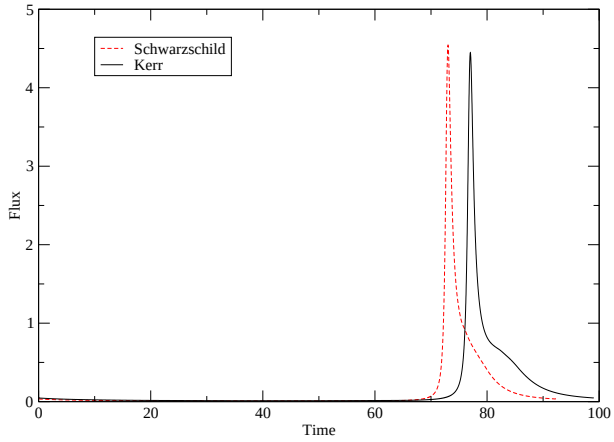

Figure 3.9: Flux from a radius of $r_* = 6M$ around a Schwarzschild and a Kerr hole as a function of photon arrival time. Disk inclination is $i = 85°$.

$r = 6M$ to $r = 80M$ around a Schwarzschild hole, and for different viewing angles of the observer from i $= 50° - 80°$. Fig. 3.12 shows the same data for the two cases of very large ($i = 5°$) and very small ($i = 5°$), respectively. Fig. 3.9 shows for comparison two light curves for a Schwarzschild and a Kerr ($a = 1$) hole from a radius of $r_* = 6M$.

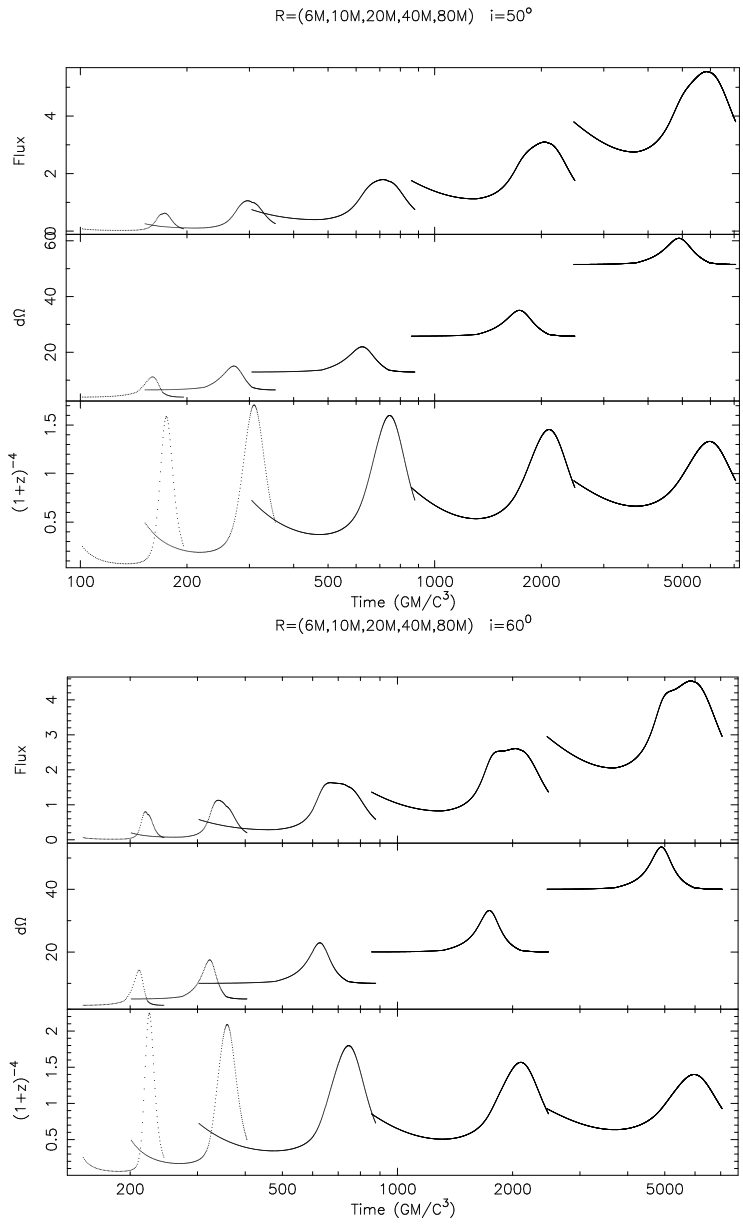

Figure 3.10: The observed flux, solid angle and redshift as a function of photon arrival time for a particle at $r = 6r_g, 10r_g, 20r_g, 40r_g, 80r_g$ and viewing angle of $i = 50°$ and $i = 60°$.

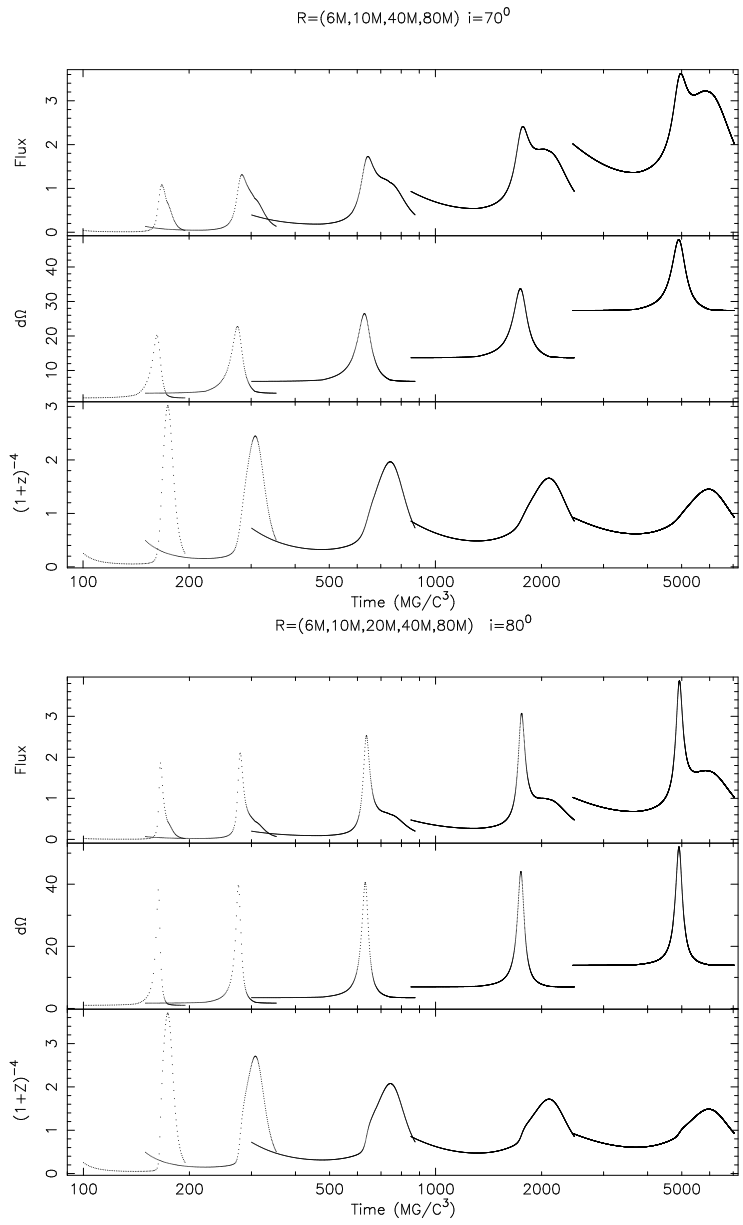

Figure 3.11: The observed flux, solid angle and redshift as a function of photon arrival time for a particle at $r = 6r_g, 10r_g, 20r_g, 40r_g, 80r_g$ and viewing angle of $i = 70°$ and $i = 80°$.

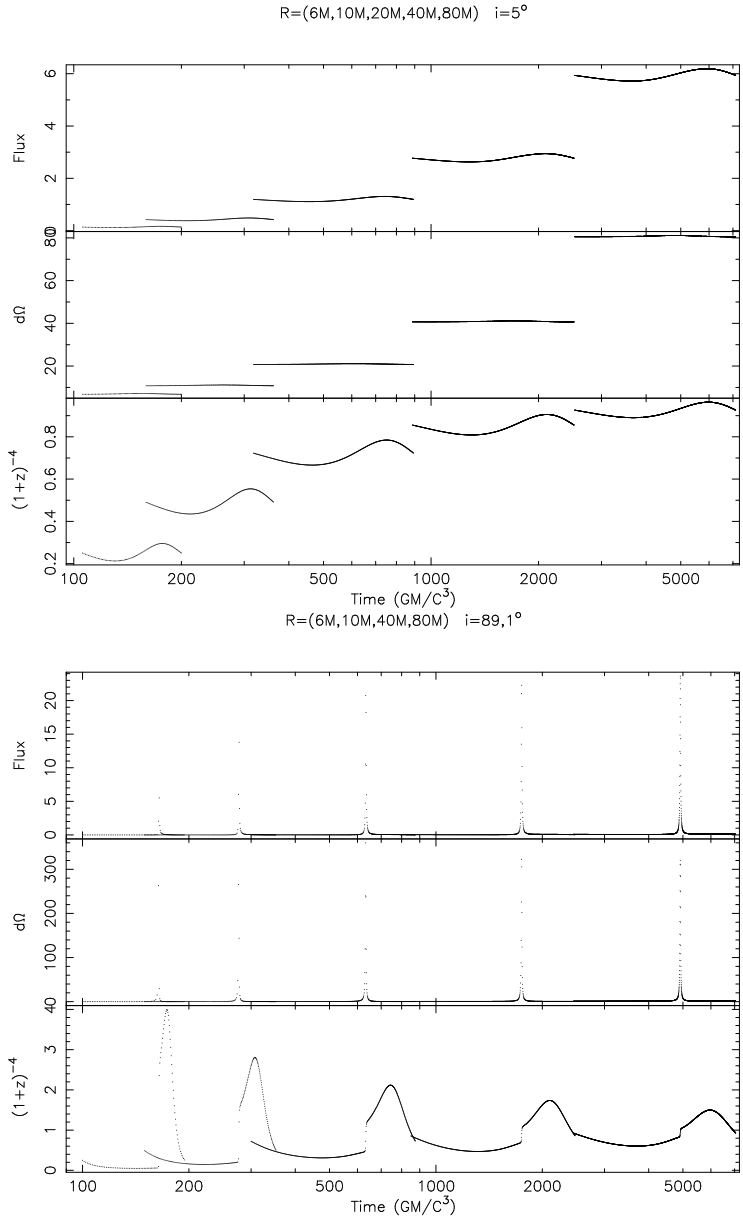

Figure 3.12: The observed flux, solid angle and redshift as a function of photon arrival time for a particle at $r = 6r_g, 10r_g, 20r_g, 40r_g, 80r_g$ and extreme viewing angles of $i = 5°$ and $i = 89.1°$.

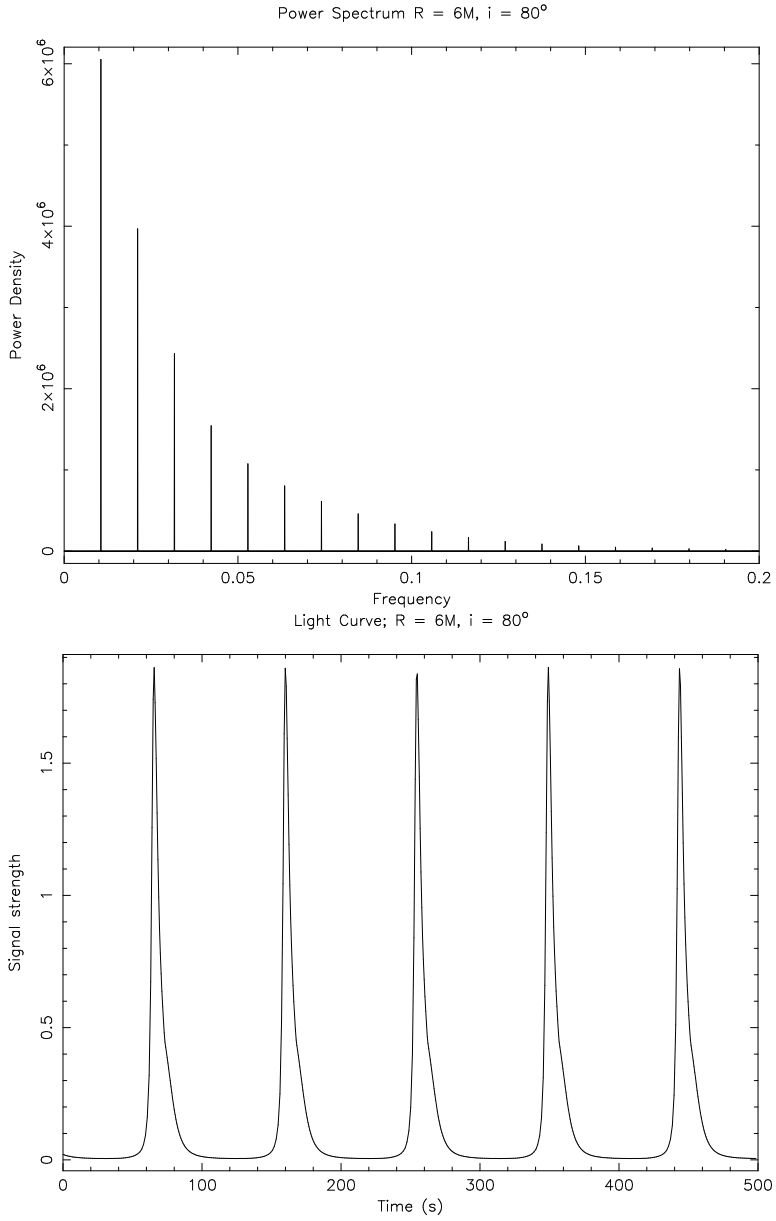

Figure 3.13: The light curve (the lower panel) and the power spectrum for an emitter at $R = 6M$ and viewing angle $i = 80°$. The first peak is the fundamental corresponding to the orbital frequency of the particle.

3.5 Thermal Emission

In addition to modeling monochromatic light from line emission, one can model other physically relevant emission profiles quite easily given the specific intensity of the radiation under consideration. One relevant example would be that of thermal (black-body) emission from a hot disk. Additionally, thermal photons can be Compton up-scattered in the disk giving rise to a power-law emission profile. The combined power-law/black-body profile is known to give good fits to observed data from both X-ray binaries (consisting of stellar-mass objects) and from AGN.

Following Page & Thorne [60] one can calculate an explicit expression for the radial dependence of the time-averaged energy flux from a disk of material. Assumptions made about the disk are as noted above in Section 3.1.

The innermost stable circular geodesic orbit is given by:

$$r_{min} = M\left\{3 + Z_2 \mp [(3 - Z_1)(3 + Z_1 + 2Z_2)]^{1/2}\right\}, \text{where} \quad (3.55)$$

$$Z_1 = 1 + (1 - \frac{a^2}{M^2})^{1/3}[(1 + \frac{a}{M})^{1/3} + (1 - \frac{a}{M})], \text{and} \quad (3.56)$$

$$Z_2 = (\frac{3a^2}{M^2} + Z_1^2)^{1/2} \quad (3.57)$$

and the temperature of the disk is given as $T(r) = [T_0 f(x)]^{1/4}$ where

$$
\begin{aligned}
T_0 &\equiv (3\dot{M}/8\pi M^2), && (3.58)\\
f(x) &= f_0(x)[x - x_0 + f_1(x) - f_2(x) - f_3(x) - f_4(x)], && (3.59)\\
f_0(x) &= \frac{1}{x^4(x^3 - 3x + 2a_*)}, && (3.60)\\
f_1(x) &= -\frac{3}{2}a_* \ln(\frac{x}{x_0}), && (3.61)\\
f_2(x) &= -\frac{3(x_1 - a_*)^2}{x_1(x_1 - x_2)(x_1 - x_3)} \ln(\frac{x - x_1}{x_0 - x_1}), && (3.62)\\
f_3(x) &= -\frac{3(x_2 - a_*)^2}{x_2(x_2 - x_3)(x_2 - x_1)} \ln(\frac{x - x_2}{x_0 - x_2}), && (3.63)\\
f_4(x) &= -\frac{3(x_3 - a_*)^2}{x_3(x_3 - x_1)(x_3 - x_2)} \ln(\frac{x - x_3}{x_0 - x_3}), && (3.64)\\
& && (3.65)
\end{aligned}
$$

Figure 3.14 shows the radial profile for an extreme Kerr hole from the innermost stable particle orbit to $r = 10M$. The accretion rate is assumed here to be $\dot{M} = 0.1$, and all physical constants are set equal to one. According to whether the system under investigation is galactic or stellar in scale, the physical temperature profile will vary considerably.

The specific intensity of black-body radiation is given by

$$I_\nu \propto \nu^3 (e^{h\nu/kT(r)} - 1)^{-1} \tag{3.66}$$

and the observed specific flux is given by

$$F_{\nu_{obs}} = \int \left(\frac{e^{h\nu_{obs}(1+z)/kT(r)} - 1}{e^{h\nu_{obs}/kT(r)} - 1} \right)^{-1} d\Omega \tag{3.67}$$

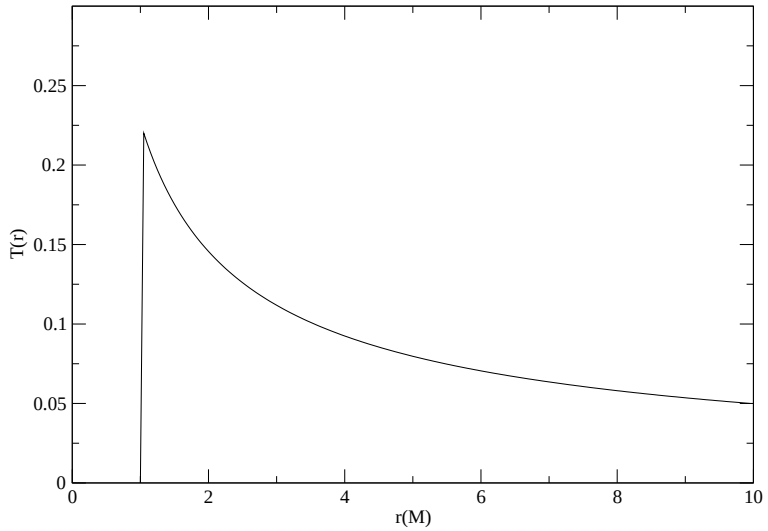

Figure 3.14: The temperature profile for an extreme (a/M = 1.0) Kerr hole with $\dot{M} = 0.1$

Figure 3.15 shows the emission profile of thermal emission from different parts of the orbit. Comparing to Fig 3.9 one can see that the emission is greatly increased in intensity on the approaching side of the disk on account of the greater blue shift, as well as the phase shift associated with the time delay.

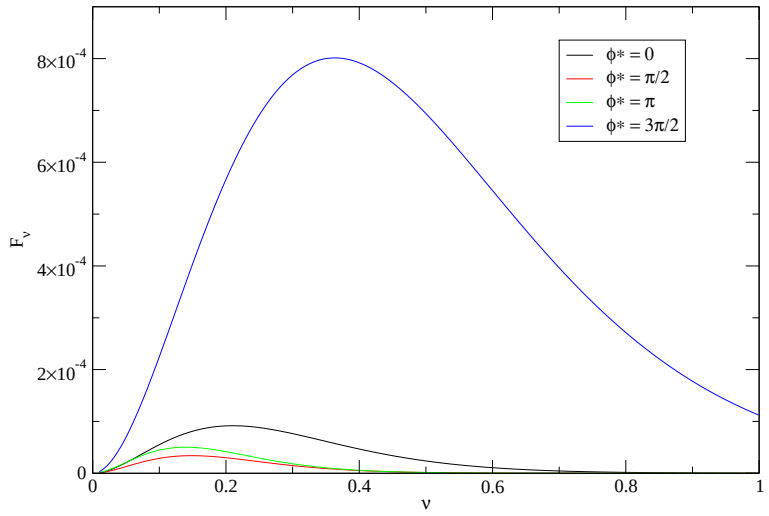

Figure 3.15: Black body emission profile at $r_* = 6M$ and $i = 85°$ for an extreme (a/M = 1.0) Kerr hole with $\dot{M} = 0.1$. The units used here are arbitrary.

3.6 Future Work

This model has the potential to be a useful tool for several different applications. One such is using it to measure emission-line profiles from accretion disks, especially in AGN. It is commonly held that the energy source of AGN is from matter accreting onto a super-massive central black hole in the nucleus of the galaxy. The disk-accretion model has been used to fit the broad-band continuum spectrum of AGN [68, 72], but the fit of disk models to emission lines is not so clear - observations tend to favor radial inflow or outflow of matter [44]. There are, however, some AGN which show double-peaked broad-line profiles. Chen et al. [18] have fit a line profile derived from a weak-field approximation to the AGN Arp 102B, where they find evidence for a disk with inclination $i = 33.5^\circ$ extending from $r = 250M$ to $r = 1000M$ with surface emissivity $q \simeq 3.1$. A fit which yields a measurement for surface emissivity can be used to constrain emission mechanisms for the disk. Observing time changes in the line profile of an AGN could also reveal the source of heating, the mechanism of line emission in the outer regions of the disk, or structural features of the disk. Other observations, such as the X-ray observation of Seyfert galaxy MCG-6-20-15 [74] have revealed emission lines attributed to K_α emission from cold Fe with profiles consistent with emission from several Schwarzschild radii from the center of the nucleus. Such observations very near to the horizon of the hole require fully relativistic models, and hold great promise for studying the strong gravitational fields of compact objects by, among other things, measuring directly the spins of black holes.

Aside from line profiles in AGN, it is possible to measure the polarization of high-energy radiation formed via Comptonization in X-ray binaries. Additionally, optical polarization in AGN has been found to be weaker and opposite in sign from that expected from smooth electron scattering atmosphere [70]. In some models [73], the angular distribution and polarization of the radiation depend only on the optical thickness of the disk. Work is currently in progress to model the polarization of Compton up-scattered photons in an optically thick disk. Such a calculation is easily merged with the current code to produce light-curves of polarized flux from an accreting object. More complicated models involving disk heating by returning radiation or other processes could also be incorporated into the existing code at a future date.

A third application for this work is investigating the relationship between accretion disk temperature and continuum colors in QSOs. A study by Cheng et al. [37] of the optical/UV continuum colors and the characteristic disk temperature QSOs has shown that whereas one might expect hotter disks to have bluer colors, the opposite in fact holds. The color dependence may have some of its source in relativistic effects. The code can be used to generate large numbers of integrated disk images in order to determine if the observed color is a result of these effects, or if it has some other cause.

Chapter 4

QSO Narrow [OIII] Line Width and Host Galaxy Luminosity

Established correlations between galaxy bulge luminosity L, black hole mass M_{BH}, and stellar velocity dispersion σ_* in galaxies suggest a close relationship between the growth of super-massive black holes and their host galaxies. Measurements of the $M_{BH} - \sigma_*$ relationship as a function of cosmic time may shed light on the origin of this relationship. Additionally, the tightness of the observed $M_{BH} - \sigma_*$ relationship in normal galaxies constrains the population of binary black holes currently within the nuclei of post-merger galaxies. Studies of the number and interaction rates of super-massive black holes in hierarchical models of galaxy formation demonstrate that if the merging timescale of super-massive binary black holes is longer than the Hubble time, a binary should be ejected in a significant fraction of elliptical galaxies [32]. The fact that the $M_{BH} - \sigma_*$ correlation is so strong requires that the black holes in the centers of merging galaxies merge within a shorter period of time, since nearly all bulges contain a central compact object. Furthermore, and there are not nearly as many off-center nuclei observed as would result from an existing binary interacting with a third object and being ejected from the center of the bulge. Such considerations constrain the population of galaxies

likely to contain binary black holes. This, in turn, illuminates the search for mechanisms of energy loss whereby the binary is likely to merge directly on account of dynamical friction or reach a separation where coalescence through emission of gravitational radiation is possible within a Hubble time. Therefore, it is desirable to explore the $M_{BH} - \sigma_*$ relationship in high-redshift objects in order to better understand the growth and dynamics of galaxies and their central black holes in addition to gaining information on the likely population of binaries in galactic nuclei.

One approach to measuring M_{BH} and σ_* is to derive black hole masses and stellar velocity dispersions from the widths of quasar (QSO) broad and narrow emission lines, respectively. I investigate the utility of using the velocity of the narrow line emitting gas, $\sigma_{[O\ III]}$, as a surrogate for σ_* in QSOs by examining host magnitudes and [O III] line widths for low redshift QSOs. For the limited range of $L_{\rm host}$ in this sample, the increase in $\sigma_{[O\ III]}$ with luminosity predicted by the Faber-Jackson relation is obscured by scatter. However, $\sigma_{[O\ III]}$ is consistent in the mean with host galaxy luminosity for radio quiet QSOs (RQQ). Radio-loud QSOs (RLQ) on average have $\log \sigma_{[O\ III]}$ smaller by 0.12 than radio quiet QSOs of similar $L_{\rm host}$. A similar offset between RLQ and RQQ is seen for M_{BH} versus $\sigma_{[O\ III]}$, but not in M_{BH} versus $L_{\rm host}$. This implies that $\sigma_{[O\ III]}$ and not M_{BH} is responsible for the RL-RQ offset for radio-loud QSOs in the $M_{BH} - \sigma_{[O\ III]}$ relationship.

4.1 Introduction

The relationship between a galaxy's central black hole and the evolutionary history of its host galaxy is unclear. Probing the correlations between galaxy luminosity, stellar velocity, gas velocity, and black hole size may reveal the connection between a galaxy's central black hole and its formation history.

Host galaxy magnitudes correspond to the mass of the central black hole. Magorrian et al. [40] showed that central black hole mass is proportional to the luminosity of the bulge of the host galaxy. Laor [38] showed that quasar host galaxy luminosity is similarly correlated with the black hole mass deduced from the broad Hβ lines. The stellar velocity dispersion in the galactic bulge also correlates with the mass of the central black hole. Gebhardt et al. [27] and Ferrarese & Merritt [23] found that the correlation between these two parameters is quite strong, suggesting the link between the formation of the bulge and the development of the black hole. Theoretical interpretations of this correlation (e.g. Silk & Rees [71], Adams, Graff, & Richstone [1], Burkert & Silk [14], Ostriker [59], Balberg & Shapiro [3], Haehnelt & Kauffmann [31]) differ as to whether the black hole forms before, during, or after the bulge. Measurements of the $M_{BH} - \sigma_*$ relationship at high redshift, may help to resolve this question [69].

Measurements of σ_* are difficult for distant QSOs, given the faintness of the galaxy and the relative brightness of the nucleus. However, it is possible to infer M_{BH} and σ_* from the widths of broad and narrow line emitting gas [46, 10, 69, and references therein]. Derivation of M_{BH} from the broad line

widths and continuum luminosity is now well established. However, estimating velocity dispersions from the velocities of the narrow line widths is more controversial (see below); and therefore any new test of $\sigma_{[O\ III]}$ as a surrogate for σ_* is valuable.

In normal galaxies, σ_* is related to bulge luminosity by the Faber-Jackson relation [24]. This relation is particularly true for early-type galaxies, which comprise the majority of the hosts of luminous quasars with $M_R < -24$ [22, 67]. In this chapter, I test the use of [O III] line widths as a surrogate for σ_* by studying the $M_{HOST} - \sigma_{[O\ III]}$ relationship in a sample of quasars for which the host galaxy luminosity has been measured. In Section 4.2 I discuss [O III] lines in AGN. In Section 4.3 I describe the host galaxy luminosities used here and measurements of the [O III] line widths. In Section 4.4 I discuss the results. I assume a cosmology with $H_0 = 70$ km s^{-1} Mpc$^{-1}, \Omega_{\rm M} = 0.3, \Omega_\Lambda = 0.7$. All values of luminosity used are corrected to these cosmological parameters.

4.2 [O III] Lines in AGN

Nelson & Whittle [58] made a comparison of [O III] $\lambda\lambda 5007, 4959$ line widths and stellar velocity dispersions in Seyfert galaxies, taking $\sigma_{[O\ III]} \equiv FWHM[O\ III]/2.35$ as appropriate for a Gaussian line profile. They found on average good agreement, although $\sigma_{[O\ III]}$ shows more scatter than σ_* . This supports the idea that the Narrow Line Region (NLR) gas is largely in orbital motion in the gravitational potential of the bulge and can be effectively used as a substitute where stellar velocities cannot be measured. Further

supporting the use of FWHM[O III] in place of stellar velocities is the work of Nelson [56], who shows that the $M_{BH} - \sigma_*$ relation for normal galaxies and AGN [27, 28] is preserved when $\sigma_{[O\ III]}$ is used in place of σ_*.

Contributing to the scatter shown by [O III] emission in comparison to σ_* is the fact that [O III] line profiles often have substantial asymmetry and a non-Gaussian profile. This may arise from outflow combined with extinction of the far side of the NLR (e.g., Wilson & Heckman [81]; Nelson & Whittle [57]). Radio-loud AGN tend to have stronger [O III] emission than radio quiet objects, as reflected in "Eigenvector 1" of Boroson & Green [11]. Radio jets may contribute to the motions of the NLR gas; Nelson & Whittle [57] find wider [O III] in AGN with powerful linear radio sources. Objects with strong iron emission can obscure the [O III] emission due to the Fe II features lying close to the [O III]$\lambda\lambda 4959, 5007$ line.

4.3 Data

4.3.1 Host Galaxy Magnitudes

Host galaxy magnitudes were taken from the literature, including McLure & Dunlop [47], Hamilton, Casertano, & Turnshek [33], Percival et al. [61], Floyd et al. [20], and McLure, Percival, & Dunlop [50]. The host galaxy measurements of McLure & Dunlop, Percival et al., Floyd et al, and McLure, Percival, & Dunlop were performed using the same method for fitting and subtracting the nucleus, modeling the host galaxy, integrating the host galaxy light, and performing the K-corrections [described in 49]. The measurements

done by Hamilton et al. [33] differed in these respects. As a result, when comparing the set of objects for which both studies report a host galaxy magnitude, there is an average offset. I converted the V-band magnitudes of Hamilton et al. to the Cousins R-band in which McLure & Dunlop report their results by using colors $V - R_c = 0.61$ for elliptical galaxies and $V - R_c = 0.54$ for spiral galaxies [25], taking the morphologies as given by Hamilton et al. The resulting magnitudes from Hamilton et al. are, on average, brighter by about 0.25 mag. All magnitudes measured by Hamilton et al. were adjusted by this amount in order to correct for average measurement difference between the two methodologies.

4.3.2 [O III] Line Widths

The [O III] line widths in this paper were measured directly from spectra publicly available from Marziani et al. [43] and the spectra presented by Mclure & Dunlop in [46]. The latter present spectra with resolution ~ 240 km s^{-1} for 13 of their 30 QSOs. The Marziani et al.spectra have instrumental dispersions ranging from 3 - 7 Å. Iron emission was subtracted from the spectra using the Boroson & Green [11] Fe II template. I made a direct measurement of the FWHM using the IRAF routine SPLOT, in preference to using a fit to the line profile [1]. Line widths were corrected by subtracting the instrumental FWHM in quadrature. Objects for which Fe II emission obscured

[1]IRAF is distributed by the National Optical Astronomy Observatories, which are operated by the Association of Universities for Research in Astronomy, Inc., under cooperative agreement with the National Science Foundation.

the [O III] line were discarded. For the McLure & Dunlop sample, this led to the exclusion of one out of 13 RLQ and 2 out of 17 RQQ. Of the 7 objects from McLure, Percival & Dunlop, all RLQ, one was rejected. One RQ object from Floyd et al. was rejected. Of the objects from Hamilton et al. for which a spectrum was available, four duplicated objects already in the foregoing sources, and one (RL) was rejected, leaving 3 RLQ and 7 RQQ. Typical errors in FWHM([O III]) are about 10%, coming largely from uncertainy in continuum placement.

4.3.3 Black Hole Masses

Below I compare host galaxy magnitudes and [O III] widths with black hole masses for the measured objects. Black hole masses were derived from the FWHM of the broad component of the Hβ emission line and the continuum luminosity at 5100 Å, using equation A7 of McLure & Dunlop (See [48] and references therein for details and background.) For the McLure & Dunlop objects, the Hβ width and continuum luminosity were taken from [48]. For the other objects, the Hβ width and the continuum luminosity at λ5007 were taken from Marziani et al. and scaled it to λ5100 using a typical continuum slope $F_\lambda \propto \lambda^{-1.5}$. Two objects (0204+292 and 2247+140) were rejected because of weak or asymmetrical Hβ , a strong narrow component of Hβ , and noise; and 0100+020 was omitted because Marziani et al. do not give an absolute flux. The black hole masses here are typically several tenths dex smaller than those tabulated by McLure & Dunlop because of differences in the adopted

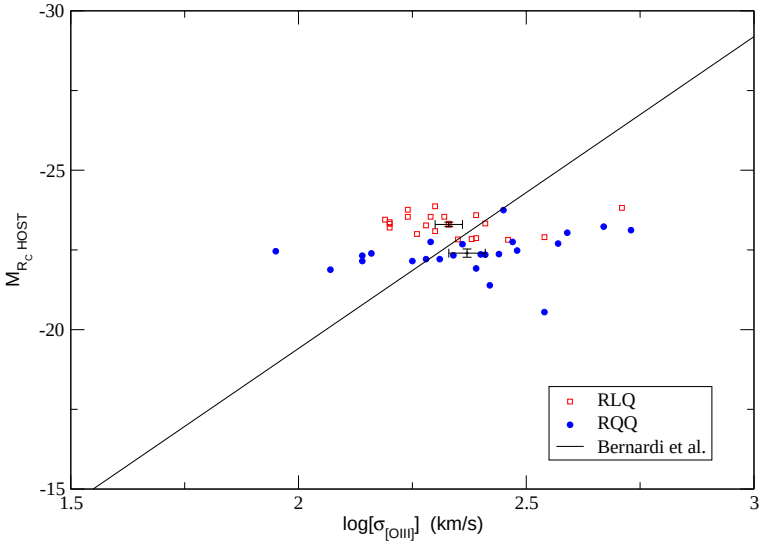

Figure 4.1: The above plot shows the sample of quasars for which host galaxy magnitudes and reliable [O III] FWHM were obtained. The objects were classified as radio-loud or quiet according to the papers from which the host magnitudes were taken. The straight line is the Faber-Jackson relation measured by Bernardi et al. [6, 7]; it is not a fit to the data. The crosses indicate the mean values and errors of the mean for host luminosity and $\sigma_{[O\ III]}$ for RL and RQ objects.

cosmology and mass formula.

4.4 Results

4.4.1 The $M_{HOST} - \sigma_{[O\ III]}$ relationship

The results for $M_{HOST} - \sigma_{[O\ III]}$ are plotted in Fig. 1. As can be seen, the data for the QSOs given agree in the mean with the Faber-Jackson relation, using $\sigma_{[O\ III]}$ in lieu of σ_*. However, the scatter is large, about 0.16 in $\log \sigma_{[O\ III]}$ for the full sample or 0.11 dex for the radio-quiet objects excluding

Table 4.1: Below are the objects for which it was possible to obtain both host magnitudes and reliable [O III] line widths. Host galaxies are given in the Cousins R-Band and adjusted for the adopted cosmology, and $\sigma_{[O\ III]} = FWHM[O\ III]/2.35$. Magnitude sources: (1) McLure & Dunlop [47, and references therein]; (2) Hamilton et al. [33]; (3) Floyd et al. [20]; (4) Percival et al. [61] (5) McLure, Percival, & Dunlop [50]. [O III] sources: (a) McLure & Dunlop [46]; (b) Marziani et al. [43].

Name	redshift	M_{R_c}(host)	$\log(\sigma_{[O\ III]})$	M_{R_c} source	[O III] source
Radio-Quiet Quasars					
0052+251	0.154	-22.44	2.44	(1)	(a)
0054+144	0.171	-23.11	2.59	(1)	(a)
0157+001	0.164	-23.76	2.45	(1)	(a)
0204+292	0.109	-22.81	2.36	(1)	(a)
0205+024	0.155	-20.83	2.54	(1)	(b)
0244+194	0.176	-22.45	2.31	(1)	(a)
0923+201	0.190	-22.76	2.57	(1)	(a)
0953+414	0.239	-22.32	2.41	(1)	(a)
1012+008	0.185	-23.26	2.67	(1)	(b)
1029-140	0.086	-22.15	2.40	(1)	(b)
1116+215	0.177	-23.17	2.73	(1)	(b)
1202+281	0.165	-22.21	2.28	(1)	(b)
1307+085	0.155	-21.97	2.34	(1)	(b)
1309+355	0.184	-22.94	2.48	(1)	(b)
1635+119	0.146	-22.55	1.95	(1)	(b)
1821+643	0.297	-24.47	2.43	(3)	(b)
0137-010	0.335	-21.66	2.25	(4)	(b)
0100+020	0.393	-22.32	2.14	(2)	(b)
0316-346	0.260	-22.75	2.47	(2)	(b)
1059+730	0.089	-21.92	2.39	(2)	(b)
1216+069	0.331	-22.39	2.16	(2)	(b)
1219+755	0.071	-22.15	2.14	(2)	(b)
1229+204	0.064	-21.88	2.07	(2)	(b)
1416-129	0.129	-21.39	2.42	(2)	(b)
1426+013	0.086	-22.75	2.29	(2)	(b)

Name	Redshift	M_{R_c}(host)	$\log(\sigma_{[O\ III]})$	M_{R_c} source	[O III] source
Radio-Loud Quasars					
0137+012	0.258	-23.55	2.29	(1)	(a)
1004+130	0.240	-23.63	2.39	(1)	(a)
1020-103	0.197	-22.87	2.46	(1)	(a)
1217+023	0.240	-23.19	2.20	(1)	(b)
1226+023	0.158	-23.79	2.71	(1)	(b)
1302-102	0.286	-23.48	2.39	(1)	(b)
1545+210	0.266	-23.12	2.33	(1)	(b)
2135-147	0.200	-22.90	2.35	(1)	(b)
2141+175	0.213	-23.13	2.54	(1)	(b)
2247+140	0.237	-23.36	2.33	(1)	(a)
2349-014	0.173	-23.77	2.24	(1)	(b)
2355-082	0.210	-23.12	2.30	(1)	(a)
1150+497	0.334	-23.45	2.19	(3)	(b)
0133+207	0.425	-23.27	2.28	(2)	(b)
0202-765	0.389	-23.00	2.26	(2)	(b)
0837-120	0.198	-22.84	2.38	(2)	(b)
1216+069	0.334	-23.33	2.16	(5)	(b)
1425+267	0.366	-23.19	2.20	(5)	(b)
1512+370	0.371	-23.69	2.30	(5)	(b)
1704+608	0.371	-23.36	2.24	(5)	(b)
2251+113	0.323	-22.70	2.41	(5)	(b)
2308+098	0.432	-22.92	2.32	(5)	(b)

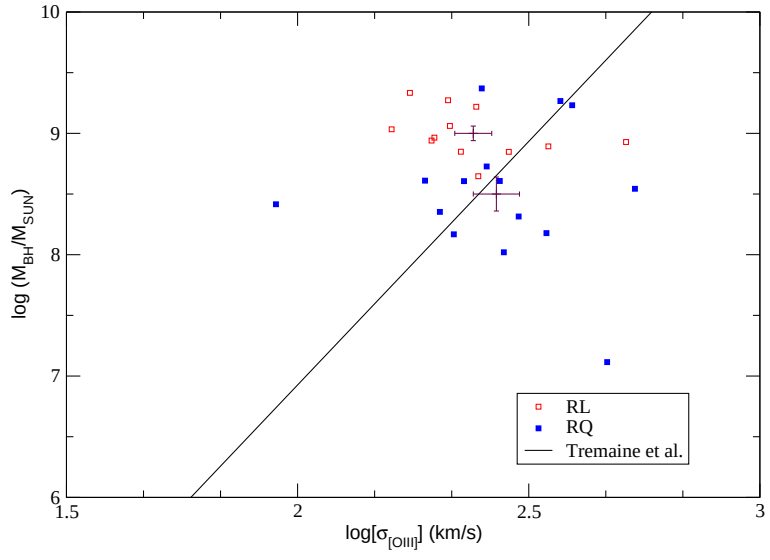

Figure 4.2: M_{BH} versus $\sigma_{[O\ III]}$ for objects in Table 1 with exceptions described in the text, and expressed in log $M_{\odot}$. The $\sigma_{[O\ III]}$ values are taken from Table 1. The RL objects are offset from the Tremaine et al. [78] relation similarly to the RL-RQ offset in Figure 1.

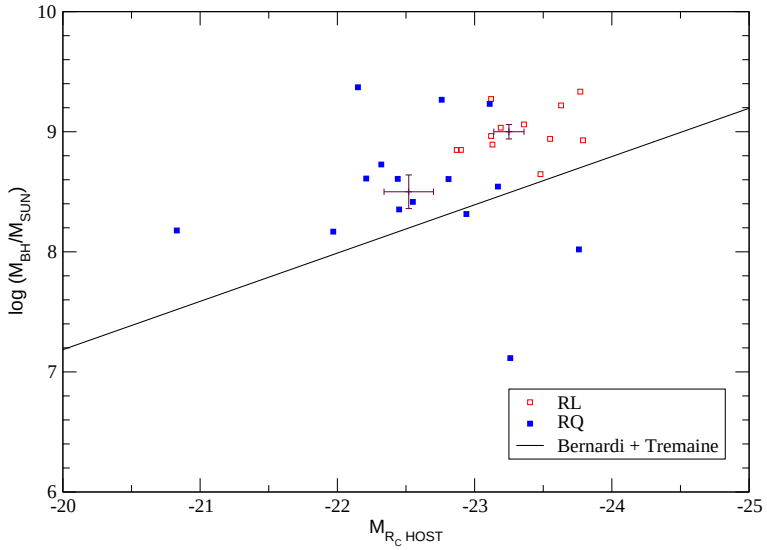

Figure 4.3: M_{BH} versus M_{HOST} for the same objects as Figure 2, along with the relation described in the text. This figure is similar to Fig. 2 of McLure & Dunlop [46], where it can be seen that the RL objects are not offset from the RQ objects in relation to the normal M_{BH} - M_{HOST} trend.

the extreme outlier (1635+119) at low $\sigma_{[O\ III]}$. Given the limited range of luminosities available to us this scatter obscures any increase of $\sigma_{[O\ III]}$ with M_{HOST} as expected by the Faber-Jackson relation.

Scatter inherent in the Faber-Jackson relation for normal galaxies contributes very little to the scatter seen in Figure 1. Bernardi, et al. [6, 7], in a sample of 9000 early-type galaxies, find the rms scatter in σ_* in the R-band to be around .075 dex in log σ at constant luminosity [see Fig. 4 in 7]. Another source of uncertainty comes from the inability to measure FWHM [O III] with high accuracy. Plausible displacements in location of the continuum level can lead to a ΔFWHM([O III]) of about $\pm$50 km/s, or a scatter of $\sim$ 0.04 dex in log $\sigma_{[O\ III]}$. Scatter of 0.5 mag. in M_{HOST} corresponds to 0.05 in log $\sigma_{[O\ III]}$ Ṫaken together with the standard deviation in log $\sigma_{[O\ III]}$ of $\sim$ 0.16, one is left with an intrinsic scatter in [O III] of

$$(\log \sigma_{[O\ III]})^2 \sim (0.16)^2_{OBS} - (0.075)^2_{FJ} - (0.04)^2_{FWHM} - (0.05)^2_{M_{HOST}} = (0.13)^2 \tag{4.1}$$

Clearly, the geometry and kinematics of the Narrow Line Region cause the $\sigma_{[O\ III]}$ to differ substantially from σ_* in individual objects. However, some mix of processes evidently increases or decreases $\sigma_{[O\ III]}$ with respect to σ_* with roughly equal probability, so that $\sigma_{[O\ III]}$ and σ_* agree fairly well in the mean.

Nelson & Whittle [58] found that AGN with powerful, linear radio

sources sometimes have $FWHM([O\ III])$ larger than expected for the value of σ_* . However, Figure 1 shows that the radio-loud objects in the sample have, on average narrower FWHM [O III] for a given host luminosity. I find average values of $\sigma_{[O\ III]}$, M_{HOST} $(2.33 \pm 0.03, -23.22 \pm 0.07)$ for radio-loud objects, and $(2.37 \pm 0.04, -22.38 \pm 0.13)$ in radio-quiet objects. The errors cited are the standard deviations of the mean (1 σ).

In this sample, the RL hosts are 0.84 magnitudes brighter, on average, than the RQ hosts. Therefore, they should have log $\sigma_{[O\ III]}$ 0.08 larger. In fact, they are found to have log $\sigma_{[O\ III]}$ 0.04 smaller, giving a total discrepancy of 0.12 ± 0.05 in log $\sigma_{[O\ III]}$ with respect to the Faber-Jackson relation. Shields et al. [69] and Bian & Zhao [8] found radio-loud objects to have, on average, narrower FWHM [O III] than radio-quiet objects for a given black hole mass. Bian & Zhao, looking at the $M_{BH} - \sigma$ derived from the FWHM [O III] measurements in Marziani et al. and Shields et al., find M_{BH} to be overestimated from $FWHM([O\ III])$ in radio-loud objects. Table 3 of Bian & Zhao gives Δ log M = 0.51, -0.36 for RL, RQ objects in Marziani et al., respectively, and 0.59, 0.17 for Shields et al. This gives an average Δ log M(RL-RQ) of 0.65. Using $M_{BH} \propto \sigma^4$ [78], this may be restated as Δ log $\sigma_{[O\ III]}$ (RL-RQ) = 0.16. This is close to the measured offset here of RL from RQ objects in log $\sigma_{[O\ III]}$ of 0.12.

Bian & Zhao consider whether the RL-RQ offset seen in the M_{BH} - $\sigma_{[O\ III]}$ relation might be due to the measurements of M_{BH} or $\sigma_{[O\ III]}$. Geometrical effects in RLQ might affect the observed width of the broad Hβ line

or the optical continuum luminosity, either of which would affect the derived M_{BH} . Alternatively, the RL-RQ offset could be due to narrower [O III] lines in RL objects. Figure 2 shows an M_{BH} -$\sigma_{[O\ III]}$ plot for these objects, where M_{BH} is derived as described above. The RL-RQ offset is similar to that in the M_{HOST} -log $\sigma_{[O\ III]}$ plot. Figure 3 shows an M_{BH} -M_{HOST} plot along with the relationship predicted by combining the Faber-Jackson relationship in Figure 4 of [7] with the M_{BH} -σ_* relationship of Tremaine et al. (2002). The Faber-Jackson relation was adjusted from r^* to R_C magnitudes using the values of Fukugita et al. [25]. This relation is particularly true for early-type galaxies, which the majority of hosts of luminous QSOs comprise. Figure 3 shows no significant RL-RQ offset relative to the expected slope. These results indicate that narrower $\sigma_{[O\ III]}$ for RL objects is responsible for the RL-RQ offset in the M_{BH} -$\sigma_{[O\ III]}$ relationship, and not any systematic effect involving M_{BH} . The cause of this offset is unknown.

Chapter 5

Conclusions

I have here presented a discussion of three problems related to black hole spacetimes, through both computational calculation and in analysis of observed data. I have solved the initial value problem for a binary black hole in writing a code which solves the constraint equations of general relativity for such a spacetime. I have discussed the physical content of that initial data, both for the analytic superposed Kerr-Schild data and for the solved fields. While the results given represent a powerful way to set initial data for a wide variety of initial configurations of the orbiting black holes, it remains difficult to physically interpret the initial data alone. The numerical solution of Einstein's equations is a necessary and potentially powerful tool to model strongly gravitating systems, especially in the case of gravitational radiation emitted from a binary black hole, but the computational capabilities remain limited at this time, and a full analysis of the physical content of initial data sets must wait for further development.

I have also presented a calculation of the light curve from isotropically radiating matter in an idealized accretion disk around a spinning black hole. I have numerically solved the geodesic equations for a photon propagating from

the surface of a disk to an observer. I calculate various general relativistic effects upon the signal received by the observer including the energy shift, relativistic time delay and phase shift, and gravitational lensing. This is used to model light curves for different flux emission profiles at varying disk inclinations and radii, for spinning and non-spinning black holes, and for varying disk parameters such as surface emissivity and temperature. In the future, the ray-tracing code can be integrated with more physically realistic accretion disk models to provide useful analysis of black hole and neutron star binaries.

Finally, I have discussed work relating to observations of AGN. In particular, I have investigated the relationship between host galaxy bulge luminosity, stellar velocity dispersion, and central black hole masses of AGN. I have found that the use of the velocity of narrow line emitting gas as a surrogate for stellar velocity dispersion is accurate in aggregate, but does not provide a reliable indicator for stellar velocity for individual objects which may be too far away, or contain a nucleus whose high luminosity makes measurements of stellar velocities impractical. I have noted an unexplained correlation between narrow line width and the radio luminosity of a QSO; the physical cause thereof should prove interesting in understanding QSO dynamical processes. I have shown how host galaxy studies may shed light on the properties of central supermassive black holes, are useful for understanding the evolution and dynamics of AGN per se, and also provide a constraint on binary black hole event rates.

Bibliography

[1] F. C. Adams, D. S. Graff, and D. O. Richstone. A Theoretical Model for the M_{BH}-σ Relation for Supermassive Black Holes in Galaxies. *Astrophysical Journal Letters*, 551:L31–L35, April 2001.

[2] R. Arnowitt, S. Deser, and C. Misner. Gravitation, an introduction to current research. New York, 1962. Wiley.

[3] S. Balberg and S. L. Shapiro. Gravothermal Collapse of Self-Interacting Dark Matter Halos and the Origin of Massive Black Holes. *Physical Review Letters*, 88(10):101301–+, March 2002.

[4] G. Bao, P. Hadrava, and E. Ostgaard. Emission-line profiles from a relativistic accretion disk and the role of its multiple images. *Astrophysical Journal*, 435:55–65, November 1994.

[5] C. T. Bardeen and J. M. Cunningham. The Optical Appearance of a Star Orbiting an Extreme Kerr Black Hole. *Astrophysical Journal*, 183:237–264, July 1973.

[6] M. Bernardi, R. K. Sheth, J. Annis, S. Burles, D. J. Eisenstein, D. P. Finkbeiner, D. W. Hogg, R. H. Lupton, D. J. Schlegel, M. SubbaRao, N. A. Bahcall, J. P. Blakeslee, J. Brinkmann, F. J. Castander, A. J. Connolly, I. Csabai, M. Doi, M. Fukugita, J. Frieman, T. Heckman, G. S.

Hennessy, Ž. Ivezić, G. R. Knapp, D. Q. Lamb, T. McKay, J. A. Munn, R. Nichol, S. Okamura, D. P. Schneider, A. R. Thakar, and D. G. York. Early-Type Galaxies in the Sloan Digital Sky Survey. I. The Sample. *Astronomical Journal*, 125:1817–1848, April 2003.

[7] M. Bernardi, R. K. Sheth, J. Annis, S. Burles, D. J. Eisenstein, D. P. Finkbeiner, D. W. Hogg, R. H. Lupton, D. J. Schlegel, M. SubbaRao, N. A. Bahcall, J. P. Blakeslee, J. Brinkmann, F. J. Castander, A. J. Connolly, I. Csabai, M. Doi, M. Fukugita, J. Frieman, T. Heckman, G. S. Hennessy, Ž. Ivezić, G. R. Knapp, D. Q. Lamb, T. McKay, J. A. Munn, R. Nichol, S. Okamura, D. P. Schneider, A. R. Thakar, and D. G. York. Early-type Galaxies in the Sloan Digital Sky Survey. II. Correlations between Observables. *Astronomical Journal*, 125:1849–1865, April 2003.

[8] W. Bian and Y. Zhao. The Black Hole-Bulge Relation in Active Galactic Nuclei. *Monthly Notices of the Royal Astronomical Society*, 347:607–612, January 2004.

[9] E. Bonning, P. Marronetti, D. Neilsen, and R. Matzner. Physics and Initial Data for Multiple Black Hole Spacetimes. *Physical Review D*, 68(4):044019–+, August 2003.

[10] T. A. Boroson. Does the Narrow [O III] λ5007 Line Reflect the Stellar Velocity Dispersion in Active Galactic Nuclei? *Astrophysical Journal*, 585:647–652, March 2003.

[11] T. A. Boroson and R. F. Green. The Emission-Line Properties of Low-Redshift Quasi-Stellar Objects. *Astrophysical Journal Supplement*, 80:109–135, May 1992.

[12] J. M. Bowen and J. W. York. Time-Asymmetric Initial Data for Black Holes and Black-Hole Collisions. *Physical Review D*, 21:2047–2056, April 1980.

[13] D. R. Brill and R. W. Lindquist. Interaction Energy in Geometrostatics. *Physical Review*, 131:471–476, July 1963.

[14] A. Burkert and J. Silk. Star Formation-Regulated Growth of Black Holes in Protogalactic Spheroids. *Astrophysical Journal Letters*, 554:L151–L154, June 2001.

[15] A. Čadež. Apparent Horizons in the Two-Black-Hole Problem. *Annals of Physics*, 83:449, 1974.

[16] B. Carter. Global Structure of the Kerr Family of Gravitational Fields. *Physical Review*, 174:1559–1571, 1968.

[17] S. A. Caveny. *Tracking black holes in numerical relativity: Foundations and applications*. PhD thesis, University of Texas at Austin, 2002.

[18] K. Chen, J. P. Halpern, and A. V. Filippenko. Kinematic Evidence for a Relativistic Keplerian Disk - ARP 102B. *Astrophysical Journal*, 339:742–751, April 1989.

[19] C. T. Cunningham and J. M. Bardeen. The Optical Appearance of a Star Orbiting an Extreme Kerr Black Hole. *Astrophysical Journal Letters*, 173:L137+, May 1972.

[20] D. J. E. Floyd, M. J. Kukula, J. S. Dunlop, R. J. McLure, L. Miller, W. J. Percival, S. A. Baum, C. P. O'Dea et al. The Host Galaxies of Luminous Quasars, 2003. (preprint) astro-ph/0308436.

[21] S. Dain. Black Hole Interaction Energy. *Physical Review D*, 66(8):084019–+, October 2002.

[22] J. S. Dunlop, R. J. McLure, M. J. Kukula, S. A. Baum, C. P. O'Dea, and D. H. Hughes. Quasars, their Host Galaxies and their Central Black Holes. *Monthly Notices of the Royal Astronomical Society*, 340:1095–1135, April 2003.

[23] L. Ferrarese and D. Merritt. A Fundamental Relation between Supermassive Black Holes and Their Host Galaxies. *Astrophysical Journal Letters*, 539:L9–L12, August 2000.

[24] D. A. Forbes and T. J. Ponman. On the Relationship between Age and Dynamics in Elliptical Galaxies. *Monthly Notices of the Royal Astronomical Society*, 309:623–628, November 1999.

[25] M. Fukugita, K. Shimasaku, and T. Ichikawa. Galaxy Colors in Various Photometric Band Systems. *Publications of the Astronomical Society of the Pacific*, 107:945–+, October 1995.

[26] A. Garat and R. H. Price. Nonexistence of Conformally Flat Slices of the Kerr Spacetime. *Physical Review D*, 61:124011, 2000.

[27] K. Gebhardt, R. Bender, G. Bower, A. Dressler, S. M. Faber, A. V. Filippenko, R. Green, C. Grillmair, L. C. Ho, J. Kormendy, T. R. Lauer, J. Magorrian, J. Pinkney, D. Richstone, and S. Tremaine. A Relationship between Nuclear Black Hole Mass and Galaxy Velocity Dispersion. *Astrophysical Journal Letters*, 539:L13–L16, August 2000.

[28] K. Gebhardt, J. Kormendy, L. C. Ho, R. Bender, G. Bower, A. Dressler, S. M. Faber, A. V. Filippenko, R. Green, C. Grillmair, T. R. Lauer, J. Magorrian, J. Pinkney, D. Richstone, and S. Tremaine. Black Hole Mass Estimates from Reverberation Mapping and from Spatially Resolved Kinematics. *Astrophysical Journal Letters*, 543:L5–L8, November 2000.

[29] E. Gourgoulhon, P. Grandclément, and S. Bonazzola. Binary black holes in Circular Orbits. I. A Global Spacetime Approach. *Physical Review D*, 65(4):044020–+, February 2002.

[30] E. Gourgoulhon, P. Grandclément, and S. Bonazzola. Last Orbits of Binary Black Holes. *Int. J. Mod. Phys.*, A17:2689–2694, 2002.

[31] M. G. Haehnelt and G. Kauffmann. The Correlation Between Black Hole Mass and Bulge Velocity Dispersion in Hierarchical Galaxy Formation Models. *Monthly Notices of the Royal Astronomical Society*, 318:L35–L38, November 2000.

[32] M. G. Haehnelt and G. Kauffmann. Multiple Supermassive Black Holes in Galactic Bulges. *Monthly Notices of the Royal Astronomical Society*, 336:L61–L64, November 2002.

[33] T. S. Hamilton, S. Casertano, and D. A. Turnshek. The Luminosity Function of QSO Host Galaxies. *Astrophysical Journal*, 576:61–74, September 2002.

[34] N. Jansen, P. Diener, A. Khokhlov, and I. Novikov. Local and Global Properties of Conformally Flat Initial Data for Black Hole Collisions. *Class. Quant. Grav.*, 20:51–74, 2003.

[35] R. Kerr and A. Schild. A New Class of Solutions of the Einstein Field Equations. In G. Barbera, editor, *Atti del Congresso Sulla Relitivita Generale: Problemi Dell'Energia E Onde Gravitazionala*, 1965.

[36] R. Kerr and A. Schild. Some Algebraically Degenerate Solutions of Einstein's Gravitational Field Equations. In *Applications of Nonlinear Partial Differential Equations in Mathematical Physics*. Symposia B Applied Mathematics, 1965.

[37] L. Cheng, S. Salviander, and G. Shields. The Accretion Disk Temperature - Continuum Color Relationship in Quasars, 2004. in preparation.

[38] A. Laor. On Quasar Masses and Quasar Host Galaxies. *Astrophysical Journal Letters*, 505:L83–L86, October 1998.

[39] J.-P. Luminet. Image of a Spherical Black Hole with Thin Accretion Disk. *Astronomy and Astrophysics*, 75:228–235, May 1979.

[40] J. Magorrian, S. Tremaine, D. Richstone, R. Bender, G. Bower, A. Dressler, S. M. Faber, K. Gebhardt, R. Green, C. Grillmair, J. Kormendy, and T. Lauer. The Demography of Massive Dark Objects in Galaxy Centers. *Astronomical Journal*, 115:2285–2305, June 1998.

[41] P. Marronetti, M. Huq, P. Laguna, L. Lehner, R. A. Matzner, and D. Shoemaker. Approximate Analytical Solutions to the Initial Data Problem of Black Hole Binary Systems. *Physical Review D*, 62(2):024017–+, July 2000.

[42] P. Marronetti and R. A. Matzner. Solving the initial value problem of two black holes. *Phys. Rev. Lett.*, 85:5500–5503, 2000.

[43] P. Marziani, J. W. Sulentic, R. Zamanov, M. Calvani, D. Dultzin-Hacyan, R. Bachev, and T. Zwitter. An Optical Spectroscopic Atlas of Low-Redshift Active Galactic Nuclei. *Astrophysical Journal Supplement*, 145:199–211, April 2003.

[44] W. G. Mathews. Do quasars rotate? *Astrophysical Journal*, 258:425–433, July 1982.

[45] R. A. Matzner, M. F. Huq, and D. Shoemaker. Initial Data and Coordinates for Multiple Black Hole Systems. *Physical Review D*, 59(2):024015–+, January 1999.

[46] R. J. McLure and J. S. Dunlop. The Black Hole Masses of Seyfert Galaxies and Quasars. *Monthly Notices of the Royal Astronomical Society*, 327:199–207, October 2001.

[47] R. J. McLure and J. S. Dunlop. On the Black Hole-Bulge Mass Relation in Active and Inactive Galaxies. *Monthly Notices of the Royal Astronomical Society*, 331:795–804, April 2002.

[48] R. J. McLure and J. S. Dunlop. The Cosmological Evolution of Quasar Black Hole Masses. *Monthly Notices of the Royal Astronomical Society*, pages 209–+, June 2004.

[49] R. J. McLure, J. S. Dunlop, and M. J. Kukula. Two-Dimensional Modelling of Optical Hubble Space Telescope and Infrared Tip-Tilt Images of Quasar Host Galaxies. *Monthly Notices of the Royal Astronomical Society*, 318:693–702, November 2000.

[50] McLure, Percival and Dunlop, 2004. (in preparation).

[51] C. W. Misner, K. S. Thorne, and J. A. Wheeler. *Gravitation*. W. H. Freeman, New York, 1970.

[52] T. Mora and C. M. Will. Numerically Generated Quasiequilibrium Orbits of Black Holes: Circular or Eccentric? *Physical Review D*, 66(10):101501–+, November 2002.

[53] N. Ó. Murchadha and J. W. York. Initial-value Problem of General Relativity I. General Formulation and Physical Interpretation. *Physical Review D*, 10:428, 1974.

[54] N. Ó. Murchadha and J. W. York. Initial-value Problem of General Relativity II. Stability of Solutions of the Initial-Value Equations. *Physical Review D*, 10:437, 1974.

[55] N. Ó. Murchadha and J. W. York. *Relativity and Gravitation*, 7:257, 1976.

[56] C. H. Nelson. Black Hole Mass, Velocity Dispersion, and the Radio Source in Active Galactic Nuclei. *Astrophysical Journal Letters*, 544:L91–L94, December 2000.

[57] C. H. Nelson and M. Whittle. Stellar and Gaseous Kinematics of Seyfert Galaxies. I. Spectroscopic Data. *Astrophysical Journal Supplement*, 99:67–+, July 1995.

[58] C. H. Nelson and M. Whittle. Stellar and Gaseous Kinematics of Seyfert Galaxies. II. The Role of the Bulge. *Astrophysical Journal*, 465:96–+, July 1996.

[59] J. Ostriker. Collisional Dark Matter and the Origin of Massive Black Holes. *Physical Review Letters*, 04:5258–5260, 2000.

[60] D. N. Page and K. S. Thorne. Disk-Accretion onto a Black Hole. Time-Averaged Structure of Accretion Disk. *Astrophysical Journal*, 191:499–506, July 1974.

[61] W. J. Percival, L. Miller, R. J. McLure, and J. S. Dunlop. The Host Galaxies of Luminous Radio-Quiet Quasars. *Monthly Notices of the Royal Astronomical Society*, 322:843–858, April 2001.

[62] H. P. Pfeiffer, G. B. Cook, and S. A. Teukolsky. Comparing Initial-Data Sets for Binary Black Holes. *Physical Review D*, 66(2):024047–+, July 2002.

[63] H. P. Pfeiffer, L. E. Kidder, M. A. Scheel, and S. A. Teukolsky. A Multidomain Spectral Method for Solving Elliptic Equations. *Comput. Phys. Commun.*, 152:253–273, 2003.

[64] H. P. Pfeiffer, S. A. Teukolsky, and G. B. Cook. Quasicircular Orbits for Spinning Binary Black Holes. *Physical Review D*, 62(10):104018–+, November 2000.

[65] W. H. Press, S. A. Teukolsky, W. T. Vetterling, and B. P. Flannery. *Numerical recipes in FORTRAN. The art of scientific computing*. Cambridge: University Press, —c1992, 2nd ed., 1992.

[66] R. H. Price and J. T. Whelan. Tidal Interaction in Binary-Black-Hole Inspiral. *Physical Review Letters*, 87(23):231101–+, December 2001.

[67] D. J. Schade, B. J. Boyle, and M. Letawsky. Hubble Space Telescope Observations of X-Ray-Selected Active Galactic Nuclei. *Monthly Notices of the Royal Astronomical Society*, 315:498–516, July 2000.

[68] G. A. Shields. Thermal Continuum from Accretion Disks in Quasars. *Nature*, 272:706–708, April 1978.

[69] G. A. Shields, K. Gebhardt, S. Salviander, B. J. Wills, B. Xie, M. S. Brotherton, J. Yuan, and M. Dietrich. The Black Hole-Bulge Relationship in Quasars. *Astrophysical Journal*, 583:124–133, January 2003.

[70] G. A. Shields, L. Wobus, and D. Husfeld. Accretion Disks and the Lyman Continuum Polarization of QSOs. *Astrophysical Journal*, 496:743–+, March 1998.

[71] J. Silk and M. J. Rees. Quasars and Galaxy Formation. *Astronomy and Astrophysics*, 331:L1–L4, March 1998.

[72] W. Sun and M. A. Malkan. Fitting Improved Accretion Disk Models to Multi-Wavelength Continuum of Active Galactic Nuclei. In *Supermassive Black Holes*, pages 273–278, 1988.

[73] R. A. Sunyaev and L. G. Titarchuk. Comptonization of Low-Frequency Radiation in Accretion Disks. *Astronomy and Astrophysics*, 143:374–388, February 1985.

[74] Y. Tanaka, K. Nandra, A. C. Fabian, H. Inoue, C. Otani, T. Dotani, K. Hayashida, K. Iwasawa, T. Kii, H. Kunieda, F. Makino, and M. Mat-

suoka. Gravitationally Redshifted Emission Implying an Accretion Disk and Massive Black-Hole in the Active Galaxy MCG:-6-30-15. *Nature*, 375:659–+, June 1995.

[75] S. A. Teukolsky. *Perturbations Of A Rotating Black Hole*. PhD thesis, California Institute of Technology, 1973.

[76] K. S. Thorne, R. H. Price, and D .A. Macdonald. *Black Holes, the Membrane Paradigm*. Yale University Press, New Haven, 1986.

[77] Cactus Computational Toolkit. http://www.cactuscode.org.

[78] S. Tremaine, K. Gebhardt, R. Bender, G. Bower, A. Dressler, S. M. Faber, A. V. Filippenko, R. Green, C. Grillmair, L. C. Ho, J. Kormendy, T. R. Lauer, J. Magorrian, J. Pinkney, and D. Richstone. The Slope of the Black Hole Mass versus Velocity Dispersion Correlation. *Astrophysical Journal*, 574:740–753, August 2002.

[79] R. Wald. Gravitational Spin Interaction. *Phys. Rev.*, D6:406–413, 1972.

[80] R. Wald. *General Relativity*. University of Chicago Press, Chicago, 1984.

[81] A. S. Wilson and T. M. Heckman. The Narrow Line Region and Associated Radio Emission in Active Galactic Nuclei. In *Astrophysics of Active Galaxies and Quasi-Stellar Objects*, pages 39–109, 1985.

[82] J. R. Wilson and G. J. Mathews. Instabilities in Close Neutron Star Binaries. *Physical Review Letters*, 75:4161–4164, December 1995.

[83] J. York and T. Piran. The Initial Value Problem and Beyond. In R. Matzner and L. Shepley, editors, *Spacetime and Geometry: The Alfred Schild Lectures*. University of Texas Press, Austin, Texas, 1982.

[84] J. W. York. Conformal "Thin-Sandwich" Data for the Initial-Value Problem of General Relativity. *Physical Review Letters*, 82:1350–1353, February 1999.

Vita

Erin Wells Bonning was born on February 26, 1975 in Annapolis, Maryland, the daughter of Stuart Wells Bonning and Maryann Longhenry Bonning. She received the Bachelor of Arts degree in Liberal Arts from St. John's College in Annapolis, Maryland in May 1997. After working briefly at the Naval Research Lab in Washington, DC, she entered the Graduate School of the University of Texas at Austin in August of 1998.

Permanent address: 4501 Speedway
Austin, Texas 78751

This dissertation was typeset with LaTeX[†] by the author.

[†]LaTeX is a document preparation system developed by Leslie Lamport as a special version of Donald Knuth's TeX Program.